Design of a Host-guest Hybrid Catalytic System Through Aperture-opening Encapsulation Using Metal-organic Framework:

Author: Zhehui Li

Design of a Host-guest Hybrid Catalytic System Through Aperture-opening Encapsulation Using Metal-organic Framework

Zhehui Li

A dissertation

submitted to the Faculty of

the Department of Chemistry

in partial fulfillment

of the requirements for the degree of

Doctor of Philosophy

Boston College
Morrissey College of Arts and Sciences
Graduate School

2019

Design of a Host-guest Catalytic System Through Aperture-opening Encapsulation Using Metal-organic Framework

Zhehui Li

Advisor: Prof. Chia-Kuang (Frank) Tsung, Ph.D.

Prof. Jeffery A. Byers, Ph.D.

Abstract. Homogeneous catalysts are advantageous in selective catalysis due to the well-defined active site at the molecular level. The poor recyclability, bimolecular aggregation, and undesired poison resistance of homogeneous catalysts hinder further industrial application despite the controlled reaction pathway due to the homogeneous environment. On the other hand, heterogeneous catalysts are preferred in industry due to their high recyclability and high activity. Yet, poor selectivity due to undefined active sites is a drawback. The construction of a host-guest system where a molecular level catalyst is incorporated into the Metal-Organic Framework (MOF) provides a promising solution to bridge those two fields. This composite maintains the advantages of homogeneous and heterogeneous catalysts and overcomes the disadvantages. However, finding an incorporation method that is versatile with minimum synthetic modification of the host and guest remains one of the challenges.

In the first part of this dissertation, a new concept called "aperture-opening encapsulation'' is introduced for incorporating large and diverse guest molecules into MOFs without changing the identity of either the guest or MOF. The approach capitalizes on the existence of linker exchange reactions, which, as our kinetic studies show, proceed via competition between associative and dissociative exchange mechanisms. The second part describes how this method is applied to incorporate a molecular catalyst into the cavity of UiO-66 for the hydrogenation of carbon dioxide to formate, which is a useful application

for energy related industry. The developed hybrid composite showed the ability to be recycled, showed no evidence of bimolecular catalyst decomposition, and was less prone to catalyst poisoning. These results demonstrate for the first time how the aperture-opening process resulting from linker dissociation in MOFs can be utilized as a strategy to synthesize host-guest materials useful for chemical catalysis. After the establishment of the hybrid catalyst, the last part of the dissertation describes our efforts into the investigation of mass transport in catalysis. The understanding of the interaction between the host-guest is beneficial for the development of biological analogs in the future.

ACKNOWLEDGEMENT

You never know what you can do until you try it. Being in graduate school is never an easy road for me, and I feel so grateful that so many people came across this chapter of my life and gave me life-lasting memories and unconditonal support.

I want to thank first and foremost my family, in particular my parents. You give me the best you have, and teach me how to be a strong person with a good heart.

Special thanks to, of course, Jeff and Frank, not only for your guidance in my prfessional career to be a better scientist, but also makes me grow internally as a person and bring the best out of me.

Thanks to the wonderful scientist came before. Thank Randy and Joe for your guidance in the early stage of my gradute school, and hope you all the best in the future. Thank Prof. Ken Mertz for very nice conversations. I've learnt so muc from you.

My dear friends, thank you for bringing so much fun into my life. 321 room gang, Enming, Qingmei, Haoran, Mahboobeh, Munira, NEYCC-GEX gang. You are the most werid people I have ever met, and hey, I am weird too. ☺

Thanks to my two group members. I have to say, you guys turned me into an alcholic.. Thanks to our amazing MOF subgroup. This is the most dynamtic, stimulating subgroup I have ever seen and I am so lucky to be part of it. Carry the torch!

Thanks finally to my committee members, Prof. Dunwei Wang and Prof. Shih-Yuan Liu for valuale suggestions.

TABLE OF CONTENT

Chapter 1. MOFs as porous host

1.1 Crystalline porous materials in catalysis

Synthetic crystalline porous materials are applied in a variety of fields, including gas separation/adsorption,[1] biological sensing,[2] catalysis,[3] and food production.[4] Among those applications, catalysis is of particularly significant industrial importance. Since the early 1980s, zeolites or aluminosilicates have remained the most popular porous materials for catalysis in academic settings and industrial applications, finding use as solid catalysts, molecular sieves, and host matrices.[5] The strong Si-O and Al-O bonds render these materials stable under a wide variety of conditions, thereby making them attractive for catalysis. Furthermore, the porous structure of zeolites allows them to accommodate a wide variety of cations, such as Na^+, K^+, Ca^{2+}, and Mg^{2+}.[6] These positive ions are loosely bound and can readily be exchanged for others in solution, making zeolites a great platform for ion exchange.[7] Tremendous advances have been made in designing well-defined pores. Organic templates, which are removed by post-synthetic calcination, can be used to synthesize zeolites with a defined pore size. Zeolites with chiral pores have recently been realized for enantioselective catalysis, with ITQ-37 representing the first chiral zeolite composed of an enantiomorphous framework with a single gyroidal channel (Figure 1-1a)[8]. Thanks to the fast extension of pore structures in zeolites, transition metal complexes can be incorporated into zeolites to alleviate their bimolecular decomposition, such as anchoring rhodium dicarbonyl to highly dealuminated zeolite Y for alkene polymerization (Figure 1-1b).[9] Nevertheless, the synthetic difficulties associated with these processes has prevented widespread adoption of these methods. In addition, identification of active sites and mechanistic understanding of the catalytic transformation remains challenging.[3]

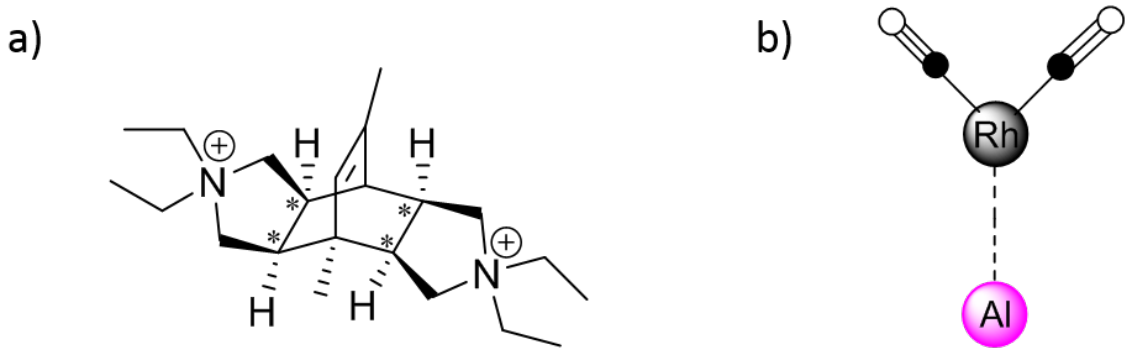

Figure 1-1. a) Structure of SDA2 used for synthesizing the ITQ–37 zeolite. SDA2 contains four chiral centres (marked with asterisks) in a meso conformation, making the overall molecule achiral. b) Simplified structural models for $Rh^{+}(CO)_2$ supported in dealuminated Y zeolite developed from EXAFS analysis

In the 1990s, well-defined supermolecular cages like cyclodextrin gained popularity in catalysis.[10] Cyclodextrin is an attractive mimic for artificial enzyme due to its ability to modulate the size-selectivity of a given reaction. It does so by confining the substrate within the ring, much like an enzyme does in nature. In early studies, Breslow found that electrophilic halogenation of methoxy-benzene regioselectively forms a para-substituted product when the substrate was confined within the ring. In a sharp contrast, both ortho- and para- substituted products were formed in the absence of the cyclodextrin (Figure 1-2), likely due to the blocking of ortho- position by the cavity.[11]

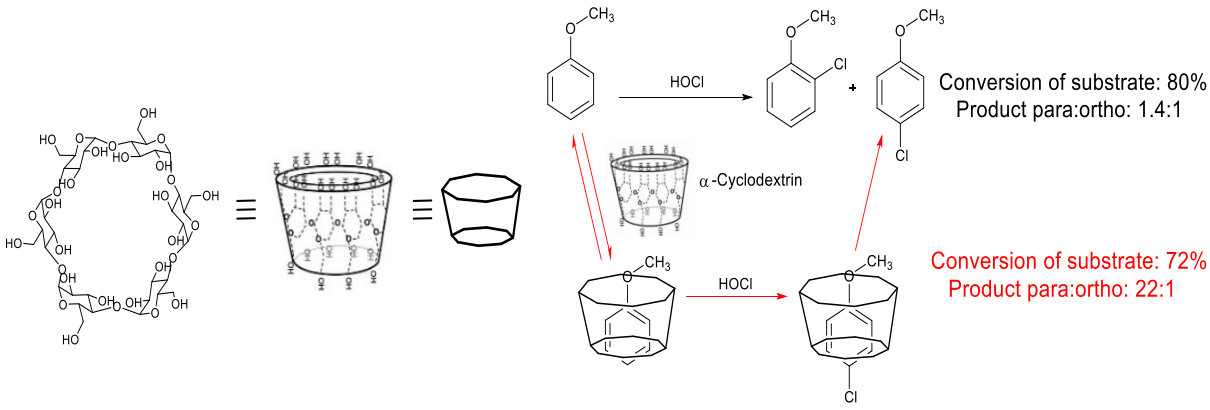

Figure 1-2. Halogenation of methoxy-benzene with and without an α-cyclodextrin ring.

In the late 1990s and early 2000s, Bergman and Raymond synthesized an M_4L_6 tetrahedral cage (Figure 1-3a). This invention was later used by Toste to bridge the fields of molecular biology and supramolecular chemistry.[12] The typical inorganic tetrahedral cage is constructed by the self-assembly of metal nodes and organic bridging linkers (Figure 1-3a). This M_4L_6 cage is able to distinguish between molecular recognition pathways, namely conformational selection[13] and induced fit[14]. Conformational selection describes the phenomenon that a dynamically fluctuating protein binds to another protein and shifts the conformational ensemble towards a stabilized state. On the other hand, induced fit refers to subtle changes in the active site occur when an enzyme binds to the appropriate substrate. Those two mechanisms are both challenging to be deconvoluted in biological system (Figure 1-2b).[12d] The invention of M_4L_6 is the first example of conformational selection in a synthetic system, and this simple enzyme mimic inform the design of efficient self-assembled microenvironment catalysts. Despite this enormous success in biomimicking, the tetrahedral cages commonly suffer from difficulties in structural diversification due to the lengthy synthetic sequence required to obtain the ligands needed for supramolecular construct.

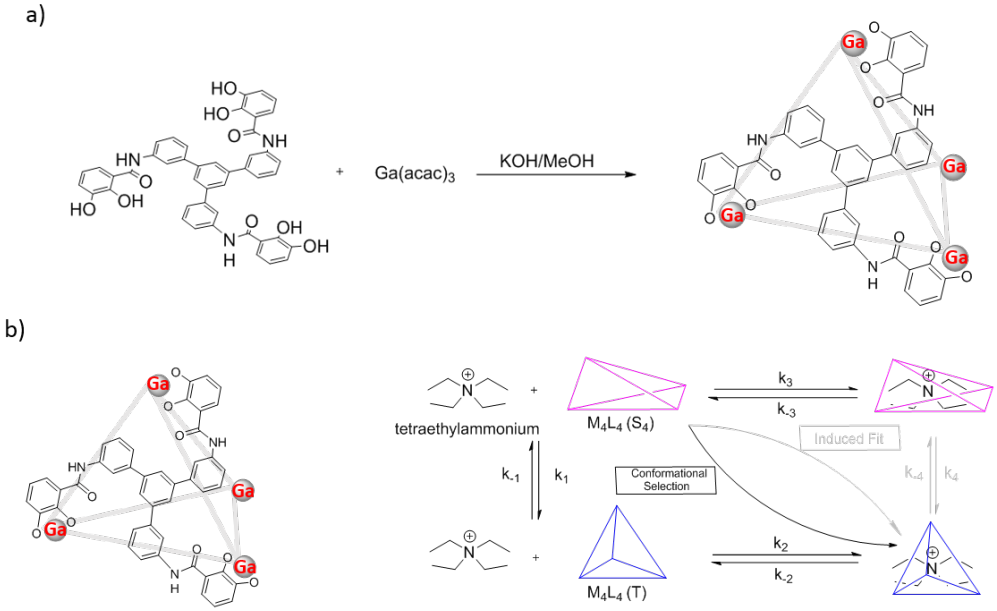

Figure 1-3. a) Self-assembly of an M_4L_6 cage. b) Distinguishing between a conformation selection and an induced fit mechanism in host-guest systems.

Supramolecular chemistry is a highly interdisciplinary field, the roots of which extend into organic chemistry, coordination chemistry, physical chemistry, and biochemistry.[15] Molecular recognition events represent the basis of information processing at the supramolecular level. The simplest recognition is the attractions between positively and negatively charged metal ions, and a supramolecular system has been demonstrated to enhance their attractions. For example, specific groups have been attached to functionalized bipyridines to form metal complexes with fixed geometries and physico-chemical properties (Figure 1-4a).[16] The fixation of the positively charged ions on to the supramolecular system allows the positively charged nucleate complexes to interact selectively with the negatively charged oligonucleotides (Figure 1-4b).[17]

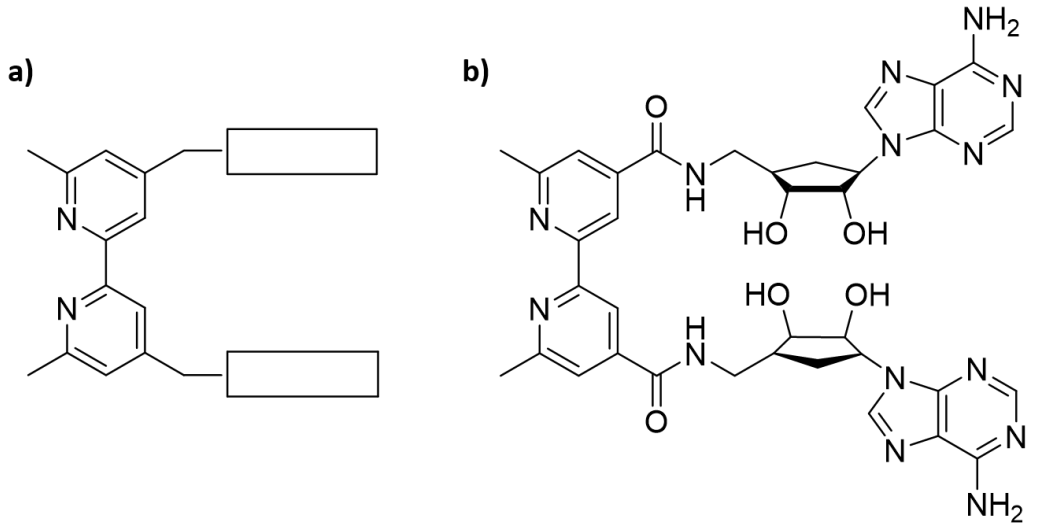

Figure 1-4. a) functionalized a,a'-bipyridines and b) bis-adenosine derivative.

The photogeneration of charge-separated states is important for the transfer of photosignals (e.g. through a membrane[18]) and inducing photocatalytic reactions (e.g. for artificial photosynthesis[19]). Silver ions are bound to the macrocycles of the electron receptors containing porphyrin sites (Figure 1-5).[20] As a result, the quenching of the singlet excited state of the Zn-porphyrin center is more efficient by an efficient intracomplex electron transfer, which generates a porphyrinium cation of long half-life. The continuous development of supramolecular chemistry provides a comprehensive solutions to scientific problems that are difficult to solve by focusing on a single field.

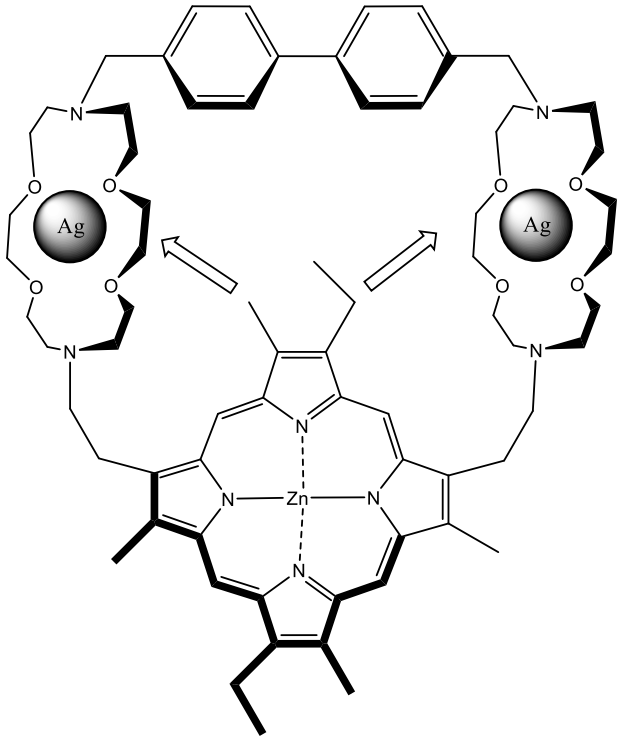

Figure 1-5. The donor (Zn sites) and acceptor (Ag sites) units in metal coordination centers.

Building on these supramolecular cages, a novel porous material was discovered that quickly gained popularity in cross-disciplinary scientific fields in the early 2000s.[21] This class of porous material is widely known as metal-organic frameworks (MOF), named by Yaghi[22], though they are also referred to as coordination polymers.[23] In this dissertation, we choose to refer to them as MOFs for consistency.

MOFs, as mentioned above, are a class of porous materials formed by the self-assembly of organic bridging linkers and metal nodes (Figure 1-6). Compared to other inorganic and organic matrices, broad choices of organic ligands and node topology endow MOFs a wide range of structural properties and functionalities.[24] Over the past two decades,

MOFs have shown great potential as a host material in the fields of catalysis,[25] such as gas separation,[26] drug delivery,[2] and sensing[27]. These applications largely take advantages of MOFs' high porosity and crystallinity, moderate chemical and thermal stability, as well as capacity for post-synthetic modification.[2, 25-27]

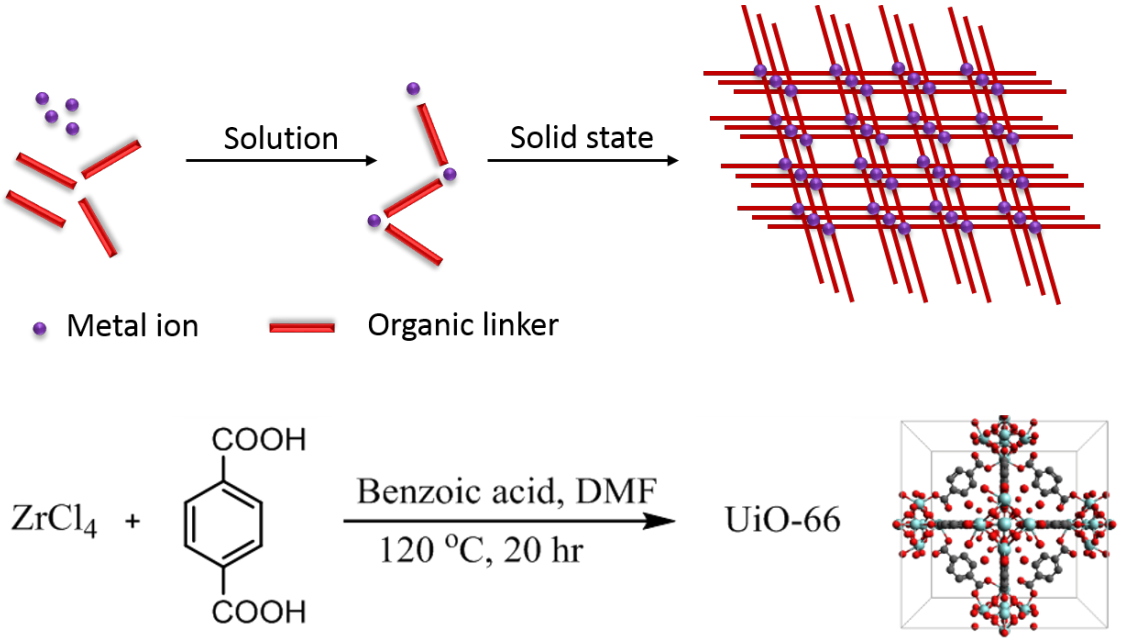

Figure 1-6. Self-assembly process of MOFs.

1.2 Metal-organic frameworks: opportunities for catalysis

Now that several of the unique properties of MOFs have been outlined in the previous section, this section will focus on how each component of the framework contributes to catalysis. It is generally accepted that MOF materials can be categorized into two different families based on the dimensionality of the inorganic framework (Figure 1-7):[28] In the first family, the organic-inorganic framework is organized into either 1- or 2-dimensional (1D or 2D) layers. 1D MOFs are often labeled metal-organic polyhedra (MOPs), and it should be noted that their inorganic moieties are often only partially

connected by bridging organic ligands or solvent molecules. In the second, 3D open-framework coordination polymers are made from 1D secondary building units (SBUs) (i.e. isolated metal ions) connected by bridging organic polytopic ligands. For example, MIL-53 (node: Al, ligand: 1,4-benzenedicarboxylate) belongs to the first family and MOF-5 (nodes: Zn_4O, ligand: 1,4-benzodicarboxylate) is in the second category.

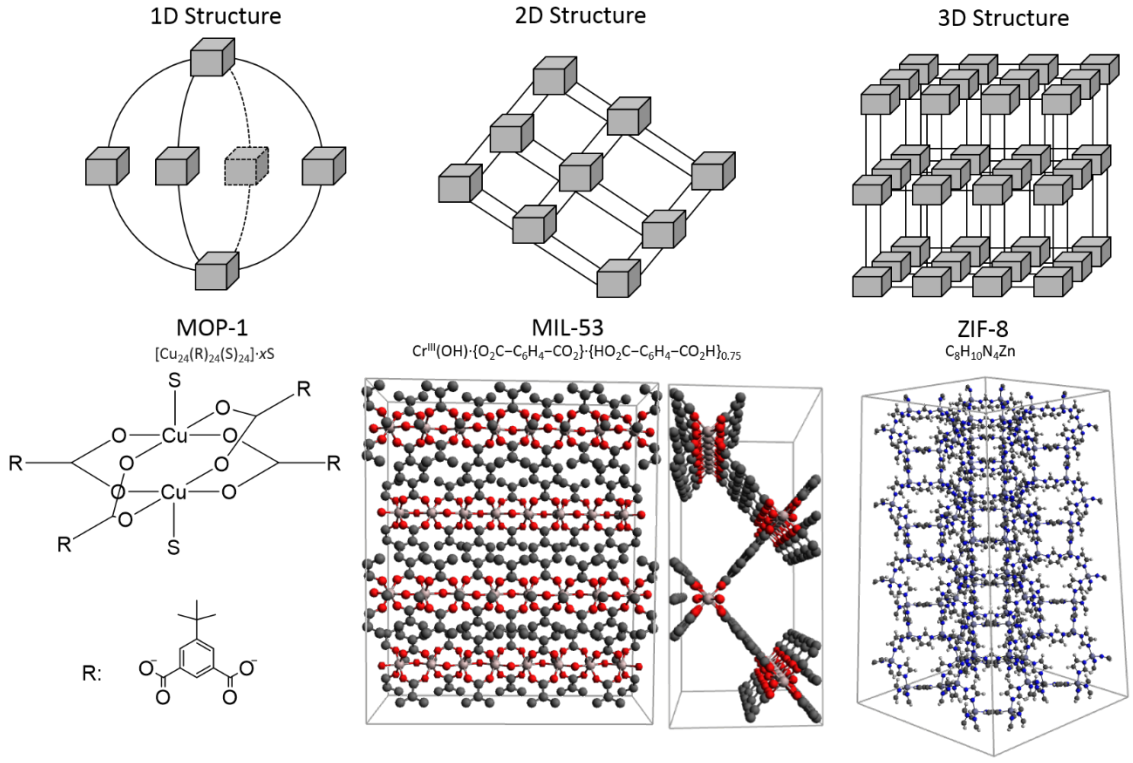

Figure 1-7. Representations of 1D, 2D, and 3D MOF stuctures.

Besides the coordination geometry, the organic and inorganic components of a MOF are also important for catalysis (Figure 1-8). It is possible, for instance, for the metal ions contained in a MOF's SBUs to serve as active sites for catalysis. For example, transition metal ions like Fe^{3+}, Cu^{2+} ,and Cr^{3+} are common catalytically active coordination metal nodes. Some catalytically active MOFs are $[Cu(im)_2]$ (im=imidazolate),[29] [Cu(2-

pymo)$_2$],[30] and HKUST-1(M) (M=Cr^{3+}, Fe^{3+}, Al^{3+}).[31] The metal ions in these structures have a high coordination number. Catalysis, conversely, usually requires coordination of the substrate to an unsaturated coordination site on the metal center. For catalytically active MOFs, the open coordination site is usually created by the dissociation of an organic bridging linker, though this can sometimes cause pores to collapse and lead to poor recyclability.[28b] Catalysis carried out throughout the entire MOF (i.e. on the surface) precludes the ability for the MOF to display size-selective catalytic performance, which provides little advantages compared to traditional heterogeneous catalysts or homogeneous catalysts supported on traditional supports (e.g. silica, alumina, etc.).

Besides metal nodes, the versatile organic linkers in a MOF can also serve as catalytic sites.[28b] MOFs that use linkers as active sites usually are composed of bifunctional organic linkers,[24] containing coordinative functional groups, like carboxylate, that coordinate to SBUs and maintain the crystallinity of MOF, and reactive functional groups, like lewis acids, which remain intact during the MOF synthesis and contribute to the catalytic activity of MOF. Some examples of catalytically active MOFs are IRMOF-3, NH_2-UiO-66, and NH_2-MIL-101(M) (M=Cr^{3+}, Fe^{3+}, Al^{3+}).[32] Adding amino functional groups is a common way to imbue a MOF with Lewis base character.

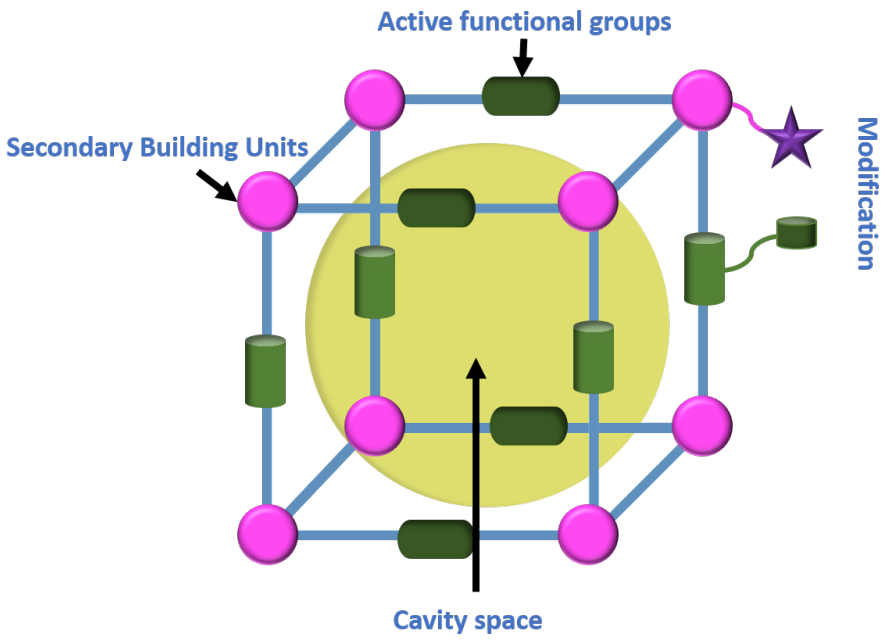

Figure 1-8. Simplified MOF picture where catalytically active moieties can be inserted through SBU/ligand modification and guest incorporation in the cavity.

All the MOFs mentioned above that utilize nodes and organic functional groups for catalysis are referred to as *as-synthesized active MOFs*.[24] On the other hand, for catalytically inert MOF materials, active sites can be grafted onto the originally inert MOF or the original, inert nodes can be post-synthetically replaced with active ones. For example, Lin incorporated Ir complexes into a UiO-66 analogue MOF using 2,2′-bipyridine-5,5′-dicarboxylate ligands to provide isolated anchoring sites for Ir. After activation, the MOF-immobilized Ir complex is active (TON: 6149, TOF: 410 h^{-1}) towards hydrogenation of CO_2 to formate (Figure 1-9a), while an Ir nanoparticle shows no conversion.[33] Ion exchange of metal nodes thus allows the originally inert MOF to become catalytically active. In another example, Dinca partially substituted Zn^{II} with Mn^{II} in MOF-5(Zn). The resultant Mn^{II} node can access terminal high-valent metal-oxo (Mn^{III}, Mn^{IV}) species that subsequently engage in catalytic oxygen atom transfer of cyclopentene due to the relatively

weak ligand fields provided by the SBU (Figure 1-9b). [34] In addition, many other groups have used similar strategies for other catalytically active MOFs.[24,28b,31]

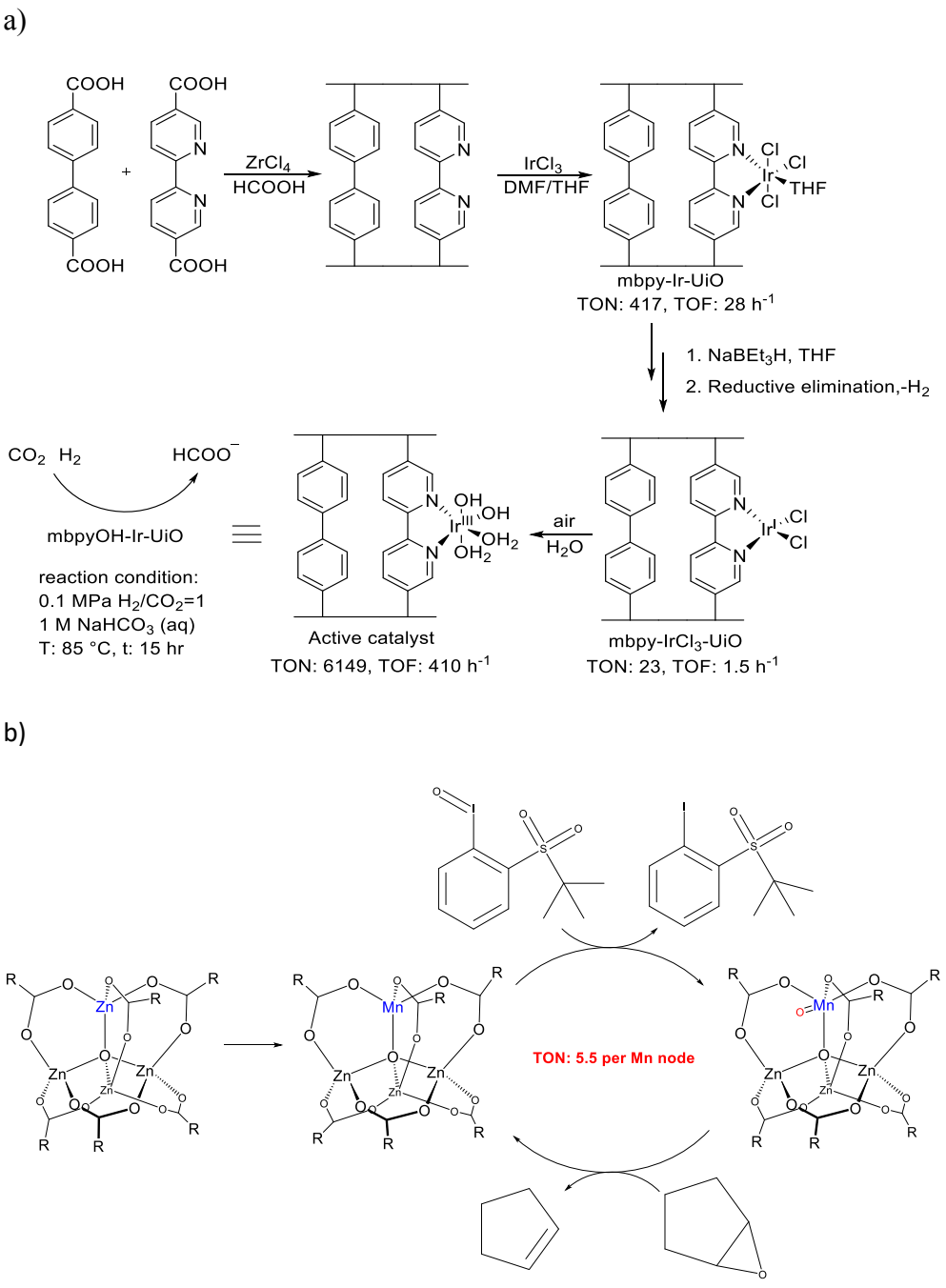

Figure 1-9. a) Ir complex incorporation into UiO-type MOFs for CO_2 hydrogenation. b) Partial substitution of Zn^{II} with Mn^{II} to activate MOF-5(Zn) for redox chemistry.

In summary, MOFs contain three well-differentiated parts that can support active sites for catalysis: the organic linker, the metal nodes, and the cavity space, two of which have been covered in this section. In the next section, the MOF cavity and the construction of a host-guest system will be discussed.

1.3 Using the MOF cavity space: host-guest systems

Recently, MOFs have come to bridge the gap between homogeneous and heterogeneous catalysis. In homogeneous catalysis, the well-defined molecular active site is advantageous for selective catalysis. The reaction can then usually be well controlled, both kinetically and thermodynamically, due to the homogenous environment. Organometallic complexes, for example, are a class of homogeneous catalysts that is widely used in industry for cross-coupling reactions,[35] olefin metathesis reactions,[36] polymerization catalysis,[37] and hydrogenation reactions.[38] Modifications to the organic ligand alters the primary coordination sphere, which can be used to regulate the activity and selectivity through electronic and steric effects. High catalytic performance is achieved through rational ligand design[35] or high throughput screening processes.[39] However, the poor recyclability, bimolecular aggregation, and low poison tolerance of homogeneous catalysts are common limitations, despite their high selectivity and desired activity.[40] Heterogeneous catalysts are instead preferred for many industrial applications, due to their high recyclability and high activity, yet these catalysts show poor selectivity due to their undefined active sites. MOF chemistry represents an opportunity to optimize molecular catalysts, merging the advantages of homogeneous and heterogeneous catalysts through the use of host-guest complexes.

In a host-guest system, active guest molecules are incorporated into the cavities of crystalline porous materials, imparting functionality for numerous applications in drug delivery,[41] sensing,[27, 42] catalysis,[33] and energy conversion (Figure 1-10).[40, 43] In the past two decades, MOFs have been more attractive for host-guest composites than zeolites. MOFs have high porosity and crystallinity, moderate chemical/thermal stability, and a capacity for post-synthetic modification.[2, 27] Compared to other pure inorganic and organic matrices, variety in organic ligands and node-strut topology endow MOFs with large structural libraries and functional tunability.[24]

Construction of MOF host-guest systems by simply diffusing guest molecules into the MOF cavity is generally limited to guests that are smaller than the window size of the MOF cage.[44] This limitation commonly leads to guest molecule leaching, since molecules that can diffuse in can also diffuse out, which is particularly problematic for catalytic applications.[45] Retaining guests in the cavity of MOFs by pursuing strategies that incorporate guests larger than the MOF aperture size could circumvent this problem.

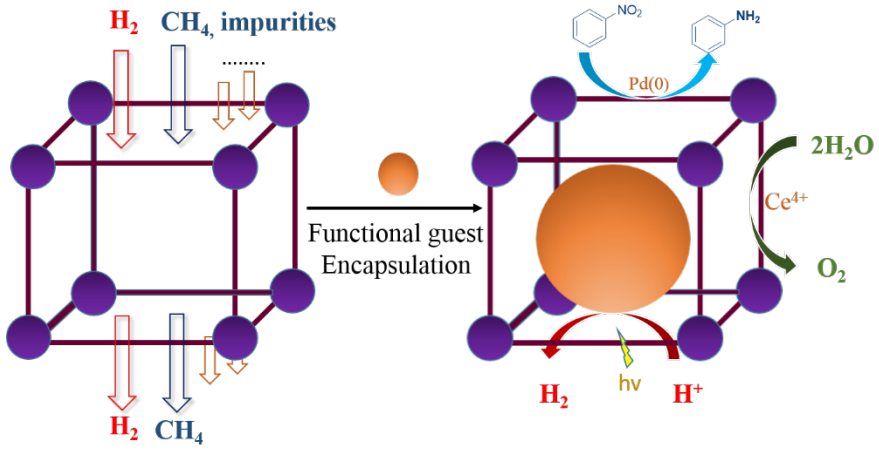

Figure 1-10. Applications of the host-guest system.

Two such strategies are the *de novo* encapsulation of the guest during MOF crystal growth and the ship-in-a-bottle assembly of the guest within the pore subunits.[28b] *De novo* encapsulation (which may be thought of as a "bottle-around-ship" method) involves mixing a functional guest molecule with MOF precursors during the process of MOF formation so that the MOF forms around the guest molecules (Figure 1-11a).[46] While convenient, this one-pot encapsulation method requires the guest molecule to be compatible with MOF synthesis conditions, which often involve high temperatures and the use of acid as a modulator. To date, this approach has only been applicable to a few organic compounds, like chromophore molecules,[47] metal ions,[48] and catalysts that have high thermal/chemical compatibility with MOF synthesis condition.

The ship-in-a-bottle approach is another elegant encapsulation strategy (Figure 1-11b).[48] This encapsulation strategy requires assembling the guest molecule within the cavity of the pre-synthesized MOF crystals. A number of techniques have been developed for this strategy, including using negatively charged MOFs to incorporate cationic organic compounds.[49] This approach is advantageous because it decouples the MOF synthesis from guest formation; however, the assembling of sophisticated catalytically active species within the MOF cavity still remains a challenge. MOFs also may not be compatible with the strong organic bases required for metal ligand metalation. So far, the most prevalent method in constructing host-guest composites relies on tethering the guest species to the backbone of the MOF linkers, similar to the aforementioned linker-based catalysis, but the loss in degrees of freedom for these tethered homogeneous catalysts can be detrimental to

their activity and selectivity. (Figure 1-11c)[33] Furthermore, there is little control over the distribution of catalyst throughout the MOF, which can impede size-exclusion catalysis.

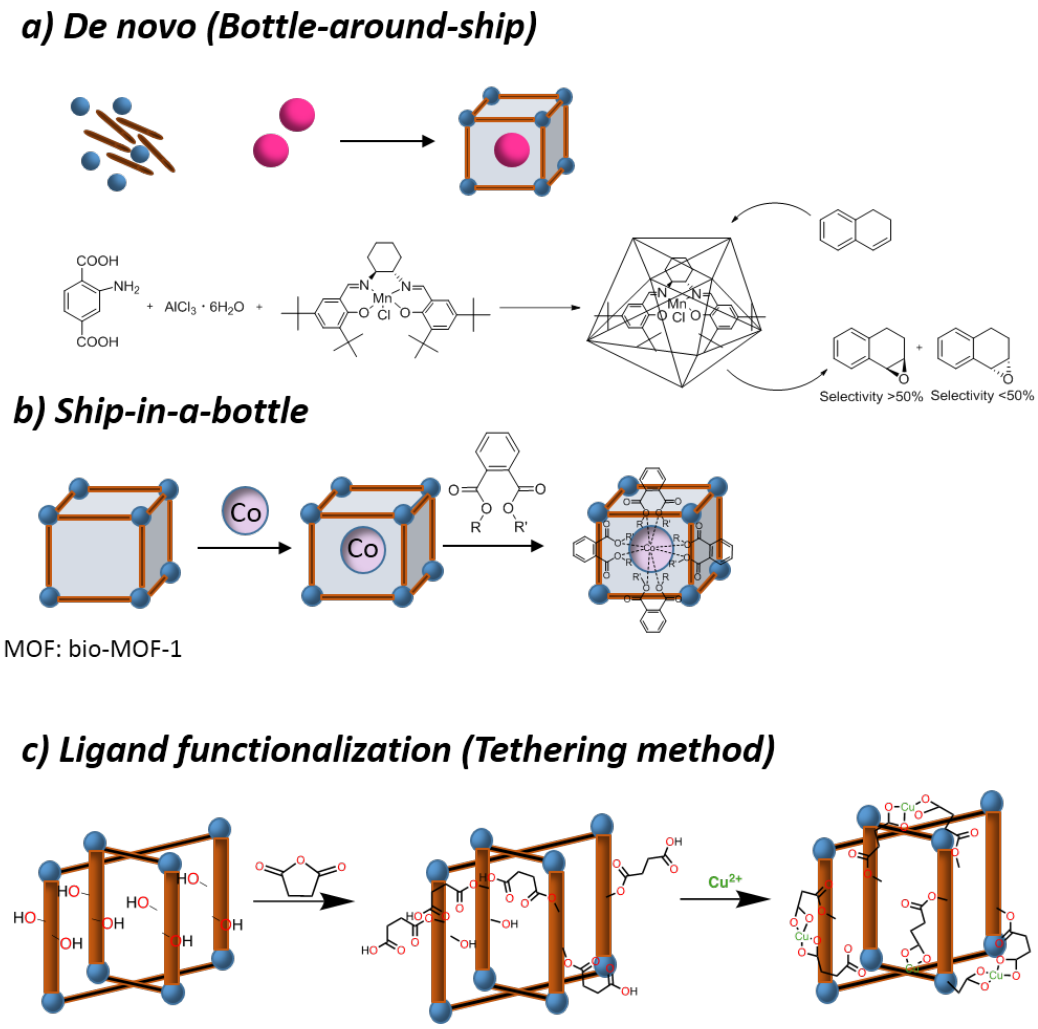

Figure 1-11. Strategies for encapsulating guests into MOFs.

1.4 Aperture-opening encapsulation for host-guest construction

Due to the labile binding between the organic bridging linker and the metal node, MOFs can undergo a linker exchange process in which the bridged linker in the MOF crystal can be exchanged with a structurally inert but chemically different functionalized ligand.[50] This phenomenon was first discovered by Choe[51] for pillared porphyrin paddlewheel framework and later modified by several groups.[52] This linker exchange

process is often referred to as solvent-assisted linker exchange (SALE) or post-synthetic modification (PSM). Our group prefers SALE, because the solvents used in this process often facilitate linker exchange. Through this process, additional functionalities can also be introduced to the organic linkers after synthesis of the MOF.[53]

SALE is a versatile and powerful method for synthesizing MOF materials that cannot be synthesized by direct methods.[53a] For instance, the direct synthesis of $Zn(im)_2$ (im=imidazolate) results in a non-porous *zni* structure, while the crystalline *sod* structure can be achieved through SALE between pre-synthesized $Zn(2\text{-mim})_2$ (ZiF-8) (mim=2-methyl imidazolate) and exogenous imidazolate.[53b] Ubiquitous in coordination chemistry, linker exchange between metal centers is described by one of two limiting pathways for ligand substitution: associative or dissociative.[39] Mechanistic studies were conducted to determine the underlying kinetics of SALE, and the results suggest the linker exchange proceeds associatively in the presence of excess exogenous imidazolate and dissociatively in its low concentration regime.[44] We believe the dissociative pathway 'opens' part of the framework and extends the aperture size of the pore, which allows for the encapsulation of guest molecules larger than the aperture size but smaller than the pore size (Figure 1-12a). We call this new host-guest system synthesis method aperture-opening encapsulation (Figure 1-12b).[44] Although the isolation and characterization of the short-lived aperture-opening intermediate are challenging, the successful formation of the host-guest system in ZiF-8 with a guest molecule of Rhodamine 6G or triphenylphosphine demonstrates that this method is successful and effective.

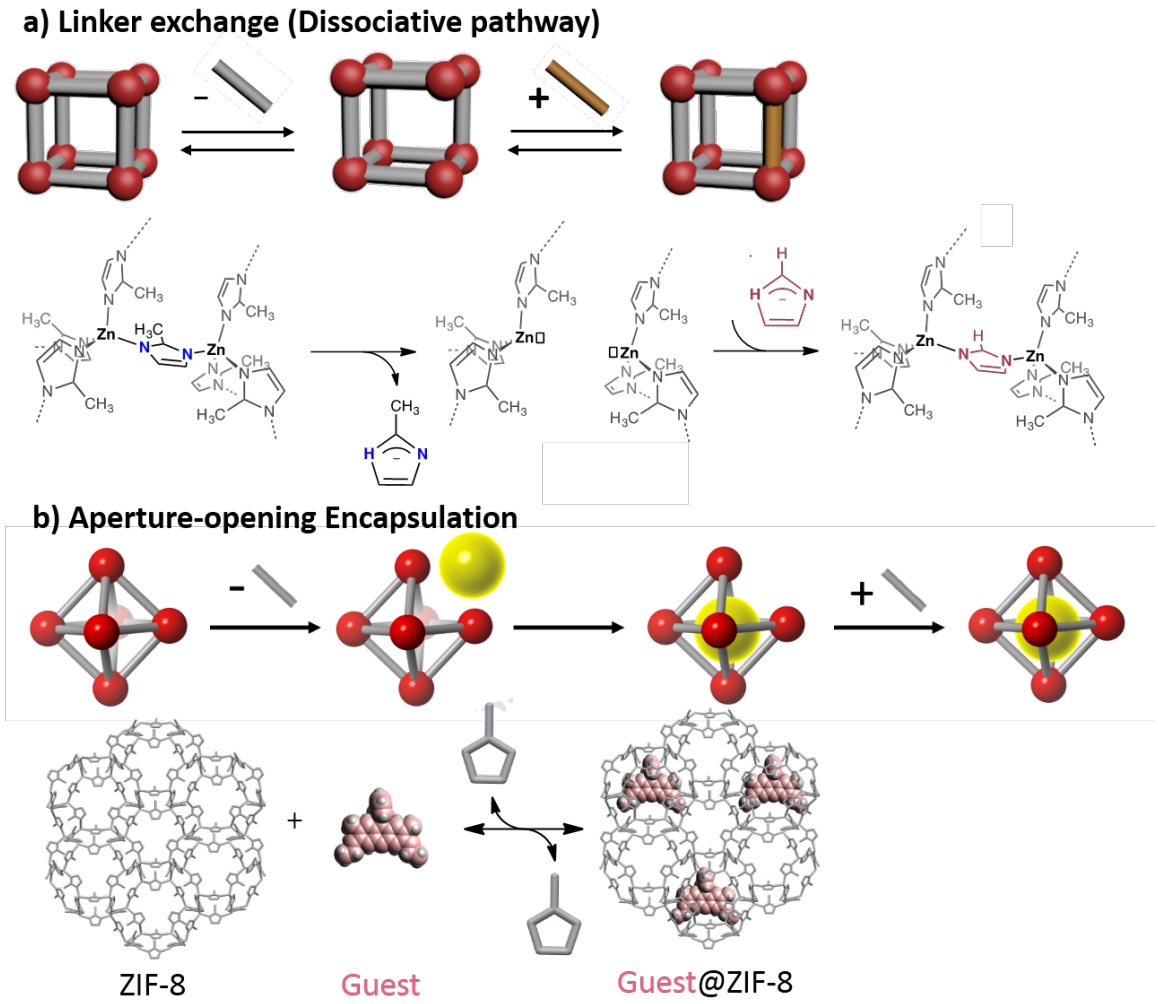

Figure 1-12. a) Linker exchange proceeds through the dissociative pathway. b) The aperture-opening encapsulation strategy.

1.5 The scope of this dissertation

Our interest in the construction of a host-guest system stems from the idea of designing better catalysts by bridging the gap between homogeneous and heterogeneous catalysis. We noticed that the design of the ligands found in most homogeneous catalysts requires lengthy synthesis sequences that highly limit their practical industrial application, despite their superior catalytic performance. On the other hand, despite the advances being made in heterogeneous catalyst design, the lack of a well-defined active site at the

molecular level has always been an issue. We believe the heterogenization of homogeneous catalysts provides an alternative approach to combine the advantages of both homogeneous and heterogeneous catalysis. MOFs have rapidly become one of the most popular host structures, and we started our project by searching for ways to incorporate guest molecules into MOFs. Most known methods are limited to the use of specific MOFs or guest molecules (e.g. ionic MOFs[54] and simple chromophore molecules[42]), with the remainder requiring non-trivial materials engineering or guest syntheses. The ideal method to construct a host-guest system should be widely applicable to a variety of systems and require little engineering of the host and the guest to facilitate guest encapsulation. We found that such a method could be designed by taking advantage of SALE. Initially, application and characterization were difficult because there is a lack of suitable spectroscopic signatures for following the mechanism of the exchange reactions. Through interdisciplinary inputs in materials and organic chemistry, we were able to develop an analytical tool box for the kinetic study of materials. These efforts, which will be discussed in Chapter Two, were pioneered by Dr. Joe Morabito and Dr. Lien-Yang Chou from the Tsung lab, under the guidance by both Prof. Tsung and Prof. Byers. After the initial establishment of the aperture-opening encapsulation mechanism, the use of this novel encapsulation method to construct a catalytically active host-guest system becomes the core of this research dissertation. Ongoing challenges and exciting directions in the development process, such as ensuring the integrity of the catalyst structure after encapsulation, preventing active site leaching during catalysis, minimizing mass transport using materials engineering, and mimicking enzymatic activity through outer-sphere interaction, will be discussed in later chapters.

Reference

1. Llewellyn, P. L.; Bourrelly, S.; Serre, C.; Vimont, A.; Daturi, M.; Hamon, L.; De Weireld, G.; Chang, J.-S.; Hong, D.-Y.; Kyu Hwang, Y.; Hwa Jhung, S.; Férey, G., "*High Uptakes of CO2 and CH4 in Mesoporous Metal—Organic Frameworks MIL-100 and MIL-101.*" Langmuir **2008**, 24 (14), 7245-7250.

2. Horcajada, P.; Gref, R.; Baati, T.; Allan, P. K.; Maurin, G.; Couvreur, P.; Férey, G.; Morris, R. E.; Serre, C., *"Metal–Organic Frameworks in Biomedicine."* Chem. Rev. **2012**, 112 (2), 1232-1268.

3. Čejka, J.; Wichterlová, B., *"Acid-catalyzed synthesis of mono- and dialkyl benzenes over zeolites: Active sites, zeolite topology, and reaction mechanisms."* Catalysis Reviews **2002**, 44 (3), 375-421.

4. Schüth, F.; Schmidt, W., *"Microporous and Mesoporous Materials."* Advanced Materials **2002**, 14 (9), 629-638.

5. (a) Avnir, D.; Levy, D.; Reisfeld, R., *"The nature of the silica cage as reflected by spectral changes and enhanced photostability of trapped Rhodamine 6G."* The Journal of Physical Chemistry **1984**, 88 (24), 5956-5959; (b) Reeve, P. J.; Fallowfield, H. J., *"Natural and surfactant modified zeolites: A review of their applications for water remediation with a focus on surfactant desorption and toxicity towards microorganisms."* Journal of Environmental Management **2018**, 205, 253-261.

6. Sheldon, R. A.; Arends, I. W. C. E.; Lempers, H. E. B., *"Liquid phase oxidation at metal ions and complexes in constrained environments."* Catalysis Today **1998**, 41 (4), 387-407.

7. Hedström, A., *"Ion Exchange of Ammonium in Zeolites: A Literature Review."* Journal of Environmental Engineering **2001**, 127 (8), 673-681.

8. Sun, J.; Bonneau, C.; Cantín, Á.; Corma, A.; Díaz-Cabañas, M. J.; Moliner, M.; Zhang, D.; Li, M.; Zou, X., *"The ITQ-37 mesoporous chiral zeolite."* Nature **2009**, 458, 1154-1157.

9. Goellner, J. F.; Gates, B. C.; Vayssilov, G. N.; Rösch, N., *"Structure and Bonding of a Site-Isolated Transition Metal Complex: Rhodium Dicarbonyl in Highly Dealuminated Zeolite Y."* Journal of the American Chemical Society **2000**, 122 (33), 8056-8066.

10. Breslow, R.; Dong, S. D., *"Biomimetic Reactions Catalyzed by Cyclodextrins and Their Derivatives."* Chemical Reviews **1998**, 98 (5), 1997-2012.

11. (a) Breslow, R.; Campbell, P., *"Selective aromatic substitution within a cyclodextrin mixed complex."* Journal of the American Chemical Society **1969**, 91 (11), 3085-3085; (b) Breslow, R.; Kohn, H.; Siegel, B., *"Methylated cyclodextrin and a cyclodextrin polymer as catalysts in selective anisole chlorination."* Tetrahedron Letters **1976**, 17 (20), 1645-1646.

12. (a) Yeh, R. M.; Xu, J.; Seeber, G.; Raymond, K. N., "*Large M4L4 (M = Al(III), Ga(III), In(III), Ti(IV)) Tetrahedral Coordination Cages: an Extension of Symmetry-Based Design."* Inorganic Chemistry **2005**, 44 (18), 6228-6239; (b) Fiedler, D.; Pagliero, D.; Brumaghim, J. L.; Bergman, R. G.; Raymond, K. N., *"Encapsulation of Cationic Ruthenium Complexes into a Chiral Self-Assembled Cage."* Inorganic Chemistry **2004**, 43 (3), 846-848; (c) Dalton, D. M.; Ellis, S. R.; Nichols, E. M.; Mathies, R. A.; Toste, F. D.; Bergman, R. G.; Raymond, K. N., *"Supramolecular Ga4L612– Cage Photosensitizes 1,3-*

Rearrangement of Encapsulated Guest via Photoinduced Electron Transfer." Journal of the American Chemical Society **2015**, 137 (32), 10128-10131; (d) Hong, C. M.; Kaphan, D. M.; Bergman, R. G.; Raymond, K. N.; Toste, F. D., *"Conformational Selection as the Mechanism of Guest Binding in a Flexible Supramolecular Host."* Journal of the American Chemical Society **2017**, 139 (23), 8013-8021.

13. Csermely, P.; Palotai, R.; Nussinov, R., *"Induced fit, conformational selection and independent dynamic segments: an extended view of binding events."* Trends in Biochemical Sciences **2010**, 35 (10), 539-546.
14. Wlodarski, T.; Zagrovic, B., *"Conformational selection and induced fit mechanism underlie specificity in noncovalent interactions with ubiquitin."* Proceedings of the National Academy of Sciences **2009**, 106 (46), 19346-19350.
15. Mattia, E.; Otto, S., *"Supramolecular systems chemistry.*" Nature Nanotechnology **2015**, 10, 111-115.
16. Geysen, H. M.; Tainer, J. A.; Rodda, S. J.; Mason, T. J.; Alexander, H.; Getzoff, E. D.; Lerner, R. A., *"Chemistry of antibody binding to a protein."* Science **1987**, 235 (4793), 1184-1186.
17. Bissell, R. A.; de Silva, A. P.; Gunaratne, H. Q. N.; Lynch, P. L. M.; Maguire, G. E. M.; Sandanayake, K. R. A. S., "*Molecular fluorescent signalling with 'fluor–spacer–receptor' systems: approaches to sensing and switching devices via supramolecular photophysics."* Chemical Society Reviews **1992**, 21 (3), 187-195.
18. Bogomolni, R. A.; Stoeckenius, W., *Bacteriorhodopsin: Photosignal transduction and photoenergy transduction in different biological systems.* Journal of Supramolecular Structure **1974**, 2, 775-780.
19. Wasielewski, M. R., *"Photoinduced electron transfer in supramolecular systems for artificial photosynthesis."* Chemical Reviews **1992**, 92 (3), 435-461.
20. Balzani, V.; Sabbatini, N.; Scandola, F., *"Second-sphere" photochemistry and photophysics of coordination compounds".* Chemical Reviews **1986**, 86 (2), 319-337.
21. Tainer, J. A.; Rodda, S. J.*, "The chemistry and applications of metal-organic frameworks."* Science **2013**, 341 (6149), 1230444-12300445.
22. Yaghi, O. M.; Li, G.; Li, H., *"Selective binding and removal of guests in a microporous metal–organic framework."* **Nature** 1995, 378, 703-705.
23. Biradha, K.; Hongo, Y.; Fujita, M., *"Open Square-Grid Coordination Polymers of the Dimensions 20×20 Å: Remarkably Stable and Crystalline Solids Even after Guest Removal."* Angewandte Chemie International Edition **2000**, 39 (21), 3843-3845.
24. Gascon, J.; Corma, A.; Kapteijn, F.; Llabrés i Xamena, F. X., *"Metal Organic Framework Catalysis: Quo vadis?"* ACS Catal. **2014**, 4 (2), 361-378.
25. Lee, J.; Farha, O. K.; Roberts, J.; Scheidt, K. A.; Nguyen, S. T.; Hupp, J. T., *"Metal-organic framework materials as catalysts."* Chem. Soc. Rev. **2009**, 38 (5), 1450-1459.

26. Sumida, K.; Rogow, D. L.; Mason, J. A.; McDonald, T. M.; Bloch, E. D.; Herm, Z. R.; Bae, T.-H.; Long, J. R., *"Carbon Dioxide Capture in Metal–Organic Frameworks."* Chem. Rev. **2012**, 112 (2), 724-781.

27. Kreno, L. E.; Leong, K.; Farha, O. K.; Allendorf, M.; Van Duyne, R. P.; Hupp, J. T., *"Metal–Organic Framework Materials as Chemical Sensors."* Chem. Rev. **2012**, 112 (2), 1105-1125.

28. (a) Férey, G., *"Microporous Solids: From Organically Templated Inorganic Skeletons to Hybrid Frameworks...Ecumenism in Chemistry."* Chemistry of Materials **2001**, 13 (10), 3084-3098; (b) Farrusseng, D.; Aguado, S.; Pinel, C., *"Metal–Organic Frameworks: Opportunities for Catalysis."* Angewandte Chemie International Edition **2009**, 48 (41), 7502-7513.

29. Luz, I.; Llabrés i Xamena, F. X.; Corma, A., *"Bridging homogeneous and heterogeneous catalysis with MOFs: "Click" reactions with Cu-MOF catalysts."* Journal of Catalysis **2010**, 276 (1), 134-140.

30. Luz, I.; Llabrés i Xamena, F. X.; Corma, A., *"Bridging homogeneous and heterogeneous catalysis with MOFs: Cu-MOFs as solid catalysts for three-component coupling and cyclization reactions for the synthesis of propargylamines, indoles and imidazopyridines."* Journal of Catalysis **2012**, 285 (1), 285-291.

31. Andrew Lin, K.-Y.; Hsieh, Y.-T., *"Copper-based metal organic framework (MOF), HKUST-1, as an efficient adsorbent to remove p-nitrophenol from water."* Journal of the Taiwan Institute of Chemical Engineers **2015**, 50, 223-228.

32. Gascon, J.; Aktay, U.; Hernandez-Alonso, M. D.; van Klink, G. P. M.; Kapteijn, F., *"Amino-based metal-organic frameworks as stable, highly active basic catalysts."* Journal of Catalysis **2009**, 261 (1), 75-87.

33. An, B.; Zeng, L.; Jia, M.; Li, Z.; Lin, Z.; Song, Y.; Zhou, Y.; Cheng, J.; Wang, C.; Lin, W., *"Molecular Iridium Complexes in Metal–Organic Frameworks Catalyze CO2 Hydrogenation via Concerted Proton and Hydride Transfer."* Journal of the American Chemical Society **2017**, 139 (49), 17747-17750.

34. Stubbs, A. W.; Braglia, L.; Borfecchia, E.; Meyer, R. J.; Román- Leshkov, Y.; Lamberti, C.; Dincă, M., *"Selective Catalytic Olefin Epoxidation with MnII-Exchanged MOF-5."* ACS Catalysis **2018**, 8 (1), 596-601.

35. Crockett, M. P.; Tyrol, C. C.; Wong, A. S.; Li, B.; Byers, J. A., *"Iron-Catalyzed Suzuki–Miyaura Cross-Coupling Reactions between Alkyl Halides and Unactivated Arylboronic Esters."* Organic Letters **2018**, 20 (17), 5233-5237.

36. Xu, C.; Shen, X.; Hoveyda, A. H., *"In Situ Methylene Capping: A General Strategy for Efficient Stereoretentive Catalytic Olefin Metathesis."* Journal of the American Chemical Society **2017**, 139 (31), 10919-10928.

37. Madrahimov, S. T.; Gallagher, J. R.; Zhang, G.; Meinhart, Z.; Garibay, S. J.; Delferro, M.; Miller, J. T.; Farha, O. K.; Hupp, J. T.; Nguyen, S. T., *"Gas-Phase Dimerization of Ethylene under Mild Conditions Catalyzed by MOF Materials Containing (bpy)NiII Complexes."* ACS Catalysis **2015**, 5 (11), 6713-6718.

38. Vu, T.; Kosslick, H.; Schulz, A.; Harloff, J.; Paetzold, E.; Lund, H.; Kragl, U.; Schneider, M.; Fulda, G., *"Influence of the textural properties of Rh/MOF-5 on the catalytic properties in the hydroformylation of olefins."* Microporous and mesoporous materials **2012**, 154, 100–106.

39. Markert, C., *"High-Throughput Screening in Chemical Catalysis. Technologies, Strategies and Applications."* Angewandte Chemie International Edition **2005**, 44 (15), 2183-2184.

40. Li, Z.; Rayder, T. M.; Luo, L.; Byers, J. A.; Tsung, C.-K., *"Aperture-Opening Encapsulation of a Transition Metal Catalyst in a Metal–Organic Framework for CO2 Hydrogenation."* Journal of the American Chemical Society **2018**, 140 (26), 8082-8085.

41. Rámila, A.; Muñoz, B.; Pérez-Pariente, J.; Vallet-Regí, M., *"Mesoporous MCM-41 as Drug Host System."* Journal of Sol-Gel Science and Technology **2003**, 26 (1), 1199-1202.

42. Ronny, G.; Volodymyr, B.; Andreas, H.; Nicole, K.; Philipp, M.; Ulrich, S.; A., B. I.; Uwe, M.; Irena, S.; Stefan, K., *"Dye Encapsulation Inside a New Mesoporous Metal–Organic Framework for Multifunctional Solvatochromic-Response Function."* Chemistry – A European Journal **2012**, 18 (42), 13299-13303.

43. (a) Morabito, J. V., Li, Z., Byers, J. A., Tsung, C.-K., Boston College, Chestnut Hill, MA, Unpublished work, **2017**, Morabito, J. V., Li, Z., Byers, J. A., Tsung, C.-K., Boston College, Chestnut Hill, MA, Unpublished work, 2017; (b) Hu, P.; Zhuang, J.; Chou, L.-Y.; Lee, H. K.; Ling, X. Y.; Chuang, Y.-C.; Tsung, C.-K., *"Surfactant-Directed Atomic to Mesoscale Alignment: Metal Nanocrystals Encased Individually in Single-Crystalline Porous Nanostructures."* Journal of the American Chemical Society **2014**, 136 (30), 10561-10564; (c) Han, T.-T.; Bai, H.-L.; Liu, Y.-Y.; Ma, J.-F., *"Two host-guest hybrids by encapsulation AlQ3 in zeolitic imidazolate framework-8 as luminescent sensors for Fe3+, CrO42- and acetone."* Journal of Solid State Chemistry **2019**, 269, 588-593.

44. Morabito, J. V.; Chou, L.-Y.; Li, Z.; Manna, C. M.; Petroff, C. A.; Kyada, R. J.; Palomba, J. M.; Byers, J. A.; Tsung, C.-K., *"Molecular Encapsulation beyond the Aperture Size Limit through Dissociative Linker Exchange in Metal–Organic Framework Crystals."* Journal of the American Chemical Society **2014**, 136 (36), 12540-12543.

45. Llabrés i Xamena, F. X.; Abad, A.; Corma, A.; Garcia, H., *"MOFs as catalysts: Activity, reusability and shape-selectivity of a Pd-containing MOF."* Journal of Catalysis **2007**, 250 (2), 294-298.

46. Shieh, F.-K.; Wang, S.-C.; Yen, C.-I.; Wu, C.-C.; Dutta, S.; Chou, L.-Y.; Morabito, J. V.; Hu, P.; Hsu, M.-H.; Wu, K. C. W.; Tsung, C.-K., *"Imparting Functionality to Biocatalysts via Embedding Enzymes into Nanoporous Materials by a de Novo Approach: Size-Selective Sheltering of Catalase in Metal–Organic Framework Microcrystals."* Journal of the American Chemical Society **2015**, 137 (13), 4276-4279.

47. Yan, D.; Tang, Y.; Lin, H.; Wang, D., *"Tunable Two-color Luminescence and Host–guest Energy Transfer of Fluorescent Chromophores Encapsulated in Metal-Organic Frameworks."* Scientific Reports **2014**, 4, 4337.

48. Li, B.; Zhang, Y.; Ma, D.; Ma, T.; Shi, Z.; Ma, S., *"Metal-Cation-Directed de Novo Assembly of a Functionalized Guest Molecule in the Nanospace of a Metal–Organic Framework."* Journal of the American Chemical Society **2014**, 136 (4), 1202-1205.

49. Zhao, S.-N.; Song, X.-Z.; Zhu, M.; Meng, X.; Wu, L.-L.; Feng, J.; Song, S.-Y.; Zhang, H.-J., *"Encapsulation of LnIII Ions/Dyes within a Microporous Anionic MOF by Post-synthetic Ionic Exchange Serving as a LnIII Ion Probe and Two-Color Luminescent Sensors."* Chemistry – A European Journal **2015**, 21 (27), 9748-9752.

50. Zhou, H.-C. J.; Kitagawa, S., *"Metal–Organic Frameworks (MOFs)."* Chemical Society Reviews **2014**, 43 (16), 5415-5418.

51. Burnett, B. J.; Barron, P. M.; Hu, C.; Choe, W., *"Stepwise Synthesis of Metal–Organic Frameworks: Replacement of Structural Organic Linkers."* Journal of the American Chemical Society **2011**, 133 (26), 9984-9987.

52. Kim, M.; Cahill, J. F.; Su, Y.; Prather, K. A.; Cohen, S. M., *"Postsynthetic ligand exchange as a route to functionalization of 'inert' metal-organic frameworks."* Chem. Sci. **2012**, 3 (1), 126-130.

53. (a) Karagiaridi, O.; Bury, W.; Mondloch, J. E.; Hupp, J. T.; Farha, O. K., *"Solvent-Assisted Linker Exchange: An Alternative to the De Novo Synthesis of Unattainable Metal–Organic Frameworks."* Angewandte Chemie International Edition **2014**, 53 (18), 4530-4540; (b) Karagiaridi, O.; Lalonde, M. B.; Bury, W.; Sarjeant, A. A.; Farha, O. K.; Hupp, J. T., *"Opening ZIF-8: A Catalytically Active Zeolitic Imidazolate Framework of Sodalite Topology with Unsubstituted Linkers."* Journal of the American Chemical Society **2012**, 134 (45), 18790-18796.

54. Xu, H.; Cai, J.; Xiang, S.; Zhang, Z.; Wu, C.; Rao, X.; Cui, Y.; Yang, Y.; Krishna, R.; Chen, B.; Qian, G., *"A cationic microporous metal–organic framework for highly selective separation of small hydrocarbons at room temperature."* Journal of Materials Chemistry A **2013**, 1 (34), 9916-9921.

Chapter 2. Molecular Encapsulation beyond the Aperture Size Limit through solvent-assisted Linker Exchange in Metal-Organic Frameworks

2.1 Incorporating guest molecules in MOF by aperture-opening encapsulation

As mentioned previously, constructing a host-guest system using MOF chemistry is widely applicable in various cross-disciplinary fields.[1] This chapter is primarily focused on the invention of aperture-opening encapsulation strategy which is pioneered by Dr. Joseph Morabito and Dr. Randy Chou. My contribution to the study is mainly in the development of Eyring analysis to provide an independent means for verifying the hypothesis that the reaction is proceeding by a competition between associative and dissociative linker exchange process. Some of the most pertinent results from Dr. Joseph Morabito and Dr. Randy Chou will be provided to legitimize the efforts described in Chapters 3-5. Also, the investigation into the mass transport associated with different MOF particle sizes are attempted.

Incorporation of guest molecules in MOFs by diffusion is generally limited to guests that are smaller than the MOF aperture size,[2] and this limitation commonly leads to guest molecule leaching. Retaining guests in the cavity of MOFs by pursuing strategies that incorporate guests larger than the MOF aperture size could circumvent this problem. Two strategies for this are the ship-in-a-bottle assembly of the guest within the pore subunits and the *de novo* encapsulation of the guest during MOF crystal growth.[3] However, they are limited in either multiple postsynthetic operations or challenged in compatibility with MOF synthesis. The development of an alternative encapsulation approach is in high demand.[4]

It has been reported that the bridging organic ligands in MOF crystals can be exchanged with compatible but chemically distinct ligands without disrupting the underlying MOF crystal structure and morphology. This phenomenon was first reported by Choe for pillared porphyrin paddlewheel frameworks[5] and has been optimized by several groups.[6] The ligand exchange process has become extremely popular for the diversification of MOFs and is most commonly referred to as solvent-assisted linker exchange (SALE)[6a] or postsynthetic exchange (PSE).[6b]

A new concept for incorporating larger and more diverse guest molecules into MOFs is introduced by taking advantage of ligand exchange reactions to "open" part of the framework of the pre-synthesized MOF crystals (Figure 2-1). Expanded apertures created by the ligand exchange process allow large guest molecules to diffuse into the MOF pore. After guest incorporation, association of the ligand closes the large aperture, trapping the guest molecule in the MOF pore. This new approach to guest incorporation is expected to be general as framework ligand exchange has been carried out under various conditions and exists in a large number of MOFs with diverse secondary building units.[5-7] An additional practical advantage of decoupling encapsulation and MOF synthesis is that MOF production can be scaled-up independently of guest loading, which is especially relevant since several MOFs, such as ZIF-8, Fe-BTC, HKUST-1, and MIL-53(Al), have been become commercially available. Recently, UiO-66 has been commercialized by BASF and STREM.

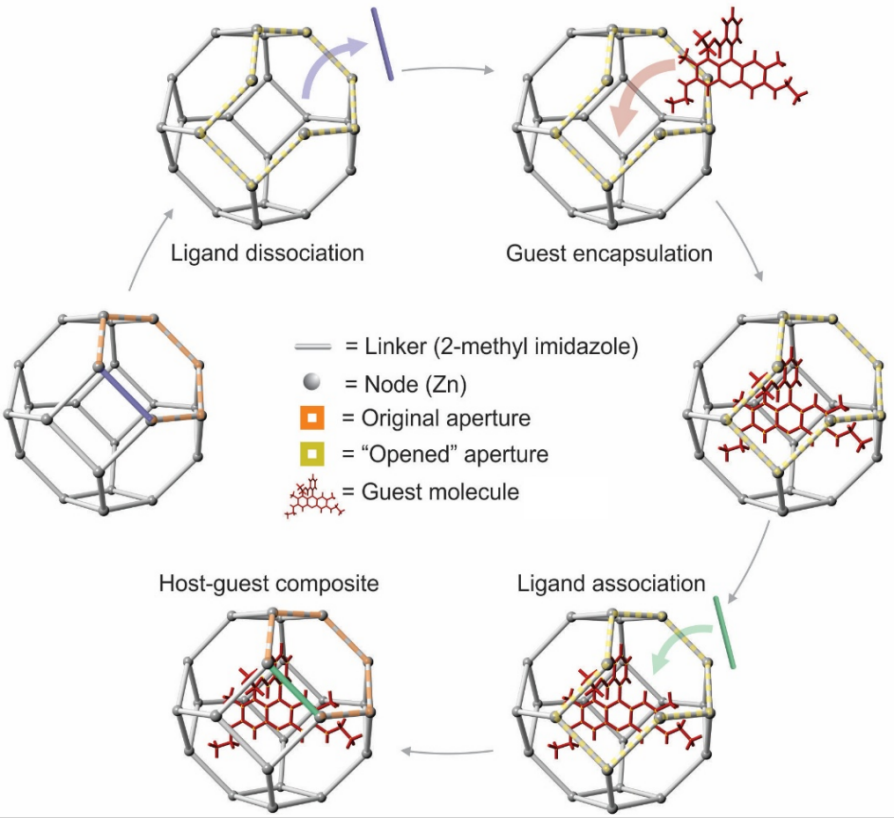

Figure 2-1. Molecular encapsulation of a large organic guest into the pores of ZIF-8 through dissociative linker exchange.

The ability for ligands to exchange between metal centers is ubiquitous in coordination chemistry, where the two limiting mechanisms for ligand substitution reactions are associative or dissociative mechanisms. In a MOF, the metals are typically coordinatively saturated, a property that we reasoned would make a dissociative mechanism more likely. If dissociative linker substitution occurs in MOFs, we hypothesized the existence of short-lived linker vacancies, which would momentarily expand the pore aperture size to allow the passage of larger guests into the framework. Subsequent reincorporation of the dissociated linker reassembles the MOF with an aperture size that is smaller than the incorporated guest.

2.2 Encapsulation of Rhodamine 6G into ZIF-8 under linker exchange conditions

As a proof of principle, the commercially available zeolitic imidazolate framework (ZIF-8) was used as a model MOF. A suitable guest molecule should meet two criteria. First, to maximize guest retention, the guest molecule should be larger than the MOF aperture size but smaller than its pore size. For encapsulation in ZIF-8, this requirement makes the ideal guest size between ~ 3.4 and 11.6 Å, the aperture and pore sizes of ZIF-8, respectively. Second, in order to better quantify the loading, the guest molecules should be easily detectable by UV-Vis spectroscopy. Rhodamine 6G (R6G) was selected as an ideal candidate that meets both criteria outlined above: it is a fluorescent dye (λ_{max} = 530 nm) with a molecular diameter of 11.3 – 13.7 Å (Figure 2-2). The amounts of encapsulated R6G are determined by UV-Vis spectroscopy after acid digestion of the ZIF-8 crystals in methanol.

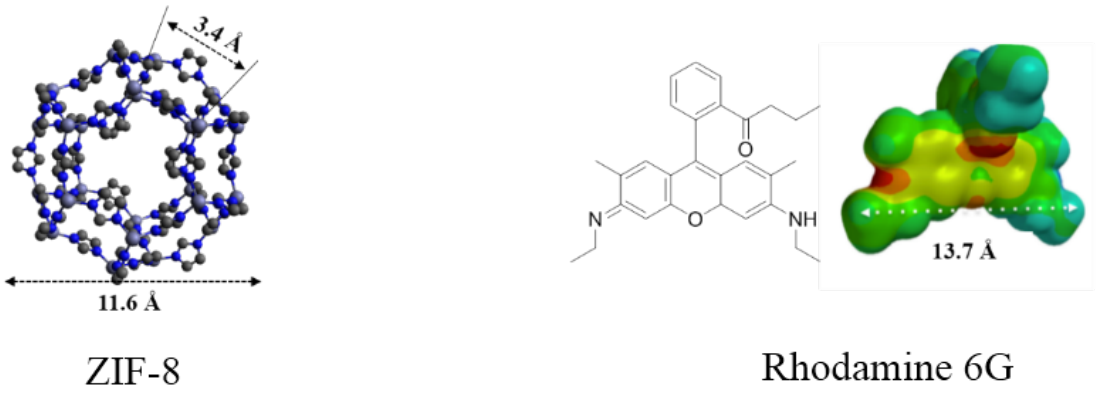

Figure 2-2. The molecular dimensions of the host ZIF-8 and the guest molecule Rhodamine 6G.

To test whether linker exchange can facilitate guest incorporation, R6G was incubated with ZIF-8 in the presence of 2-methylimidazole as an exogenous linker in n-butanol at 100 °C

for 7 days (Figure 2-3). Exchange of the 2-methylimidazole linker in ZIF-8 with imidazole has been reported under these conditions.[7a] After the reaction, the material, henceforth referred to as R6G@ZIF-8, took on a cloudy light pink hue. The structure of the guest encapsulation products was characterized by transmission electron microscopy (TEM) and powder X-ray diffraction (PXRD). Both techniques showed no apparent differences after guest encapsulation, suggesting that the guest loading method was not destructive to the MOF structure (Figures 2-4 and 2-5).

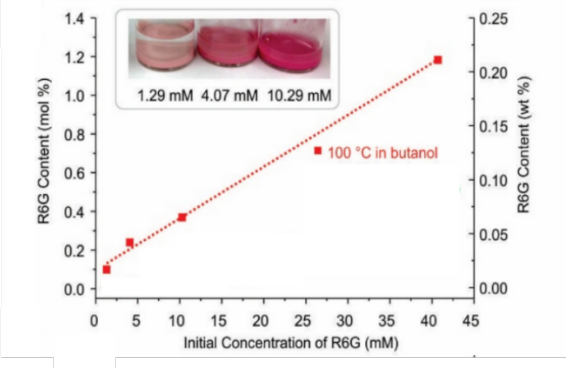

Figure 2-3. Rhodamine 6G encapsulation through ZIF-8 linker exchange. Condition: 10.29 mM of R6G at 100 ºC in *n*-butanol for 7 d.

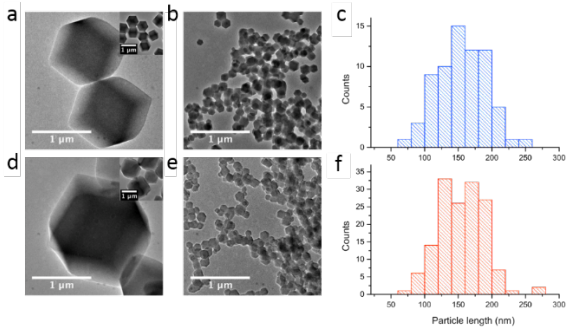

Figure 2-4. Transmission electron microscope (TEM) images and particle size distributions (PSDs) of ZIF-8 crystals a) as synthesized (micron-sized), b) as synthesized (nano-sized), c) PSD of as synthesized (nano-sized), d) after R6G loading (micron-sized), e) after R6G loading (nano-sized), and f) PSD of after R6G loading (nano-sized). The loading was carried out with 10.3 mM R6G at 100 °C for 7 days in *n*-butanol.

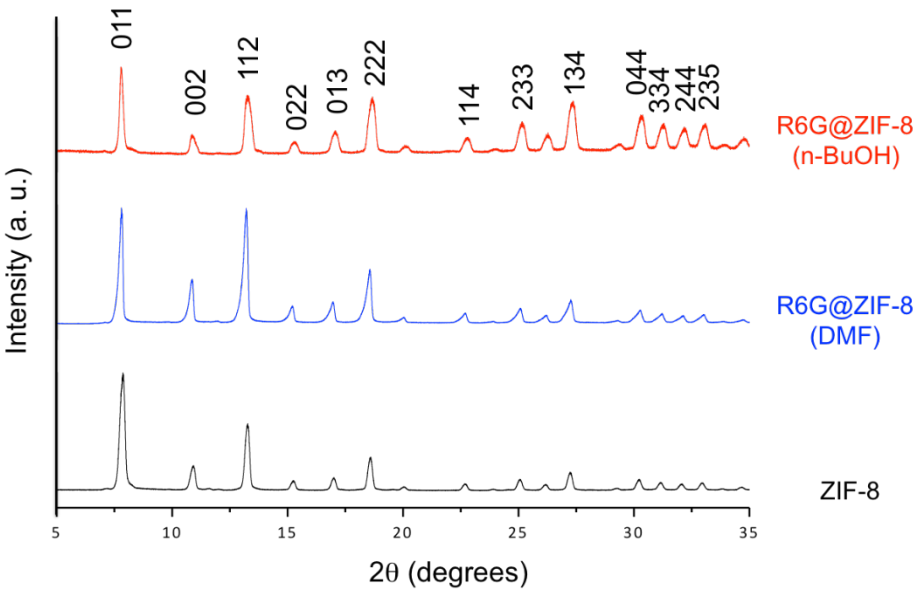

Figure 2-5. Powder X-ray diffraction patterns of R6G@ZIF-8. The R6G loading was carried out with 10.3 mM R6G at 100 °C for 7 days in *n*-butanol (red) and in DMF (blue). The pattern for pure ZIF-8 crystals (black) is given for reference below.

2.3.1 Encapsulated versus surface bond Rhodamine 6G

To confirm that the R6G is indeed incorporated in ZIF-8 instead of attaching to its surface, a method was sought out to remove the surface bound R6G in all samples prior to UV-Vis analysis. Briefly exposing ZIF-8 to R6G at room temperature led to the coloration of the MOF, despite linker exchange not occurring to an appreciable extent (Figure 2-6). The affinity of R6G for ZIF-8 likely arises from its ester and amine functional groups, which can interact with the hydrophilic external surfaces of ZIF-8. To remove surface bound R6G from ZIF-8, the samples were washed with methanolic solutions of polyvinylpyrrolidone (PVP), a polar polymer with poly-ketone functional groups that interact strongly with MOF crystals due to the polyvalency effect.[8] Due to its large size, PVP cannot penetrate the interior of ZIF-8. Therefore, any R6G that remains associated with ZIF-8 after PVP washing is likely trapped in the pores of ZIF-8 rather than on its surface. As expected,

repeated washings of R6G@ZIF-8 with PVP led to the liberation of some R6G, but after repeated PVP washings, the pink color of R6G@ZIF-8 remained (Figure 2-7). Analysis of the PVP washed R6G@ZIF-8 by UV/Vis allowed for the encapsulation efficiency of R6G in R6G@ZIF-8 to be quantitatively determined. A similar PVP washing procedure carried out under conditions where linker exchange does not occur led to full removal of R6G from the ZIF-8 crystals (Figure 2-7).

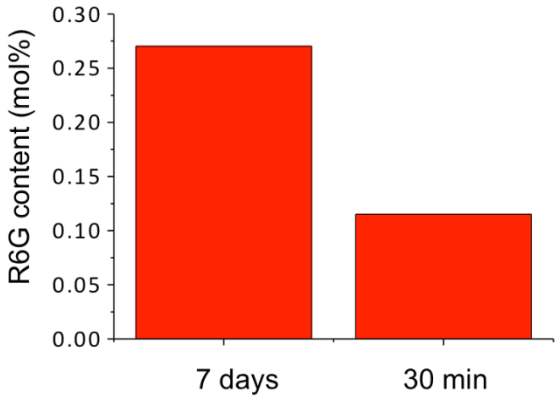

Figure 2-6. ZIF-8 surface interaction experiments. Loading of R6G for 7 days and 30 minutes. All other R6G loading parameters were the same (10.3 mM R6G, *n*-butanol, 25 °C).

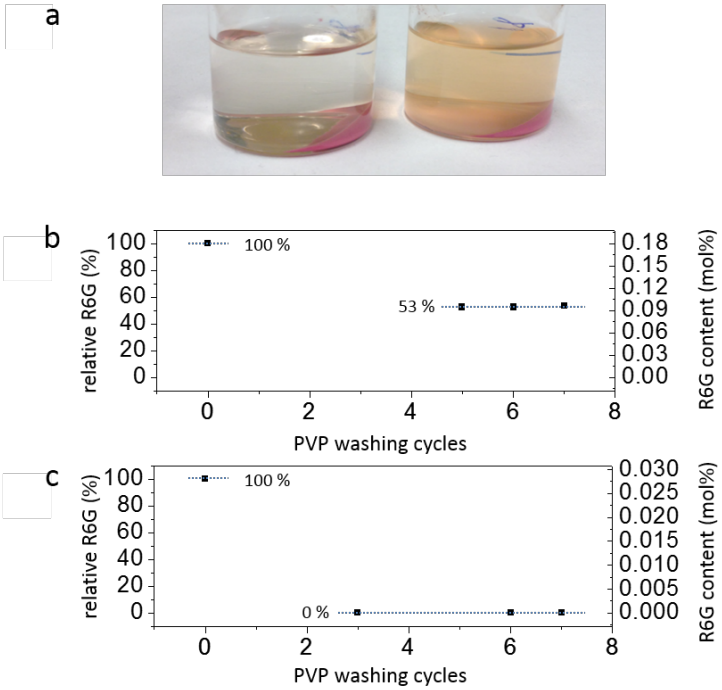

Figure 2-7. PVP washing experiments. a) Digital photograph of R6G@ZIF-8 precipitates and supernatants after centrifugation: (left) as synthesized R6G@ZIF-8 after 5 times methanol washing and (right) methanol-washed R6G@ZIF-8 re-suspended in 14 wt. % PVP/methanol solution. Surface bound R6G was washed by PVP solution. In b) and c), R6G content tracking by absorbance after PVP washing cycles. The R6G loading was carried out with 1.29 mM R6G in *n*-butanol at b) 100 °C for 7 days, and c) 25 °C for 10 min.

To further confirm that the R6G is encapsulated in ZIF-8 during linker exchange, comparison was carried out between fluorescence intensity of the sample prepared by linker exchange in n-butanol with R6G, the sample prepared by brief exposure of ZIF-8 to the R6G, and free R6G in solution (Table 2-1). After the fluorescence intensities were normalized by the amount of the R6G in the samples, a significant decrease in fluorescence intensity was observed for the linker exchange sample. The normalized intensity for surface bound R6G was more than double than the linker exchange sample, while fluorescent lifetimes (τ) were approximately the same for all samples. The origin of the low intensity

is likely due to the encapsulation. The difference in intensity has further supported that R6G is indeed encapsulated in ZIF-8 during the linker exchange instead of bound to the external ZIF-8 surface.

Table 2-1. Fluorescence lifetime and fluorescence intensity measurement. R6G@ZIF-8 samples prepared with 147 mM 2-methylimidazole exogenous linker (+ Hmim) and without any exogenous linker (no exog.) in n-butanol. Both R6G@ZIF-8 samples were PVP washed to remove surface bound dye as described in the main text. The R6GonUiO-66 was prepared by exposing ZIF-8 particles to R6G in a methanolic solution for 10 min, followed by extensive (5x) washing with methanol. In previous control experiments we found that PVP washing of a sample prepared this way led to complete removal of the dye, demonstrating that dye loading is solely on the surface. The fluorescence intensities were normalized by the amount of the R6G loading measured by absorption after the ZIF-8 particles were digested by acid. The R6G standard consisted of R6G dissolved in methanol with a UV-vis absorbance of 0.3 a.u..Last entry was measured under the condition where no exogenous imidazole was added.

SAMPLE	wt% R6G	τ (ns)	I /A (A.U.)	I / A NORMALIZED
R6G	-	2.84 ± 0.14	18800 ± 100	1.0
Surface only control	0.023	3.63 ± 0.10	1800 ± 40	0.096
R6G@ZIF-8 +HMIM	0.024	3.50 ± 0.03	790 ± 6	0.042
R6G@ZIF-8 No exog.	0.064	3.79 ± 0.02	195 ± 3	0.010

2.3.2 Investigating parameters affecting Rhodamine 6G encapsulation

2.3.2.1 Temperature and solvent

After R6G was removed from the surface, the effects of temperature, solvent, and initial concentration of R6G on encapsulation in ZIF-8 were studied (Figure 2-8). This study indicated that guest loading was temperature and solvent dependent. For instance, n-butanol facilitated the encapsulation more than acetonitrile at the same temperature. Higher encapsulation was observed at higher temperatures due to increased linker exchange rates.

As expected for diffusion-controlled guest incorporation, R6G loading was found to be dependent on the initial concentration of R6G. Re-subjecting R6G@ZIF-8 to the linker exchange reaction conditions without exogenous R6G led to diffusion of the dye into solution (Table 2-2). The leaching can be prohibited by using the conditions that do not promote linker exchange (Table 2-2).

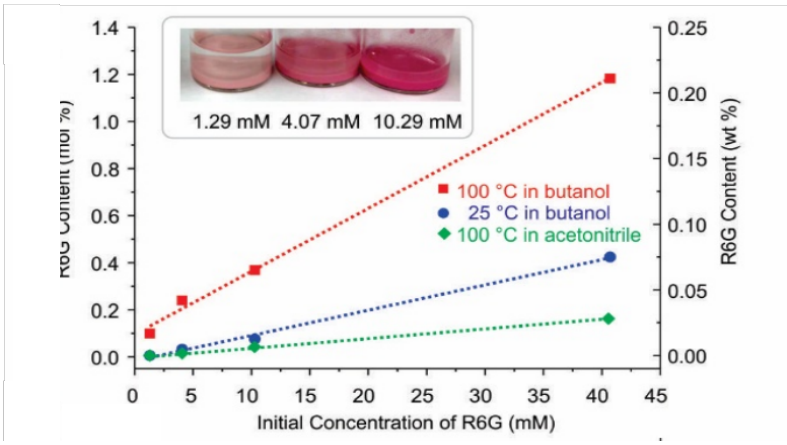

Figure 2-8. Rhodamine 6G encapsulation through ZIF-8 linker exchange (7 days). R6G loading versus [R6G] at 100 °C (red) and 25 °C (blue) in *n*-butanol and at 100 °C in acetonitrile (green). Inset image shows ZIF-8 after R6G loading at various [R6G] during linker exchange at 100 °C in *n*-butanol

Table 2-2. Leaching experiment. (a) the original R6G@ZIF-8 prepared under linker-exchange condition, (b) Re-subjecting R6G@ZIF-8 to the linker exchange condition at elevated temperature without exogenous linker, (c) Re-subjecting R6G@ZIF-8 to non-linker exchange condition at room temperature with exogenous linker.

ENTRY	SAMPLE	PREPARATION	LOADING
(A)	Original R6G@ZIF-8	10.29 mM R6G, BuOH at 100 °C for 7days	0.370 mol (%)
(B)	Under linker-exchange condition	BuOH at 100 °C for 7days	0.027 mol (%)
(C)	Under non-linger-exchange condition	2.2 mmol 2-methylimidazol MeOH at 20 °C for 1 month	0.340 mol (%)

2.3.2.2 Exogenous linker concentration

The effect of exogenous 2-methylimidazole linker concentration had on guest loading was explored next. Somewhat surprisingly, R6G loading was inversely proportional to the concentration of 2-methylimidazole linker (Figure 2-9). In fact, the highest loading of R6G was observed when reactions were carried out without any exogenous 2-methylimidazole linker. Although unexpected, this result was rationalized by a dissociative linker substitution mechanism where dissociation of 2-methylimidazole from ZIF-8 led to the formation of a linker-deficient "open" state (Figure 2-1). Under low concentrations of free imidazole, the "open" state is not as readily arrested by free linker, which provides more time for the guest to diffuse into the pores of the MOF. Consequently, higher guest loadings are observed at lower concentrations of the exchanging linker. The aforementioned leaching experiment also suggested exogenous linker and low temperature shut down dissociative linker substitution reaction pathway.

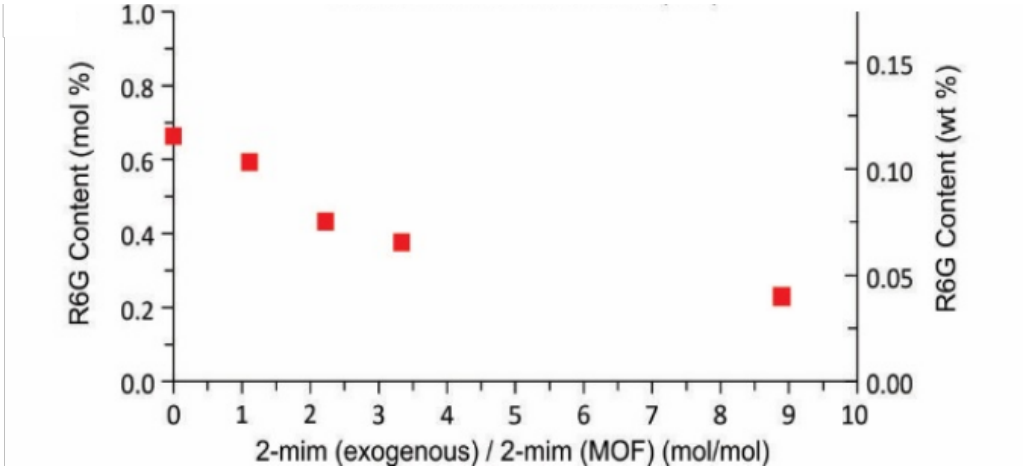

Figure 2-9. Dependence of R6G encapsulation on the [2-methylimidazole] exogenous linker. Conditions: 10.29 mM of R6G at 100 ºC in *n*-butanol for 7 d.

2.4 Linker exchange mechanistic study

2.4.1 Kinetic measurements

The development of the first quantitative kinetic method for studying MOF linker exchange reactions and the application of this method to understand the solvent dependence of ZIF-8 and imidazole is described in detail in Dr. Joe Morabito's Ph.D. dissertation. This part of chapter 2 serves as a summary of major findings from Dr. Joe Morabito and Dr. Randy Chou's work.

To test the hypothesis that linker substitution is dissociative, Dr. Joseph Morabito and Dr. Randy Chou, particularly pioneered by Joseph examined the kinetics of the linker exchange reaction under pseudo-first order conditions by varying the initial concentration of exogenous imidazole linker (See Experimental Section). The observed rate (k_{obs}) for the linker exchange reaction could be obtained by using the method of initial rates (< 10% conversion) of multiple parallel reactions stopped at different time. By plotting k_{obs} versus [imidazole] ([im]), they observed a linear correlation with a non-zero slope and intercept (representative ^{1}H-NMR spectra in Figure 2-10, conv. vs. t plots in Figure 2-11, and k_{obs} values in Table 2-3, k_{obs} vs. [im] in Figure 2-12,). These data suggest that there is a competition between associative and dissociative linker substitution reactions with the slope of this line (m = 38.6 x 10^{-6} M^{-1}•s^{-1}) being the second order rate constant for associative exchange, and the intercept (b = 3.37 x 10^{-6} s^{-1}) being the first order rate constant for dissociative exchange. Under the empirically determined conditions employed for linker exchange ([im] = 147 mM), the apparent rate constant for associative linker substitution ($k_{app}(s^{-1}) = k_a$•[im]) is 5.67 x 10^{-6} s^{-1}, which is similar to the first order rate constant for dissociative linker exchange. Importantly, under the conditions that worked

best to maximize guest incorporation ([im] = 0), the associative exchange mechanism was completely shut down, indicating that linker exchange occurs from a competition between associative and dissociative pathway under conditionally typically employed for linker exchange reactions in ZiF-8. Indeed, the lower guest incorporation at higher linker concentrations may be due to a competing associative exchange process that precludes the formation of an "open" state for guest incorporation. These studies clearly reveal the mechanistic complexity of the process. Besides exogenous linkers, the solvent dependency of the incorporation of R6G dye into MOF clearly indicates the solvent-assisted linker exchange property. Hence, rate measurements made for the exchange of imidazole into ZIF-8 demonstrated a complicated dependency on the imidazole concentration, which could be related to the existence of at least three distinct reaction mechanisms: a) a dissociative pathway that predominates at low imidazole concentration and only for protic solvents, b) a faster associative process that is first order in imidazole and is relatively solvent independent, and c) a pathway that has a kinetic order in imidazole that is greater than one and that is highly dependent on the hydrogen bond donating ability of a solvent. (Figure 2-13). An alternative interpretation of the data besides pathway a is that the reaction is always dissociative, and the linear plot of k_{obs} vs. [im] is due to the reassociation of the ligand being the rate determining step of the dissociative pathway. However, the fact that we never observed saturation kinetics at high linker concentrations is more consistent with an associative linker exchange mechanism as opposed to dissociative process. In summary, we conclude linker exchange in ZIF-8 goes through a competition between at least 2 pathways. One of these has first order or higher dependence in linker and doesn't allow for guest encapsulation. The other occurs only in protic solvents and allows for guest

encapsulation via long-lived missing-linker defects. Both pathways are strongly solvent-dependent and both are fastest in protic solvents.

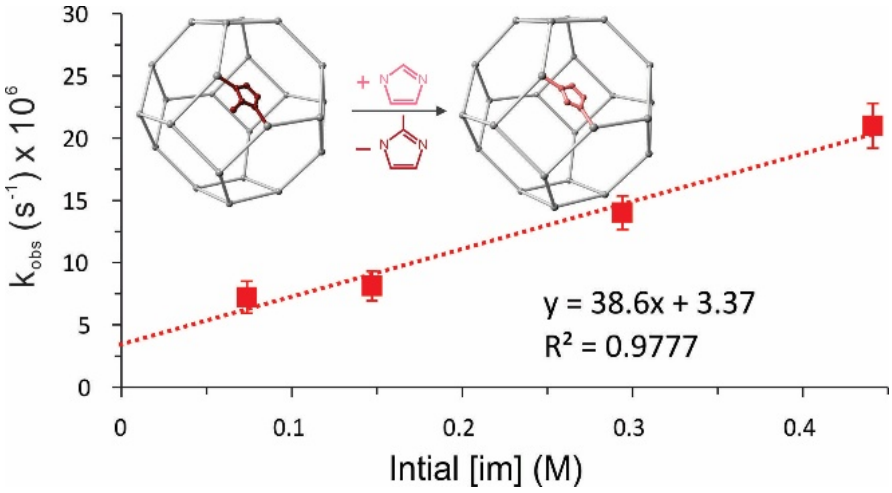

Figure 2-12. Observed rate constants (k_{obs}) for exchange of ZIF-8 with imidazole at different concentrations of imidazole.

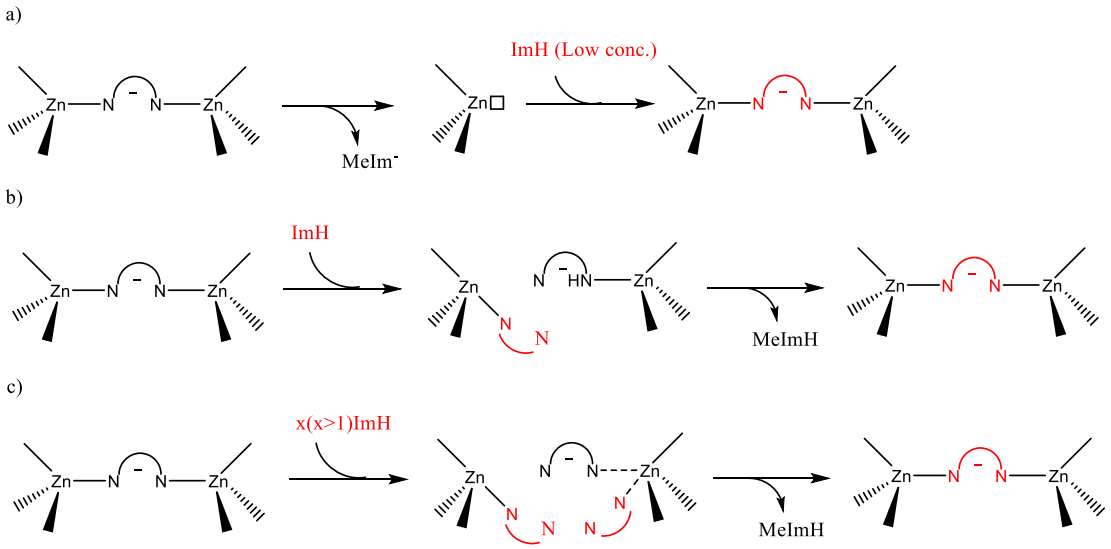

Figure 2-13. Three hypothetical mechanism pathways a) a dissociative pathway at low ImH concentration, b) an associative pathway first order in ImH, c) an associative pathway higher than first order in ImH.

2.4.2 Eyring analysis on linker exchange reactions

The experiments were carried out to provide an independent means for verifying the hypothesis that the reaction is proceeding by a competition between associative and dissociative linker exchange process. Doing so requires treating the dissociative and associative regions separately. Linker exchange in ZIF-8 was carried out with exogenous imidazole in n-BuOH at different temperatures. The product after partial linker exchange is denoted SALEM-2.[9] The level of conversion was kept under 10% to prevent the formation of a *zni* phase, which can form with high imidazole incorporation.[10]

The Eyring equation is widely used in chemical kinetics to describe the variance in the rate of a chemical reaction with changing temperature.

$$\mathrm{k} = \frac{k(\mathrm{k_b})T}{h} e^{\frac{\Delta S^{\ddagger}}{R}} e^{\frac{-\Delta H^{\ddagger}}{RT}} \qquad \text{(Eq. 1)}$$

The equation can be written in this following form as well.

$$\ln\frac{k}{T} = \frac{-\Delta H^{\ddagger}}{R} \cdot \frac{1}{T} + ln\frac{k(\mathrm{k_b})}{h} + \frac{\Delta S^{\ddagger}}{R} \qquad \text{(Eq. 2)}$$

where k is the reaction rate constant, T is the absolute temperature, $\Delta H^{\ddagger}$ is the enthalpy of activation, $\Delta S^{\ddagger}$ is the entropy of activation, R is the ideal gas constant, $\mathrm{k_b}$ is Boltzmann constant and h is Planck's constant. The kinetics underpinning a chemical reaction, such as the enthalpy of activation ($\Delta H^{\ddagger}$) and the entropy of activation $\Delta S^{\ddagger}$), can be derived from this form of the Eyring equation.

The plot of conversion vs time for associative and high imidazole concentration ([im]=0.441 M) and low imidazole concentration ([im]=0.0294 M) was acquired from ^{1}H-NMR (T_1=13 s) analysis of reactions at different time (Figure 2-14). Each kinetic

experiment was repeated at least three times to improve the accuracy. Slopes of the fitting from linear regression was the observed rates for reactions (Table 2-4). Those data indicated the rate of reaction increased with temperature and the concentration of exogenous imidazole.

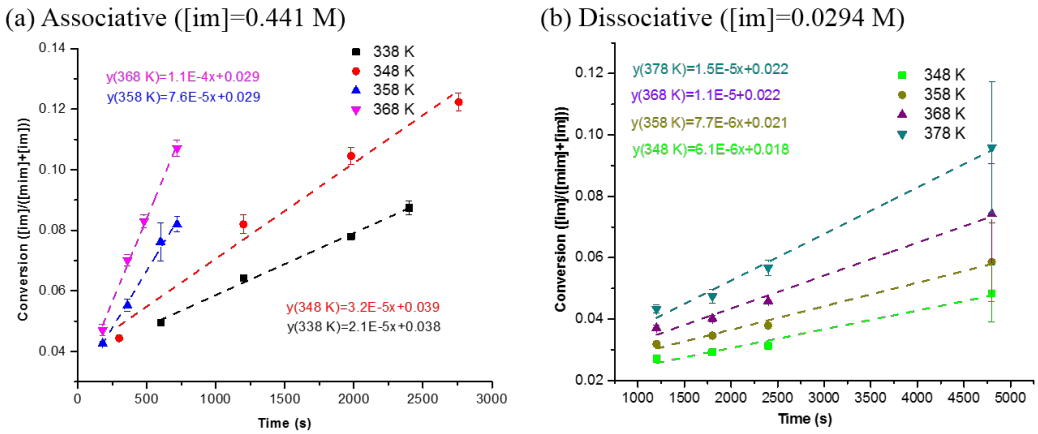

Figure 2-14. Plot of conversion vs. time of the $Zn(mim)_2$ to $Zn(mim)_{2-x}(im)_x$ exchange reaction at varying temperature, with conversion expressed as the appearance of imidazole in the framework as a molar fraction of the total imidazolate linker content of the solid. (a) Exogenous [im]=0.441 M. (b) Exogenous [im]=0.0294 M. Least squares linear regressions are shown.

Table 2-4. The observed rates (k_{obs}) determined by the method of initial rates (k_{obs} = slope m) from the conversion vs. time plots in Figure 2-13, with the coefficients of determination (R^2) for each linear fit.

[im]=0.441M	**k_{obs} (s^{-1})**	**R^2**	**[im]=0.0294M**	**k_{obs} (s^{-1})**	**R^2**
338K	2.05E-5	0.9931	348 K	6.11E-6	0.9971
348 K	3.16E-5	0.9706	358 K	7.66E-6	0.9865
358 K	7.55E-5	0.9904	368 K	1.07E-5	0.9902
368 K	1.10E-4	0.9935	378 K	1.52E-5	0.9881

Plots of ln(k_a/T) vs. 1/T were then made for both the associative region ([im]=0.441 M) and the dissociative region ([im]=0.0294 M) using the rate constants k_a calculated from dividing k_{obs} by the concentration of exogenous imidazole ([im]), as detailed above (Figure 2-15). The calculated activation parameters $\Delta H^{\ddagger}$ and $\Delta S^{\ddagger}$ from the Eyring plots show a notable difference from the associative to dissociative regions, which is consistent with our hypothesis of a mechanism change as the exogenous linker concentration increases. $\Delta H^{\ddagger}$ of the associative reaction (13.935 kcal/mol) is almost twice that of the dissociative (7.269 kcal/mol). The negative sign of $\Delta S^{\ddagger}$ (-32.0 kcal/K*mol) for the associative region is consistent with the aforementioned mechanism, though it remains unclear why a negative entropy is derived from the dissociative region (-33.4 kcal/K*mol). In principle, the dissociative pathway should have a positive entropy due to the increase of freedom after linker being dissociated from the framework. The more negative entropy of activation ($\Delta S^{\ddagger}$) may arise from the high entropic cost of solvent reorganization in the transition state, such as to stabilize a buildup of charge.

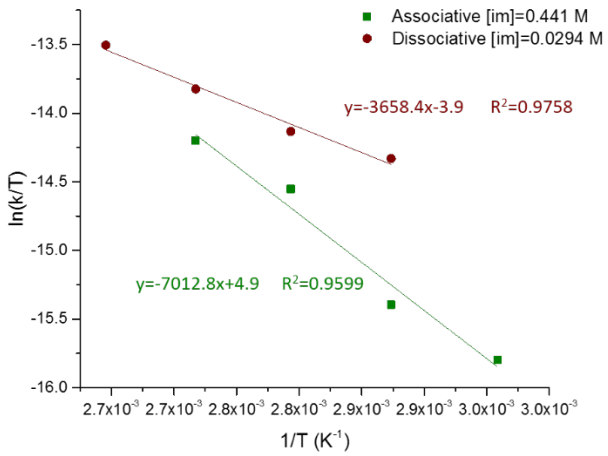

Figure 2-15. Eyring plot ln(k_a/T) vs. 1/T for associative region and dissociative region and the calculated activation parameters $\Delta H^{\ddagger}$ and $\Delta S^{\ddagger}$ from Eyring plot.

2.4.3 Understanding mass transport in linker exchange kinetics

Mass transport is a challenge in obtaining mechanistically relevant kinetic information for reactions occurring in porous solids, since slow diffusion within the pores may cause the reaction to be rate limited by the mass transport.[11]

In principle, mass transport is crystal size dependent while kinetics is not. To determine if kinetics for linker exchange rather than diffusion, bond breaking and forming, were being obtained, we measured and compared the exchange rates of imidazole with ZIF-8 of different crystal sizes in the solvent 1-butanol (BuOH). To minimize the possibility of interference from diffusion, all kinetic measurements were carried out using initial rates early on in the linker exchange process (<10 %).[12] Size-controlled ZIF-8 samples ranging from 80 nm to 10 um in average diameter (Figures 2-16, Table 2-5) were synthesized by varying the ratio between $Zn(NO_3)_2$ and 2-methylimidazolate. Figure 2-16 shows the particle size distributions obtained from TEM images of size controlled ZIF-8 particles shown as counts versus grain diameter d, and the statistics analysis are shown in Table 2-5. The observed rate constant (k_{obs}) for exchange was measured for each size at high (0.294 M) and low (0.0735 M) concentrations of exogenous imidazole ([ImH]) in BuOH at 70 °C. k_{obs} versus the log of crystal diameter (Figure 2-17) was plotted to understand if there is any correlation between k_{obs} and diffusion rate at different crystal sizes.

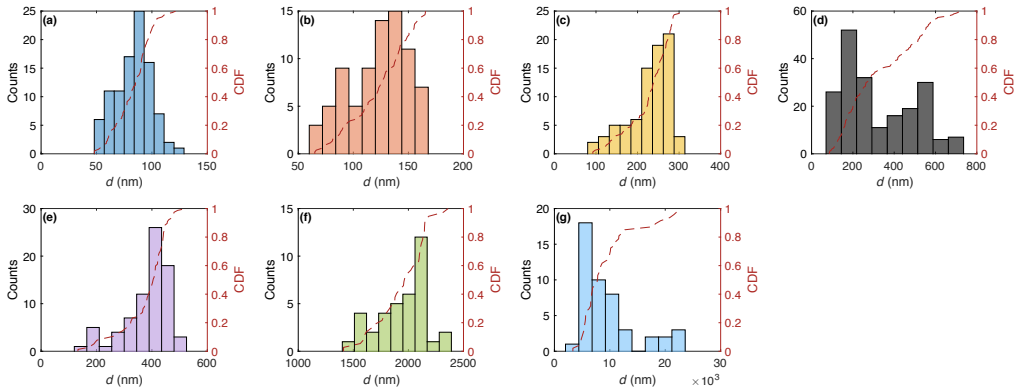

Figure 2-16. Particle size distributions obtained from TEM imaging of size-controlled ZIF-8 particles shown as counts versus grain diameter, *d*, in nm, CDF = cumulative distribution function of the particle volume distribution (equal to weight for constant density).

Table 2-5. The parameters obtained from the particle size distributions in Figure 2-11. Average grain diameter, d_{ave}, is the mean of the number distribution of grain diameters. D10, D50, and D90 are the corresponding *d* values of the mass-weighted cumulative distribution functions in Fig. 2-11 at CDF = 0.1, 0.5, and 0.9 respectively. In other words, 10 % of the particles have grain diameters less than D10, 50 % are smaller than D50, and 90 % are smaller than D90. D50 is also referred to as the mass median diameter.

Entry	Sample	D_{ave}(nm)		Std dev (nm)	D_{10}(nm)	D_{50} (nm)	D_{90} (nm)
(A)	M	83	±	16	60	85	102
(B)	L	123	±	27	81	125	155
(C)	XL	229	±	51	140	239	282
(D)	Basolite Z1200	324	±	173	130	265	565
(E)	XXL	382	±	82	251	404	455
(F)	2 µm	1946	±	224	1598	1963	2149
(G)	10 µm	9485	±	5151	4960	7755	18528

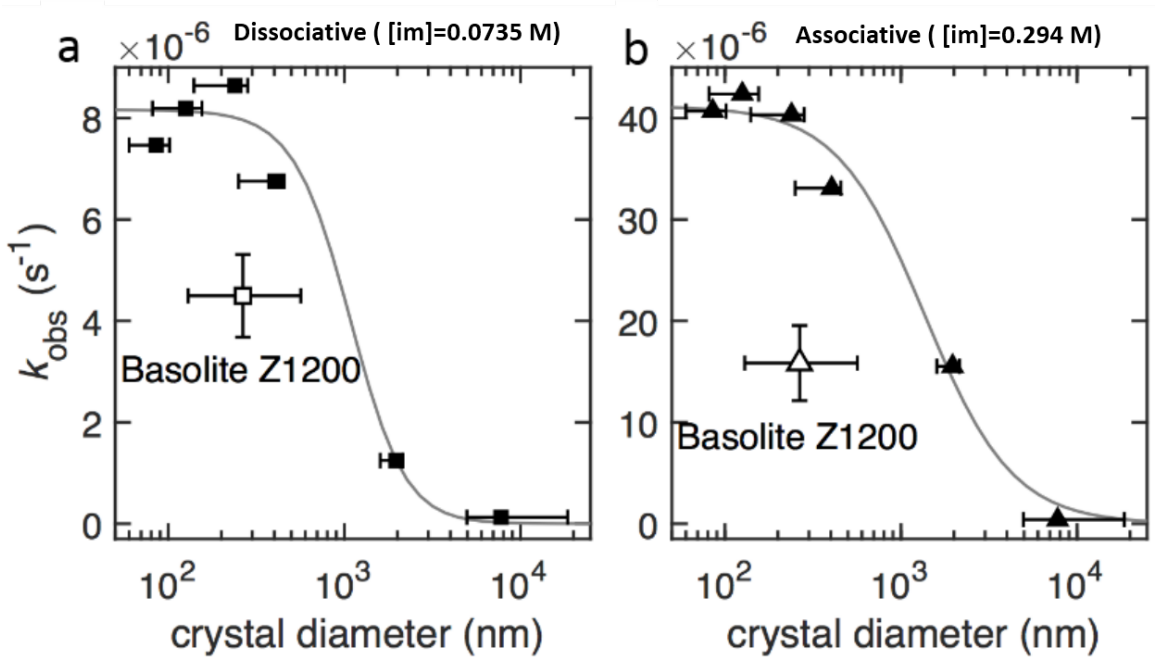

Figure 2-17. The dependence of linker exchange kinetics on ZIF-8 crystal size as measured in *n*-butanol at 70 °C with (a) 0.0735 M and (b) 0.294 M imidazole. Data are plotted for size-controlled (filled symbols) and commercially obtained (open symbols) ZIF-8. Crystal diameter values come from statistical analysis of transmission electron micrographs, scaling the number distribution of grain diameters to a volume (weight) distribution. The *x*-values are the mass median diameters (D_{50}) of the crystal grain size distribution, and *x*-error bars represent the span of the distribution from 10 % (D_{10}) to 90 % (D_{90}) of the distribution by weight. The lines are meant to guide the eye and do not represent a mathematical fit to the data. Uncertainty in k_{obs} for Basolite Z1200 indicates the 99 % confidence interval.

The plots show a partial dependency of k_{obs} on crystal diameters. k_{obs} is independent of crystal sizes until the size increases to around 400 nm and K_{obs} is gradually affected by the crystal sizes when size further increases to micrometer region. The commercial ZIF-8 particles with the size around 200 nm is in the region where k_{obs} is not completely diffusion controlled. Although these values indicate that under these conditions reaction kinetics are not fully uncoupled from mass transport, valuable mechanistic information could still be garnered from measurements on this material due to the still substantial contribution of intrinsic kinetics to the overall rate. Our methodology used initial rates early on in the

linker exchange process (< 10 %), which stops the reaction before the product layer can become too thick, making transport through it rate limiting. In particular, trends in the kinetic orders in imidazole obtained from the shape of k_{obs} vs. [ImH_0] plots (Figure 2-9) should still be valid if the exchange kinetics in other solvents also show comparably steady contributions from diffusion over the range of imidazole concentrations as in n-BuOH. We note that the absolute rate constants obtained above do not reflect the elementary rate constants for the reactions because they are a composite result from diffusion and the mechanism for linker exchange.

2.5 Construction of [Rh, PPh_3]@ZIF-8 for catalysis.

The construction of host-guest catalytic system was attempted by the incorporation of a transition metal complex in ZIF-8 under linker exchange conditions. In all previous instances of *ship-in-a-bottle* complex synthesis, the metal cation serves as the initial subunit that is encapsulated in the MOF via electrostatic interactions.[13] Subsequent to metal loading, ligands smaller than the aperture size of the MOF are added to form a transition metal complex. In contrast to the anionic MOFs, the neutral pores of ZIF-8 offer no similar means to immobilize metal ions electrostatically. Since our approach allows sufficiently bulky ligands to be encapsulated and retained, a neutral ligand could be encapsulated in ZIF-8. Complexation of the incorporated ligand could then be carried out in a subsequent step by using transition metal ion precursors that could easily diffuse into the MOF.

Triphenylphosphine (PPh_3) (molecular diameter = 9.56 Å) was chosen as the initial guest ligand, because of its ubiquity in organometallic catalysis and its appropriate molecule size (Figure 2-18). The same method used for dye encapsulation was adopted to encapsulate PPh_3 in ZIF-8 (henceforth referred to as PPh_3@ZIF-8) using initial [PPh_3] of 165 mM and

220 mM. Elemental analysis of the product obtained with an initial [PPh_3] of 220 mM indicated a PPh_3 loading of 2 wt. % (Figure 2-19). Based on PXRD, PPh_3@ZIF-8 had the same crystal structure as pristine ZIF-8 (Figure 2-20).

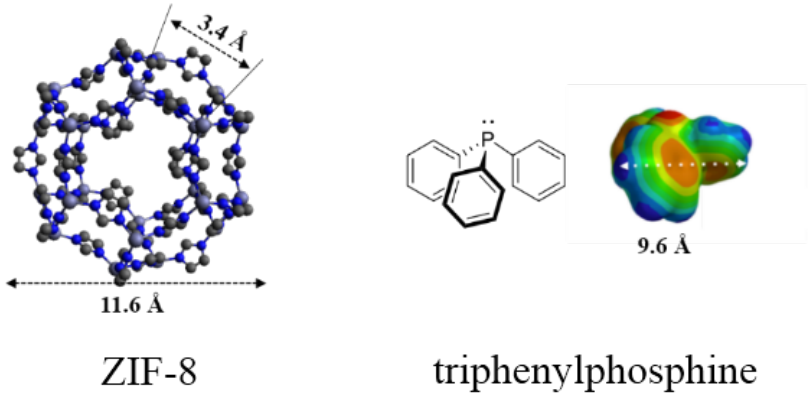

Figure 2-18. The molecular dimensions of the host ZIF-8 and the guest molecule triphenylphosphine.

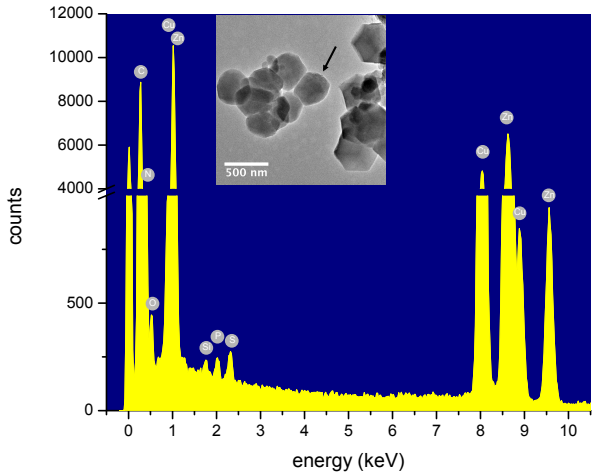

Figure 2-19. A representative energy dispersive X-ray spectrum of PPh_3@ZIF-8 loaded with initial [PPh_3] of 220 mM. Inset shows the TEM image of the area used for analysis, with the focused particle indicated by an arrow. The 10 % pore loading of PPh_3 was estimated by multiplying the P/Zn atomic ratio of 0.016 by 6 (the number of unique Zn atoms per sodalite cage of ZIF-8).

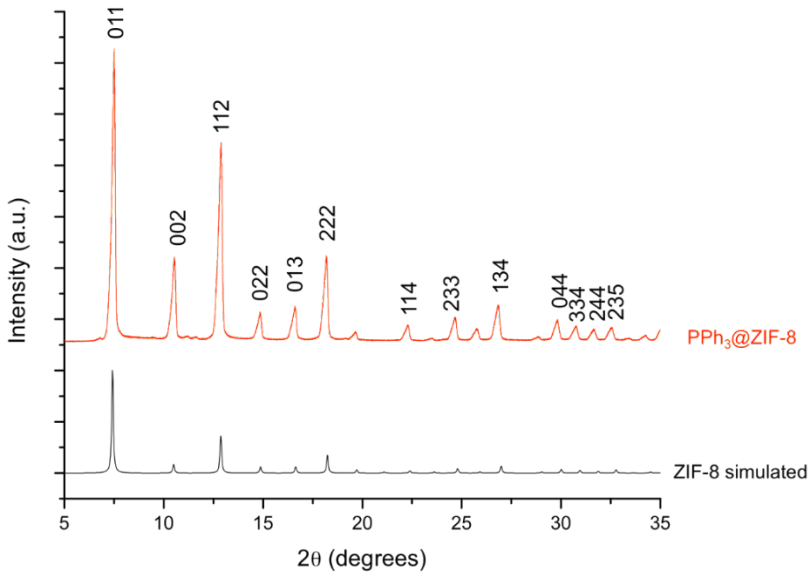

Figure 2-20. Powder X-ray diffraction (PXRD) patterns of PPh_3@ZIF-8 (top, red) and ZIF-8 simulated from the crystal structure (bottom, black) for reference. The loading was carried out with 220 mM PPh_3 in *n*-butanol for 7 days at 100 °C.

To demonstrate that the PPh_3 was mainly encapsulated within the pores of ZIF-8 and not on its surface, N_2 adsorption data were collected at 77 K on the two loadings of PPh_3@ZIF-8 and the commercial source of ZIF-8 (Figure 2-21a). A high resolution of points in the micropore adsorption region was depicted in Figure 2-20b. Saturation of the micropore volume with N_2 occurred for the reference ZIF-8 material at 485 cm^3/g, and the BET surface area was calculated to be 1554 m^2/g using a P/P_o range of 5×10^{-4} to 5×10^{-3} (before gating) or 1885 m^2/g with a range of 5×10^{-4} to 10^{-2} (after gating). These surface areas are in agreement with ZIF-8 values from the literature.[14] For the PPh_3@ZIF-8 samples, micropore saturation occurred at 459 cm^3/g for the sample exchanged with 165 mM PPh_3 and at 405 cm^3/g for that with 220 mM PPh_3, which is 5 % and 16 % lower compared to ZIF-8. This decrease in the micropore adsorption capacity was in excess of the decrease anticipated from the weight gain upon loading (only 2 %) and was consistent

with guests occupying some pores of the MOF. It was estimated from the data that approximately one in every 10 pores in ZIF-8 was occupied by a triphenylphosphine ligand. Such loadings were only possible by the linker exchange process that facilitates incorporation of the large ligand guest.

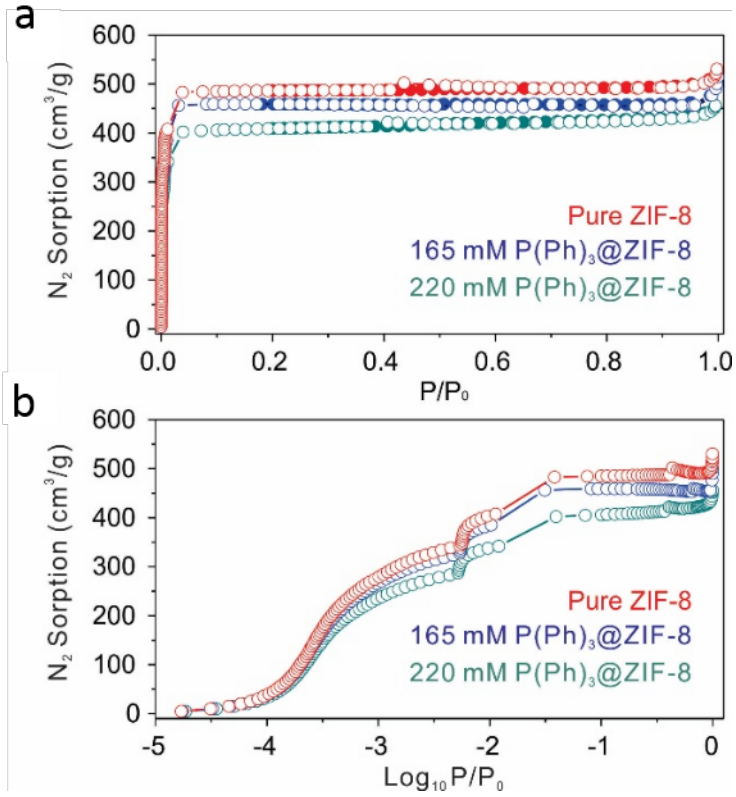

Figure 2-21. (a) N_2 absorption (filled symbols) and desorption (open symbols) isotherms of ZIF-8 (red), 165 mM triphenylphosphine@ZIF-8 (blue) and 220 mM triphenylphosphine@ZIF-8 (green). (b) Log_{10} scale of P/P_0 to show the detailed N_2 sorption under low pressure.

The metalation of the encapsulated triphenylphospine in PPh_3@ZIF-8 was done by treating a suspension of PPh_3@ZIF-8 with rhodium(III) trichloride in ethanol under reflux for one hour. Importantly, independent measurements revealed that these reaction conditions resulted in only a minimal amount of 2-methyl imidazole linker exchange. TEM

images of the rhodium loaded PPh_3@ZIF-8 (henceforth referred to as [Rh,PPh_3]@ZIF-8) revealed no evidence for rhodium nanoparticle formation, indicating that the rhodium is highly dispersed. The conditions for the metalation reaction were patterned after the synthesis of Wilkinson's catalyst (i.e. $(PPh_3)_3RhCl$), which results in the reduction of rhodium(III) trichloride to rhodium(I).[15] As indirect evidence that a similar reduction occurred in our reactions, the elemental composition of [Rh,PPh_3]@ZIF-8 analyzed by EDX revealed a Rh:Cl of 1:0.8, which was more consistent with rhodium(I) rather than rhodium(III) species. Interestingly, the Rh:P ratio was close to 1:1, which suggested a speciation that was different from Wilkinson's catalyst where a Rh:P of 1:3 was expected. At this point in our investigations, the source of this discrepancy is uncertain, but it may be due to the inaccessibility of multiple PPh_3 ligands to coordinate to rhodium in the ZIF-8 pores. Importantly, a similar procedure was carried out by treating ZIF-8 (without PPh_3) with rhodium(III) trichloride in ethanol under reflux. Elemental analysis of the resulting Rh@ZIF-8 from the ICP-OES of H_2SO_4 digested sample revealed a Rh:Cl that was close to 1:3, which suggested the presence of a rhodium(III) species. This result also suggested that PPh_3 interacted with rhodium in [Rh,PPh_3]@ZIF-8; otherwise, the reduction of rhodium(III) would not have occurred.

The hydroformylation of various alkene substrates using [Rh,PPh_3]@ZIF-8 was next carried out (Figure 2-22). Whereas Wilkinson's catalyst and [Rh,PPh_3]@ZIF-8 demonstrated catalytic activity for the hydroformylation of 1-octene (Conversions: 98%, 68%), $RhCl_3$@ZIF-8 and $RhCl_3$ showed low catalytic activity (Conversions: 31%, 1%). These results provided a second piece of evidence that rhodium in [Rh,PPh_3]@ZIF-8 was

in the rhodium(I) oxidation state, which was a more active oxidation state for hydroformylation than was rhodium(III).[16]

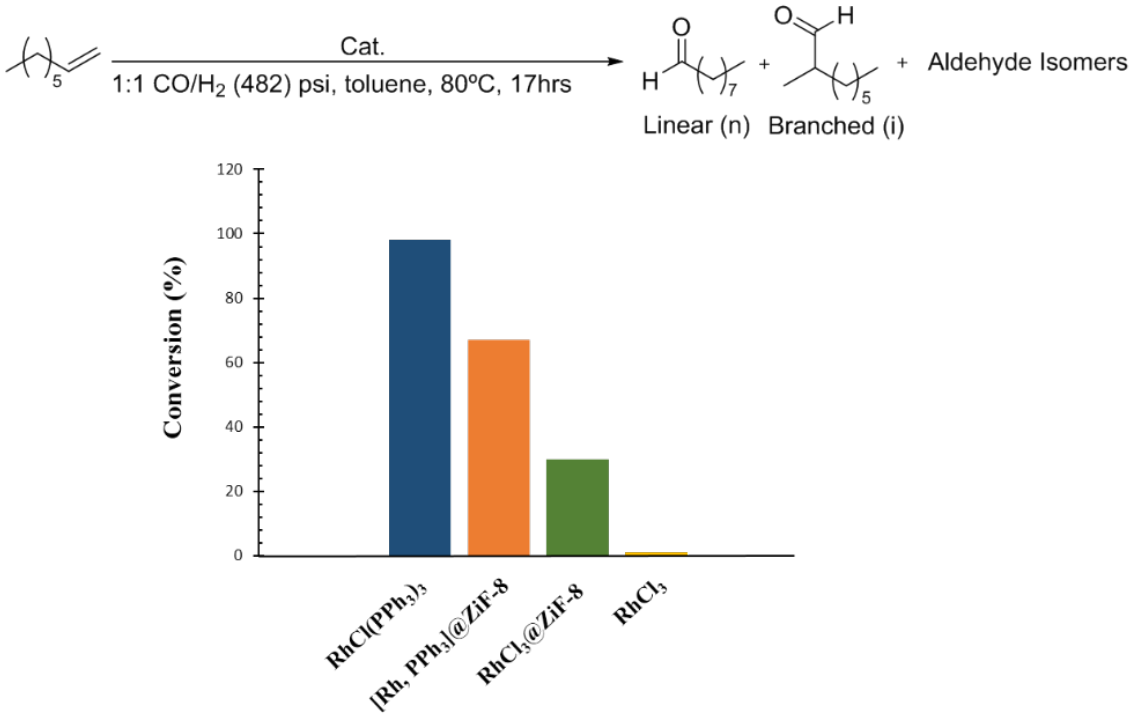

Figure 2-22. Hydroformylation of 1-octene by Wilkinson catalyst ($RhCl(PPh_3)_3$), [Rh,PPh_3]@ZiF-8, $RhCl_3$@ZIF-8 and $RhCl_3$.

For all of the olefins evaluated, [Rh,PPh_3]@ZIF-8 led to lower catalytic turnover compared to Wilkinson's catalyst (Figure 2-23). However, in sharp contrast to Wilkinson's catalyst, [Rh, PPh_3]@ZIF-8 demonstrated a significant dependence on the size and shape of the olefin substrate. Larger olefins resulted in lower conversions compared to smaller olefins. For example, while 1-octene demonstrated nearly 68% conversion after 17 h, 1-dodecene showed only 7%. Moreover, the branched vinylcyclohexane, which is too large to fit through the aperture of ZIF-8, demonstrated significantly retarded reaction rates

compared to the nearly isomeric 1-octene substrate. In addition to the size and shape dependence of the reaction rate, the selectivities for hydroformylation were also very different for [Rh, PPh_3]@ZIF-8 compared to Wilkinson's catalyst. The linear:branched ratios observed for isomeric aldehydes were higher for [Rh, PPh_3]@ZIF-8 (~3:1 for all linear alkenes) than for Wilkinson's catalyst (~1:1 for all linear alkenes), likely due to the effects of cage confinement on the formation of the intermediate.

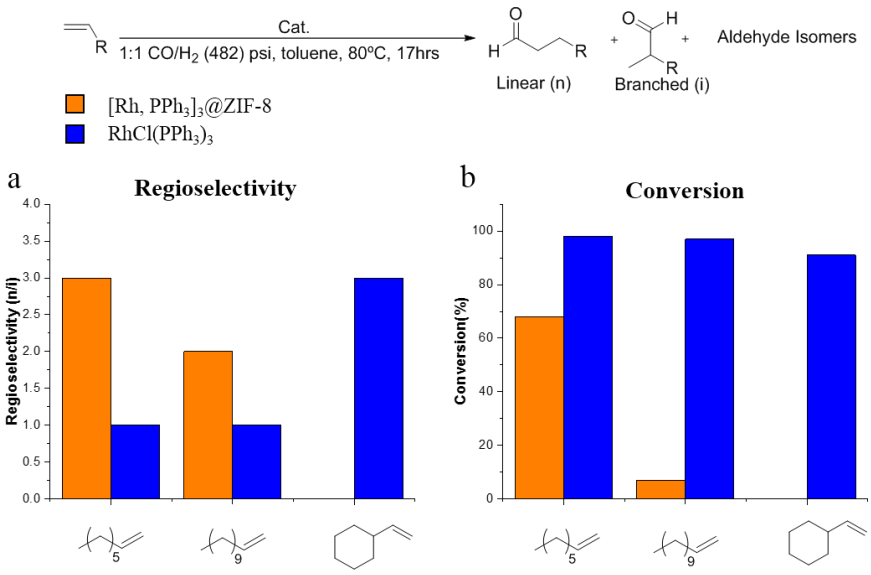

Figure 2-23. Hydroformylation of 1-octene, 1-dodecene, and vinylcyclohexane by using [Rh, PPh_3]@ZIF-8 and $RhCl(PPh_3)_3$.

The dramatic size dependence that [Rh, PPh_3]@ZIF-8 demonstrated, coupled with the difference in selectivity observed for [Rh, PPh_3]@ZIF-8 compared to Wilkinson's catalyst, clearly indicated that [Rh, PPh_3]@ZIF-8 contained a catalytically active species that was sequestered in the metal-organic framework.

2.6 Summary

A method has been developed for the postsynthetic encapsulation of large guests (R6G, PPh_3) with molecular diameters that exceed the framework aperture size in ZIF-8 nanocrystals beyond what could be explained by framework flexibility. The approach capitalizes on the existence of linker exchange reactions, which our kinetic studies show proceed by a competition between associative and dissociative exchange mechanisms. Maximum guest encapsulation was observed under conditions where the dissociative mechanism predominates because the dissociation of at least one aperture-defining 2-methylimidazole linker facilitates the formation of a short-lived "open" state in the pore with an expanded pore aperture size. Compared to other encapsulation strategies, this approach does not require any specific electrostatic interaction between the guest and the MOF host, which may significantly expand the scope of molecular guests and MOF hosts suitable for forming host-guest composites. In addition to the impact that these findings have on the ability to incorporate large guests in MOFs, important insight into the mechanism for linker exchange processes in MOFs was garnered. Such processes have already been exploited for the synthesis of novel MOF architectures,[5] useful catalyst species,[7d] and sophisticated nanocomposite materials.[7f]

Furthermore, a hydroformylation catalyst analog has been synthesized by combining the encapsulated triphenylphospine in PPh_3@ZIF-8 with rhodium(III) trichloride, and the resulted composite [Rh, PPh_3]@ZIF-8 shows higher linear to branch selectivity and similar activity compared to its homogeneous analog. Although distinct catalytic performance has been shown for [Rh, PPh_3]@ZIF-8, no exclusive evidence has shown the interactions between the rhodium and triphenylphospine.

Future investigations will look at the application of these findings to other classes of MOFs such as UiO-66, as well as the utilization of the new encapsulation methodology to expand the library of current catalytic systems that takes advantage of the size-selective capabilities of MOFs. After the exploration of aperture-opening encapsulation as a result of linker exchange, and the initial attempt in constructing catalytic host-guest composite, Chapter 3 will discuss in length the first successful example of the construction of host-guest hybrid catalytic system for energy conversions by using this aperture-opening encapsulation method. The following Chapters 4 and 5 will expand the scope of the host-guest system, and investigate the importance of mass transport in catalysis as well as the interactions between the host and guest to develop better biological analogs in the future.

2.7 Experimental Section

General considerations Unless otherwise stated, all the reactions were carried out in the air without taking any precaution to protect reactions from oxygen or moisture. Zinc nitrate hexahydrate (Aldrich, 99%), 2-methylimidazole (Aldrich, 99%), imidazole (Alfa Aesar, 99%), Basolite Z1200 (ZIF-8, Aldrich, produced by BASF), *n*-butanol (Alfa Aesar, ≥99.4%), N,N′-dimethylformamide (Alfa Aesar, ≥99.8%), Rhodamine 6G (Acros, dye content ~95%), triphenylphosphine (Aldrich), sodium hydroxide (VWR), polyvinylpyrrolidone (PVP, Mw~29,000, Aldrich), deuterium oxide (Aldrich, 99.9 atom % D), and sulfuric acid-d_2 solution (96-98 wt. % in D_2O, 99.5 atom % D) were purchased from the indicated sources and used without further purification.

Characterization Transmission electron microscope (TEM) images were obtained on JEOL JEM2010F operated at 200 kV. The powder x-ray diffraction patterns (PXRD) were collected on a Bruker AXS diffractometer with Cu Kα radiation (λ= 1.5418 Å). ^{1}H

NMR spectra obtained for the kinetic experiments were recorded on a Varian (Agilent) (600 MHz) spectrometer. The line listing for the NMR spectra are reported as chemical shift in ppm. The nitrogen gas adsorption-desorption was carried out on Micromeritics ASAP 2020 provided by the University of Massachusetts Boston. Visible light absorption spectra were measured on a Thermo Scientific NanoDrop 2000c.

Dye loading via linker exchange Variable amounts (9.3 mg/0.02 mmol, 29.2 mg/0.06 mmol, 73.9 mg/0.15 mmol, and 292.4 mg/0.61 mmol) of Rhodamine 6G (R6G) were placed in a 20 mL glass scintillation vial. 2-methylimidazole (Hmim) (181 mg, 2.2 mmol) and activated ZIF-8 crystals (75 mg, 0.33 mmol $Zn(mim)_2$) were added to the vial with the guest molecules. Next, *n*-butanol or DMF (15 mL) was added to the vial, and the solids were suspended by sonication for 10 minutes. The vial was capped and placed in an isothermal oven at 100 °C for 7 days. The guest-loaded ZIF-8 was collected by centrifugation at 5000 rpm for 10 minutes. The solid precipitate was triturated by decanting the methanol supernatant then re-suspended into fresh methanol (10 mL). The centrifugation and trituration steps were repeated at least 5 times until the supernatant was completely transparent. The residual solvent was removed from the isolated solids in a vacuum oven at 100 °C overnight. The mass recovery of the product was 92%.

PPh_3 loading via linker exchange Variable amounts of PPh_3 (866 mg/3.3 mmol and 649 mg/2.5 mmol) were placed in a 20 mL scintillation vial. 2-methylimidazole (181 mg, 2.2 mmol) and activated ZIF-8 crystals (75 mg, 0.33 mmol $Zn(mim)_2$) were added to the vial with the guest molecules. Next, *n*-butanol (15 mL) that had been sparged with Ar gas for 30 min to remove dissolved O_2 was added to the vial. The vial was capped and the solids were suspended by sonication for 10 minutes. The vial was placed in an isothermal

oven at 100 °C for 7 days. The guest-loaded ZIF-8 was collected by centrifugation at 5000 rpm for 10 minutes. The solid precipitate was triturated by decanting the methanol supernatant then re-suspended into fresh methanol (10 mL). The centrifugation and trituration steps were repeated at least 5 times. The residual solvent was removed from the isolated solids in a vacuum oven at 100 °C overnight. The mass recovery of the product was 92%.

The effect of exogenous linker concentration R6G (73.9 mg, 0.15 mmol) and activated ZIF-8 crystals (75 mg, 0.33 mmol $Zn(mim)_2$) were placed in a 20 mL scintillation vial. Variable amounts (0 mg, 60.3 mg/0.73 mmol, 120.6 mg/1.47 mmol, 181.0 mg/2.21 mmol, and 482.4 mg/5.88 mmol) of 2-methylimidazole were added to the vial with the guest and ZIF-8 mixture. Next, *n*-butanol (15 mL) was added to the vial, and the solids were suspended by sonication for 10 minutes. The vial was capped and placed in an isothermal oven at 100 °C for 7 days. The guest-loaded ZIF-8 was collected by centrifugation at 5000 rpm for 10 minutes. The solid precipitate was triturated by decanting the methanol supernatant then re-suspended into fresh methanol (10 mL). The centrifugation and trituration steps were repeated at least 5 times until the supernatant was completely transparent. The residual solvent was removed from the isolated solids in a vacuum oven at 100 °C overnight.

Synthesis of micron-sized ZIF-8 The synthesis of micron-sized ZIF-8 followed a published procedure.[17] A 25 mM solution of $Zn(NO_3)_2 \cdot 6H_2O$ in methanol (0.125 mmol, 5 mL) was combined with a 25 mM solution of 2-methylimidazole (0.125 mmol, 5 mL) in a 20 mL scintillation vial. The reaction was carried out at room temperature for 24 hours without stirring. The product was collected by centrifugation at 5000 rpm for 10 minutes.

The solid precipitate was triturated by decanting the methanol supernatant then re-suspended with fresh methanol (10 mL). The centrifuging and trituration steps were repeated 3 times. The residual solvent was removed from the isolated solids in a vacuum oven at 100 °C overnight. The yield of ZIF-8 was 8.4%.

Synthesis of nano-sized ZIF-8 The synthesis of nano-sized ZIF-8 is based on a previous procedure with some modifications.[18] $Zn(NO_3)_2 \cdot 6H_2O$ (150 mg, 0.504 mmol) and 2-methylimidazole (330 mg, 4.02 mmol) were weighed and transferred to a 30 mL glass vessel and 20 mL scintillation vial, respectively. The solids were dissolved in methanol (7.15 mL each). The glass jar was then equipped with a magnetic stir bar, and placed on a stir plate. Next, under vigorous stirring, the 2-methylimidazole solution was poured into the jar and the mixture was stirred at room temperature for 6 hours. The product was collected by centrifugation at 7000 rpm for 10 minutes. The solid precipitate was triturated by decanting the methanol supernatant then re-suspended with fresh methanol (10 mL). The centrifuging and trituration steps were repeated 3 times. The residual solvent was removed from the isolated solids in a vacuum oven at 100 °C overnight. The yield of ZIF-8 was 83%.

Visible light absorption spectroscopy Dried R6G@ZIF-8 (10 mg) was digested in a 1 wt% hydrochloric acid/methanol solution (2 mL). After stirring for 1 minute, the resulting solution was transferred to a glass cuvette to measure the visible light absorption spectrum at 530 nm on a Thermo Scientific NanoDrop 2000c. The amount of R6G loading was determined with a calibration obtained by monitoring the absorbance of light at 530 nm at different R6G concentration (extinction coefficient= 0.0934 $\mu M^{-1}cm^{-1}$ at 530 nm).

PVP washing Dried R6G@ZIF-8 (15 mg) was suspended in a 14 wt. %

PVP/methanol solution (10 mL) by sonication for 10 minutes. The solid precipitate was collected by trituration after centrifugation at 5000 rpm for 10 minutes. The isolated solid was then re-suspended with fresh 14 wt. % PVP/methanol (10 mL), and the centrifugation and trituration steps were repeated at least 5 times until the R6G content was constant, as determined by UV-Vis absorption spectroscopy. The PVP-washed product was then re-suspended with 10 mL methanol to remove any excess PVP, and the final product was collected by centrifugation at 5000 rpm for 10 minutes followed by decanting of the supernatant. The solid was then dried overnight in vacuum oven at 100 °C to remove any residual solvent. The mass recovery was 10 mg (66%).

Molecular size calculations The molecular sizes of R6G and triphenylphosphine were estimated by using the Spartan 10 software package. Hartree-Fock method with the basis set 3-21G was used to minimize structures. The greatest interatomic distances for each molecule are given as the effective molecular sizes in Figure 2-2, 2-22.

Linker exchange kinetics The kinetics of exchange of $Zn(mim)_2$ (ZIF-8) with exogenous imidazole (Him) to yield $Zn(mim)_{2-x}(im)_x$ (SALEM-2) were followed using a modified procedure based on literature precedence.[9] Due to the heterogeneous nature of the exchange reaction, accurate sampling could not be guaranteed, and thus, for the kinetics experiment, each point shown in Figure 2-10 is the result of independent measurements carried out at different reaction times by monitoring the amount of linker incorporated in the solid product. Generally, each reaction was repeated three times, the average of which is used for the kinetic fits.

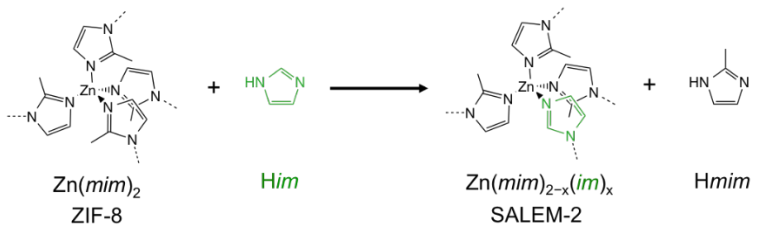

Dried ZIF-8 (5.0 mg, 0.022 mmol $Zn(mim)_2$) was placed in a 3 mL glass serum vial. Solids were suspended by sonication in an appropriate volume of *n*-butanol (tabulated below) before the reaction was initiated with exogenous linker. A 588 mM solution of imidazole in *n*-butanol was added in an appropriate volume (see below), and vials were immediately sealed with PTFE-lined aluminum crimp caps. Immediately, the vials were shaken manually for 5 s, and placed into the aluminum heating blocks of a Labmate synthesizer thermostated at 70 °C. The reactions were incubated at 70 ºC with 450 rpm shaking for a predetermined amount of time.

Data point	*1*	*2*	*3*	*4*
im/mim (mol/mol)	5	10	20	30
Vol. n-butanol (mL)	2.625	2.250	1.500	0.750
Vol. 588 mM Him (mL)	0.375	0.750	1.500	2.250

At the end of the allocated time, the vials were removed and immediately immersed in a water bath held at 0 ºC. Suspended solids were transferred quickly into 3 mL of methanol chilled at 0 °C in a 15 mL centrifuge tube and centrifuged at 3300 rpm for 5 min. The solid precipitate was triturated by decanting the supernatant, and the product was re-suspended in fresh methanol (6 mL). The centrifugation and trituration was repeated 3 times with 6 mL of methanol each time. The isolated solids were transferred to pre-weighed

glass vials and the residual solvent was removed in a vacuum oven at 100 °C overnight. Dried samples were weighed and then digested in a solution of 0.900 mL deuterium oxide and 0.100 mL 98% d_2-sulfuric acid in D_2O along with tetramethylammonium bromide (0.7 mg) that was used as an internal standard for analysis by ^{1}H-NMR spectroscopy.

The spin-lattice relaxation times (T_1) of each proton in solution were determined by the inversion recovery method and are detailed in the following table. In light of the measured relaxation times, ^{1}H-NMR spectra were acquired using an acquisition time (at) of 18 s and an interpulse delay (d1) of 54 s, in order to make (at + d1) ~ 5 × the longest T_1. A pulse angle of 90 ° was used and 16 transients were taken per acquisition.

proton (in red)	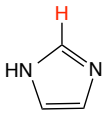	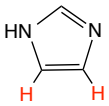	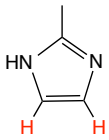	H_2O	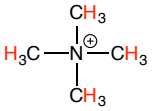	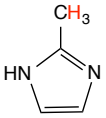
δ (ppm)	7.85	6.66	6.45	4.94	2.35	1.79
T_1 (s)	13.74 ± 0.28	12.06 ± 0.21	9.72 ± 0.26	3.01 ± 0.11	5.65 ± 0.12	4.44 ± 0.32

The quantity of imidazole and 2-methylimidazole in solution were determined using the formulae:

A_P = area determined by integration of peak (P), as defined in Figure S9

$$\left(A_A \times \frac{[TMA^+]}{A_D} \times \frac{12 \text{ protons}}{1 \text{ protons}}\right) + \left(A_B \times \frac{[TMA^+]}{A_D} \times \frac{12 \text{ protons}}{2 \text{ protons}}\right) = 2[im]$$

$$\left(A_C \times \frac{[TMA^+]}{A_D} \times \frac{12 \text{ protons}}{2 \text{ protons}}\right) + \left(A_E \times \frac{[TMA^+]}{A_D} \times \frac{12 \text{ protons}}{3 \text{ protons}}\right) = 2[mim]$$

$$\frac{[mim]}{[im] + [mim]} = conversion$$

Synthesis of 85, 125, 240, and 400 nm ZIF-8 The synthesis procedure was adapted from previous reports.[19] A 1.32 M solution of 2-MeImH was prepared by adding 10.837 g 2-MeImH to a volumetric flask and diluting to 0.100 L with deionized water. A 0.01 M cetyltrimethylammonium bromide (CTAB) solution was prepared by adding 0.3645 g of CTAB to a volumetric flask and diluting to 0.100 L with deionized water (dissolves slowly). A 0.024 M $Zn(NO_3)_2$ solution was prepared by adding 0.7140 g $Zn(NO_3)_2 \cdot 6H_2O$ to a volumetric flask and diluting to 0.100 L with deionized water. Reactions were carried out in stainless steel autoclaves (Parr) with 45 mL capacity PTFE liners. In a PTFE liner, 17.5 mL of the 1.32 M 2-MeIm solution was combined with variable amounts of the 0.01 M CTAB solution: 1.260 mL (85 nm), 1.008 mL (125 nm), 0.504 mL (240 nm), and 0.252 mL (400 nm). The solutions were then mixed by stirring at 500 rpm for 5 min followed by the addition of 17.5 mL of the 0.024 M $Zn(NO_3)_2$ solution. Stirring was continued for 5 min, after which the stirbar was removed and the PTFE liner was transferred into the stainless steel autoclave. All of the solutions became cloudy within 2 min after Zn(II) addition, with higher concentrations of CTAB resulting in delayed precipitation. The autoclaves were sealed and left in a 120 °C oven for 6 h. After cooling, the ZIF-8 crystals

and mother liquor were divided into two 45 mL centrifuge tubes to which was added 20 mL of methanol each. The crystals were then collected by centrifugation at 14k rpm for either 30 min (85 and 125 nm) or 15 min (240 and 400 nm). The supernatants were decanted and the solids were consolidated from two tubes into one tube per reaction with 20 mL of fresh methanol. This first wash was then collected by centrifugation at either 14k rpm for 20 min (85 and 125 nm) or 10k rpm for 15 min (240 and 400 nm) and the supernatants were decanted. The washing procedure was then repeated for a second wash with 20 mL fresh methanol. The resulting solids were left to soak overnight in 20 mL fresh methanol in a third wash to allow trapped species such as unreacted 2-MeImH to diffuse out of the microporous crystals. The next day, the particles were collected as before and the supernatants decanted. The products were dried at 70 °C in air. Yields were around 90 % for all four sizes, with representative product weights of 83.7 mg (85 nm), 86.5 mg (125 nm), 83.2 mg (240 nm), and 84.9 mg (400 nm).

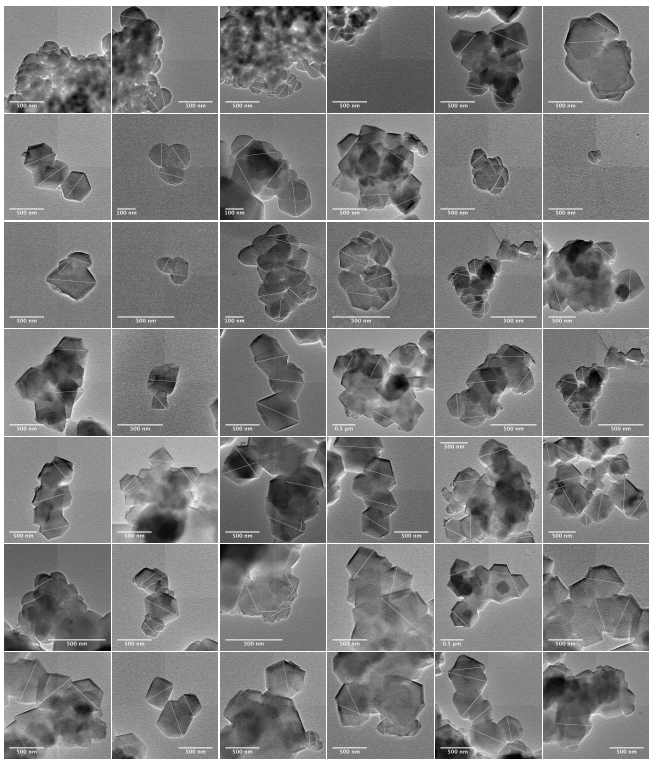

Figure 2-24. TEM images used to calculate the grain size distribution of the commercial sample, Basolite Z1200, with a D50 of 265 nm. White lines are the grain diameter, *d*, measurements.

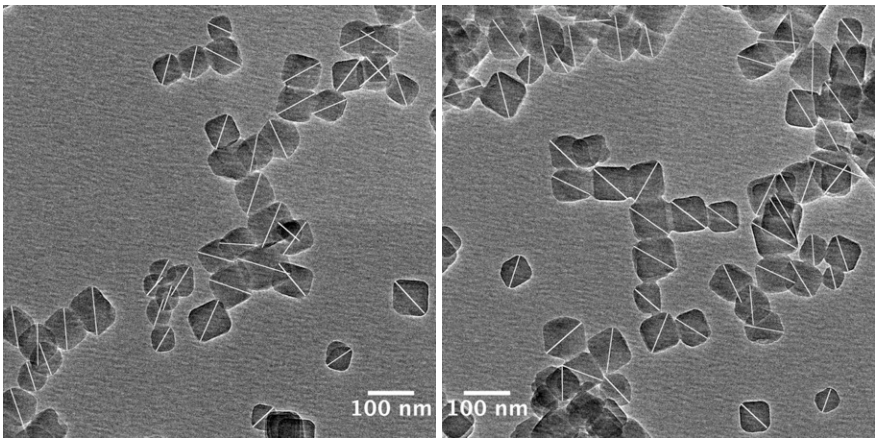

Figure 2-25. TEM images used to calculate the grain size distribution of the sample "M" with a D50 of 85 nm. White lines are the grain diameter measurements. For this sample grain size, *d*, equals particle size.

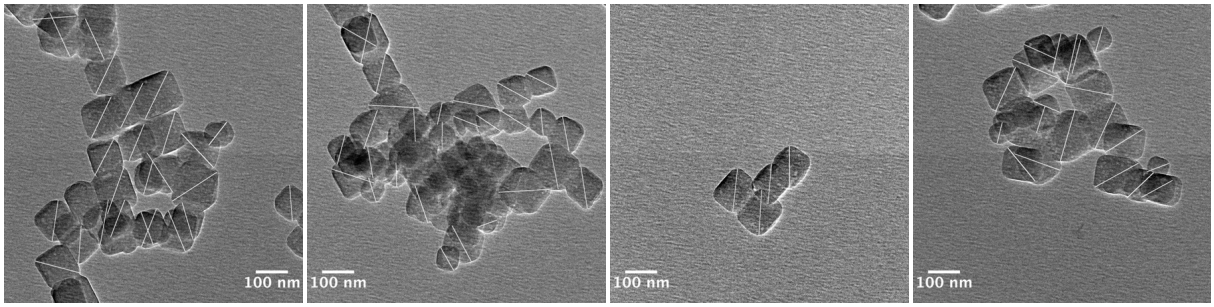

Figure 2-26. TEM images used to calculate the grain size distribution of the sample "L" with a D50 of 125 nm. White lines are the grain diameter measurements. For this sample grain size, *d*, equals particle size.

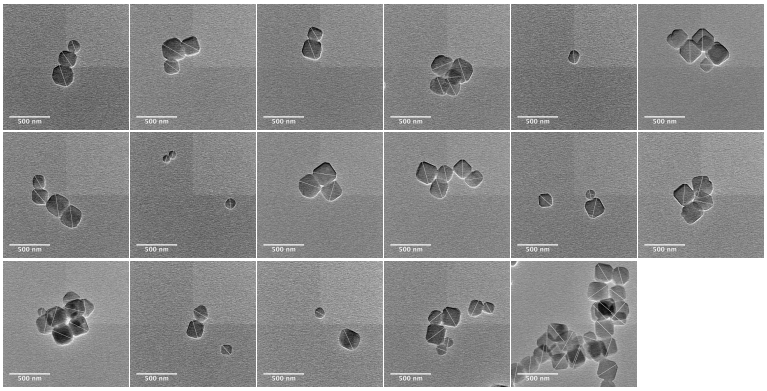

Figure 2-27. TEM images used to calculate the grain size distribution of the sample "XL" with a D50 of 239 nm. White lines are the grain diameter measurements. For this sample grain size, *d*, equals particle size.

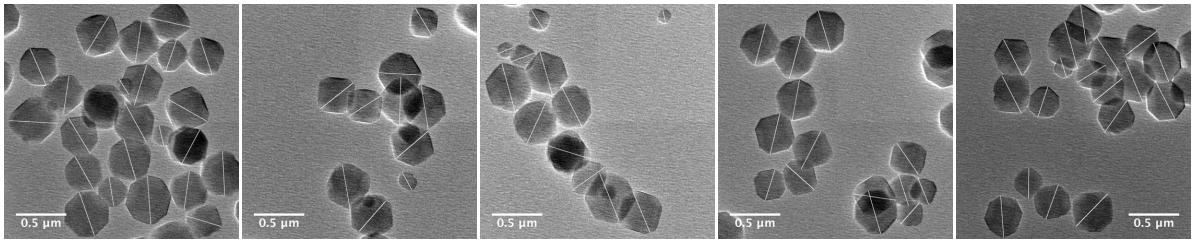

Figure 2-28. TEM images used to calculate the grain size distribution of the sample "XXL" with a D50 of 404 nm. White lines are the grain diameter measurements. For this sample grain size, *d*, equals particle size.

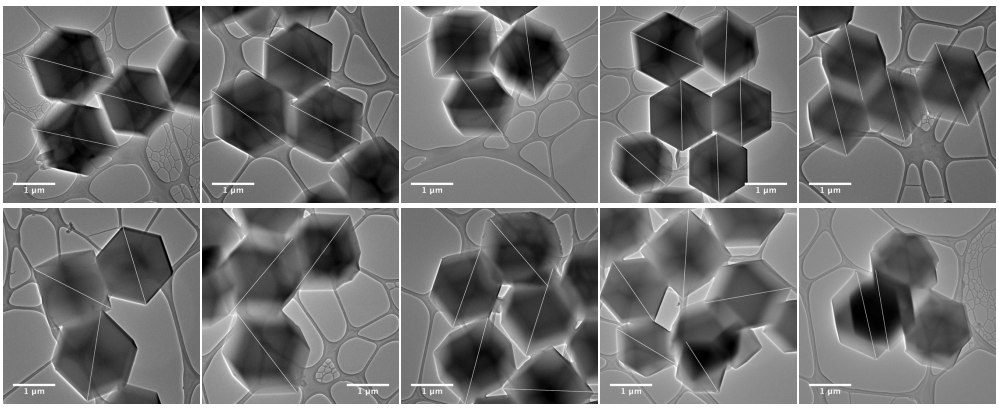

Figure 2-29. TEM images used to calculate the grain size distribution of the sample with a D50 of 1.96 μm. White lines are the grain diameter measurements. For this sample grain size, *d*, equals particle size.

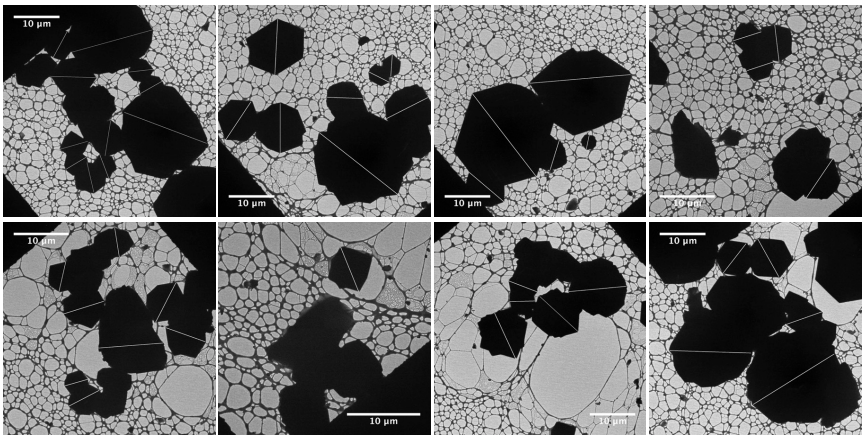

Figure 2-30. TEM images used to calculate the grain size distribution of the sample with a D50 of 7.76 μm. White lines are the grain diameter measurements.

Preparation of [Rh, PPh_3]@ZIF-8 To a 20 mL scintillation was added 150 mg of PPh3@ZIF-8 (containing 2 wt% triphenylphosphine) and it was suspended in ethyl alcohol (4 mL). $RhCl_3$ (0.79 mg, 4 mol, 0.33 eq.) was added to this suspension, the vial was capped and heated to 90 °C for 45 minutes. The vial was gently agitated throughout the course of the reaction. The solution was cooled to room temperature and the solid was isolated by

filtration and washed with cold ethanol (3x3 mL). Afterwards, the solid was dried in vacuum affording a yellowish solid in a quantitative yield.

Preparation of $Rh(PPh_3)_2(CO)Cl$[16a] All the glassware were dried in oven overnight before being transferred to the glove box. The following procedure was carried out in a glove box under N_2 atmosphere. $[Rh(CO)_2Cl]_2$ (15mg, 0.038 mmol) dissolved in dry benzene (2 mL) was treated slowly dropwise with triphenylphosphine (20 mg, 0.076 mmol) in dry benzene (1 mL) with vigorous stirring. The triphenylphosphine was further rinsed out with dry benzene (0.5 mL) twice. The reaction was carried out for 2 hours in the glove box with stirring. After being taken out of the glove box, the reaction mixture was concentrated by removing the solvent. Addition of pentane (4 mL) gave the orange-yellow product. The solid was re-suspended by sonication and re-precipitate the solid after centrifugation at 4300rpm for 3 minutes. The isolated solid was then re-suspended with fresh pentane (4 mL), and the sonication, centrifugation and decanting steps were repeated three times. The final product was dried in vacuum and gave 75% yield. ^1H NMR (DMSO-d6, 500 MHz). δ 7.15 ppm (d, 12H), δ 7.44 ppm (t, 12 H), δ 7.47 ppm (t, 6 H). NMR matches literature reports.

General procedure for hydroformylation

General consideration Hydroformylation was performed in 50 Ml Parr reactor using 1:1 H_2/CO supplied by Airgas, Inc. Nuclear Magnetic Resonance (NMR) spectra were recorded at ambient temperature on spectrometers operating at 500 MHz, and gas chromatography (Shimadzu,GC-2014, 30 °C 5 mins, 15 °C/min up to 250 °C for 15 mins)

were also applied to analyze the products. Eight glass liners used as reaction container allows multiple reactions to run in parallel.

1-octene, 1-dodecene and vinylcyclohexane substrates were used for the hydroformylation of n-alkene over ZIF-8 encapsulated catalyst. The catalytic reactions were carried out in the following way. In the 20 mL glass ampules were added the reaction mixture containing the olefin substrate (1mmol, 1M) in toluene, and the catalyst. The olefin and the rhodium ratio was kept at 2000/1, for example, 1 mmol olefin, 16 mg [Rh, PPh_3]@MOF or 0.12 mg Wilkinson catalyst. One ampule containing toluene was included in the reactor to avoid cross-talk over the course of reaction. The Parr reactor was initially purged with syngas (1:1 H_2/CO) for 5 minutes followed by being pressurized up to 34 bar at room temperature. After the pressure was stabled for 10 minutes, the gas tank was closed and the reaction was heated to 80 °C. The reaction was stirred at 300 rpm at 80 °C for 17 hours. The reaction mixture was sonicated shortly and transferred in to a 20 ml dram vial. After centrifugation at 4300 rpm for 3 mins, the catalyst precipitated at the bottom of the vial. The remaining oil was analyzed by ^{1}H NMR and GC.

Reference

(1) (a)Horcajada, P.; Chalati, T.; Serre, C.; Gillet, B.; Sebrie, C.; Baati, T.; Eubank, J. F.; Heurtaux, D.; Clayette, P.; Kreuz, C.; Chang, J.-S.; Hwang, Y. K.; Marsaud, V.; Bories, P.-N.; Cynober, L.; Gil, S.; Ferey, G.; Couvreur, P.; Gref, R. *"Porous metal-organic-framework nanoscale carriers as a potential platform for drug delivery and imaging"* *Nat. Mater.* **2010**, *9*,172-176; (b)Rimoli, M. G.; Rabaioli, M. R.; Melisi, D.; Curcio, A.; Mondello, S.; Mirabelli, R.; Abignente, E. *"Synthetic zeolites as a new tool for drug delivery"* Journal of Biomedical Materials Research Part A **2008**, *87*,156-162.

(2) Alkordi, M. H.; Liu, Y.; Larsen, R. W.; Eubank, J. F.; Eddaoudi, M. *"Zeolite-like metal-organic frameworks as platforms for applications: on metalloporphyrin-based catalysts"* Journal of the American Chemical Society **2008**, *130*,12639-12642.

(3) (a)Li, B.; Zhang, Y.; Ma, D.; Ma, T.; Shi, Z.; Ma, S. *"Metal-Cation-Directed de Novo Assembly of a Functionalized Guest Molecule in the Nanospace of a Metal,ÄìOrganic Framework"* Journal of the American Chemical Society **2014**, *136*,1202-1205; (b)Zhuang, J.; Kuo, C.-H.; Chou, L.-Y.; Liu, D.-Y.; Weerapana, E.; Tsung, C.-K. *"Optimized Metal–Organic-Framework Nanospheres for Drug Delivery: Evaluation of Small-Molecule Encapsulation"* ACS Nano **2014**, *8*,2812-2815.

(4)Yin, Z.; Wan, S.; Yang, J.; Kurmoo, M.; Zeng, M.-H. *"Recent advances in post-synthetic modification of metal–organic frameworks: New types and tandem reactions"* Coordination Chemistry Reviews **2019**, *378*,500-506.

(5) Burnett, B. J.; Barron, P. M.; Hu, C.; Choe, W. *"Stepwise synthesis of metal-organic frameworks: replacement of structural organic linkers"* Journal of the American Chemical Society **2011**, *133*,9984-9990.

(6) (a)Karagiaridi, O.; Bury, W.; Sarjeant, A. A.; Stern, C. L.; Farha, O. K.; Hupp, J. T. *"Synthesis and characterization of isostructural cadmium zeolitic imidazolate frameworks via solvent-assisted linker exchange"* Chemical Science **2012**, *3*,3256-5259; (b)Kim, M.; Cahill, J. F.; Su, Y.; Prather, K. A.; Cohen, S. M. *"Postsynthetic ligand exchange as a route to functionalization of 'inert' metal-organic frameworks"* Chem. Sci. **2012**, *3*,126-135.

(7) (a)Karagiaridi, O.; Lalonde, M. B.; Bury, W.; Sarjeant, A. A.; Farha, O. K.; Hupp, J. T. *"Opening ZIF-8: a catalytically active zeolitic imidazolate framework of sodalite topology with unsubstituted linkers"* J. Am. Chem. Soc. **2012**, *134*,18790-18794; (b)Fei, H.; Cahill, J. F.; Prather, K. A.; Cohen, S. M. *"Tandem postsynthetic metal ion and ligand exchange in zeolitic imidazolate frameworks"* Inorganic Chemistry **2013**, *52*,4011-4015; (c)Kim, M.; Cahill, J. F.; Fei, H.; Prather, K. A.; Cohen, S. M. *"Postsynthetic ligand and cation exchange in robust metal-organic frameworks"* Journal of the American Chemical Society **2012**, *134*,18082-18086; (d)Pullen, S.; Fei, H.; Orthaber, A.; Cohen, S. M.; Ott, S. *"Enhanced photochemical hydrogen production by a molecular diiron catalyst incorporated into a metal-organic framework"* Journal of the American Chemical Society **2013**, *135*,16997-16700; (e)Deria, P.; Mondloch, J. E.; Tylianakis, E.; Ghosh, P.; Bury, W.; Snurr, R. Q.; Hupp, J. T.; Farha, O. K. *"Perfluoroalkane functionalization of NU-1000 via solvent-assisted ligand*

incorporation: synthesis and CO2 adsorption studies" Journal of the American Chemical Society **2013**, *135*,16801-16805; (f)Takaishi, S.; DeMarco, E. J.; Pellin, M. J.; Farha, O. K.; Hupp, J. T. *"Solvent-assisted linker exchange (SALE) and post-assembly metallation in porphyrinic metal-organic framework materials"* Chemical Science **2013**, *4*,1509-1513; (g)Bury, W.; Fairen-Jimenez, D.; Lalonde, M. B.; Snurr, R. Q.; Farha, O. K.; Hupp, J. T. *"Control over Catenation in Pillared Paddlewheel Metal–Organic Framework Materials via Solvent-Assisted Linker Exchange"* Chemistry of Materials **2013**, *25*,739-743.

(8) Lu, G.; Li, S.; Guo, Z.; Farha, O. K.; Hauser, B. G.; Qi, X.; Wang, Y.; Wang, X.; Han, S.; Liu, X.; DuChene, J. S.; Zhang, H.; Zhang, Q.; Chen, X.; Ma, J.; Loo, S. C. J.; Wei, W. D.; Yang, Y.; Hupp, J. T.; Huo, F. *"Imparting functionality to a metal–organic framework material by controlled nanoparticle encapsulation"* Nat. Chem. **2012**, *4*,310-315.

(9) Karagiaridi, O.; Lalonde, M. B.; Bury, W.; Sarjeant, A. A.; Farha, O. K.; Hupp, J. T. *"Opening ZIF-8: A Catalytically Active Zeolitic Imidazolate Framework of Sodalite Topology with Unsubstituted Linkers"* Journal of the American Chemical Society **2012**, *134*,18790-18795.

(10) Tan, J. C.; Bennett, T. D.; Cheetham, A. K. *"Chemical structure, network topology, and porosity effects on the mechanical properties of Zeolitic Imidazolate Frameworks"* Proceedings of the National Academy of Sciences **2010**, *107*,9938-9943.

(11) Butt, J. B. *"Mass transfer in heterogeneous catalysis" AIChE Journal* **1970**, *16*,509-514.

(12) In this context, we mean 10% past the y-intercept. The crystal surface tontains coordination environments that are not representative of the bulk, and this is reflected in the nonzero y-intercepts of conversion versus time plots

(13) Juan-Alcañiz, J.; Ramos-Fernandez, E. V.; Lafont, U.; Gascon, J.; Kapteijn, F. *"Building MOF bottles around phosphotungstic acid ships: One-pot synthesis of bi-functional polyoxometalate-MIL-101 catalysts"* Journal of Catalysis **2010**, *269*,229-235.

(14) Park, K. S.; Ni, Z.; Cote, A. P.; Choi, J. Y.; Huang, R. D.; Uribe-Romo, F. J.; Chae, H. K.; O'Keeffe, M.; Yaghi, O. M. *"Exceptional chemical and thermal stability of zeolitic imidazolate frameworks"* Proceedings of the National Academy of Sciences of the United States of America **2006**, *103*,10186-10192.

(15) Van Vu, T.; Kosslick, H.; Schulz, A.; Harloff, J.; Paetzold, E.; Schneider, M.; Radnik, J.; Steinfeldt, N.; Fulda, G.; Kragl, U. *"Selective hydroformylation of olefins over the rhodium supported large porous metal–organic framework MIL-10"* Applied Catalysis A: General **2013**, *468*,410-415.

(16) (a)In *Inorganic Syntheses*; (b)Dedieu, A. *Hydrogenation of olefins catalyzed by the chlorotris(triphenylphosphine)rhodium(I) complex. A theoretical study of the structural aspects* Inorganic Chemistry **1980**, *19*,375.

(17) Lu, G.; Li, S.; Guo, Z.; Farha, O. K.; Hauser, B. G.; Qi, X.; Wang, Y.; Wang, X.; Han, S.; Liu, X.; DuChene, J. S.; Zhang, H.; Zhang, Q.; Chen, X.; Ma, J.; Loo, S. C. J.; Wei,

W. D.; Yang, Y.; Hupp, J. T.; Huo, F. *"Imparting functionality to a metal–organic framework material by controlled nanoparticle encapsulation"* Nature Chemistry **2012**, *4*,310-315.

(18) Venna, S. R.; Jasinski, J. B.; Carreon, M. A. *"Structural Evolution of Zeolitic Imidazolate Framework-8"* Journal of the American Chemical Society **2010**, *132*,18030-18035.

(19) Pan, Y.; Heryadi, D.; Zhou, F.; Zhao, L.; Lestari, G.; Su, H.; Lai, Z. *"Tuning the crystal morphology and size of zeolitic imidazolate framework-8 in aqueous solution by surfactants"* CrystEngComm **2011**, *13*,6937-6941.

Chapter 3. Aperture-opening Encapsulation of a Transition Metal Catalyst in a Metal-organic Framework for CO_2 Hydrogenation

3.1 Strategies for constructing host-guest systems with a metal-organic framework

As discussed in the previous chapters, host-guest composites using MOFs as hosts have proven to be a versatile platform for a wide variety of applications including gas storage,[1] drug delivery,[2] chemical sensing,[3] and catalysis.[4]

Recently, we have developed a new approach to encapsulate guest molecules into MOFs that circumvents lengthy synthetic sequences and incompatible reaction conditions.[5] In this approach, molecular guests larger than the aperture size of a MOF host are encapsulated into the pores by taking advantage of aperture-opening events that occur as a result of dissociative linker substitution reactions (Scheme 3-1). In this work, we demonstrate that the solvent-dependent aperture-opening process exists even in a chemical/thermal robust MOF,[6] which led us to pursue an effective strategy for using MOFs to synthesize host-guest composites for chemical catalysis (Scheme 3-1).

Scheme 3-1

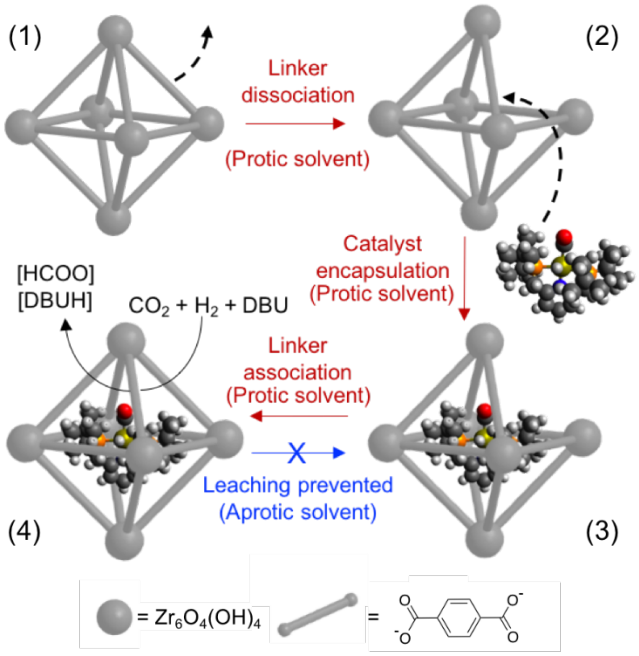

The strategy involves encapsulating catalysts and running catalytic reactions under different conditions. Solvents that favor dissociative linker exchange were used to promote the encapsulation of a molecular guest via aperture-opening events (e.g. (1) to (4), Scheme 1). Molecular catalyst leaching from the framework during catalysis is prevented by carrying out catalytic reactions in solvents where dissociative linker exchange is slow (e.g. (4) to (3), Scheme 3-1). Herein, implementation of this strategy is demonstrated successful with the encapsulation of a highly active homogeneous CO_2 hydrogenation catalyst[7] into the robust metal-organic framework, UiO-66 (shown as the octahedral cage in scheme 3-1).[8] The encapsulated catalyst exhibited properties that were a hybrid of homogeneous and heterogeneous catalysts, and evidence is provided that supports that the majority of the active catalyst was encapsulated inside of the MOF rather than on its surface.

3.2 Dye encapsulation in UiO-66 though aperture-opening encapsulation

The robust UiO-66 was anticipated to be compatible with a variety of reaction conditions. As a result, UiO-66 was selected as the host material to demonstrate this concept instead of the less robust zinc imidazolate-based MOF ZIF-8 was previously investigated in chapter 2. In order to verify that the aperture-opening events in UiO-66 can be used to encapsulate guests similarly to what have been observed in ZIF-8,[5] the fluorescent dye Rhodamine 6G (R6G) was used as a model guest molecule (see experimental section for details). Dye encapsulation carried out by Tom Rayder was observed when UiO-66 was suspended in protic polar solvents (Figure 3-1), and encapsulation of R6G was depressed when exogenous terephthalic acid was present (Figure 3-2). These results are similar to those obtained with ZIF-8 (See Chapter 2), suggesting that R6G encapsulation occurred as a consequence of aperture-opening events that result from linker dissociation which are more prominent at low concentrations of exogenous terephthalic acid.[10]

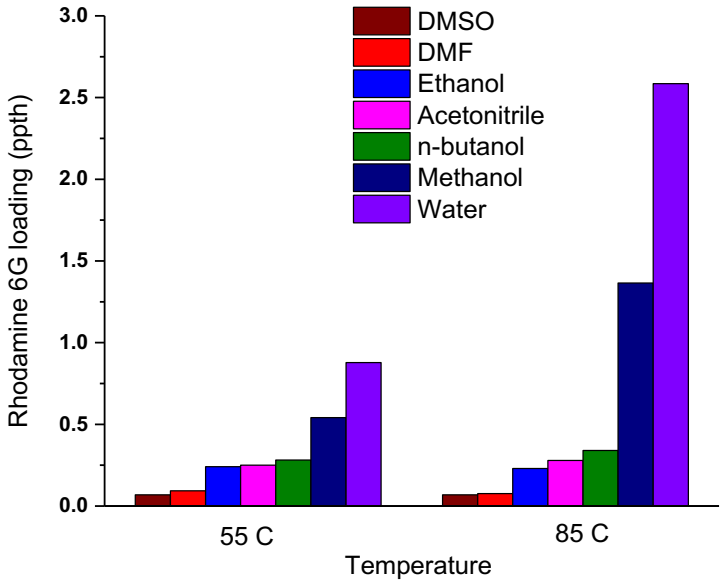

Figure 3-1. Rhodamine 6G encapsulated (parts per thousand) in UiO-66 at 55 ºC and 85 ºC in various solvents. Ppth represents parts per thousand.

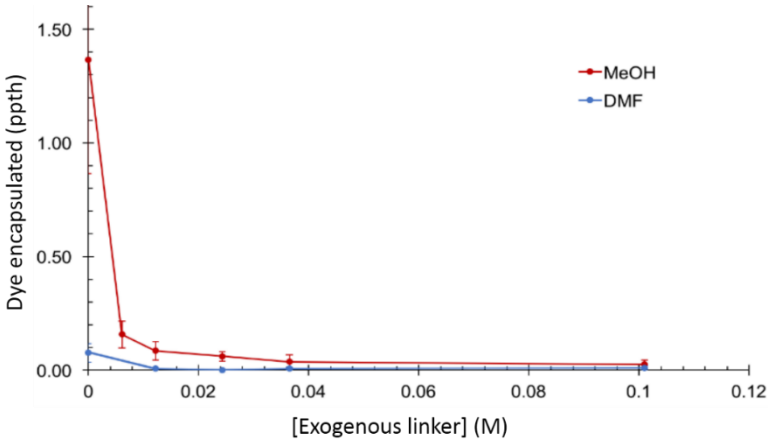

Figure 3-2. Effect of exogenous linker addition on Rhodamine 6G encapsulation at 85 ºC for five days in methanol and DMF. Ppth represents parts per thousand.

The appearance of new defects is a common concern in post treatment of MOF materials.[5] The surface area of UiO-66 obtained from nitrogen sorption before (947.6 m^2/g) and after aperture-opening events (948.8 m^2/g) indicated that no additional defects were generated after the encapsulation (Figure 3-3).[8b]

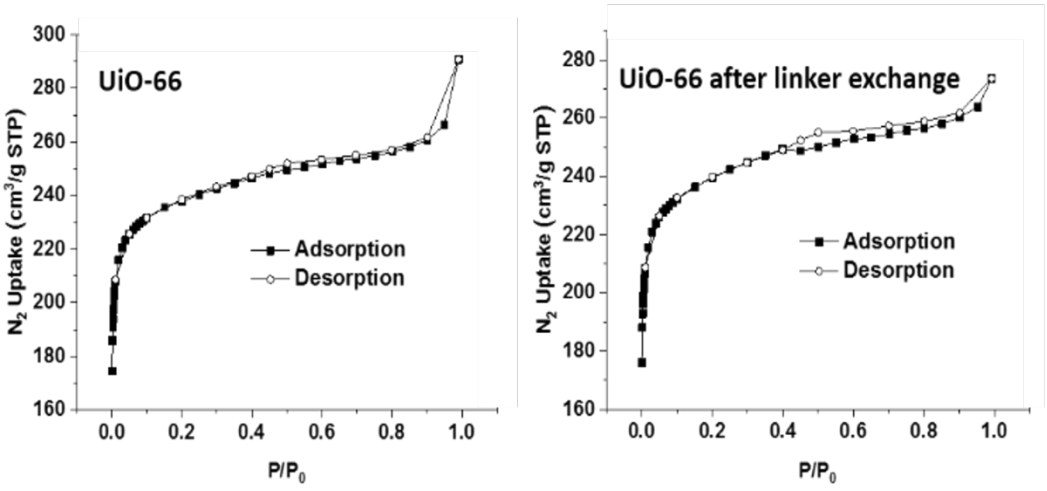

	Pristine UiO-66	UiO-66 after linker exchange
N_2 Uptake (cm^3 $_{STP}$/G)(P/P_0=0.8)	256.3	256.5
BET (R^2)	947.6	948.8

Figure 3-3. Nitrogen adsorption and desorption of UiO-66 before and after linker exchange.

Next, similar dye encapsulation experiments were used to identify the appropriate conditions required for encapsulation of a transition metal complex and to discern the orthogonal conditions needed to suppress leaching of the guest catalyst molecules during catalysis (Figure 3-4). The amount of encapsulated R6G was significantly higher than surface bond dye, and more encapsulation of R6G occurred at elevated temperature in polar protic solvents (Figure 3-4a, b). Similarly, in experiments that involved exposing R6G

encapsulated in UiO-66 to various solvents, dye leaching into solution was highly suppressed in aprotic solvents compared to protic solvents (Figure 3-4c).

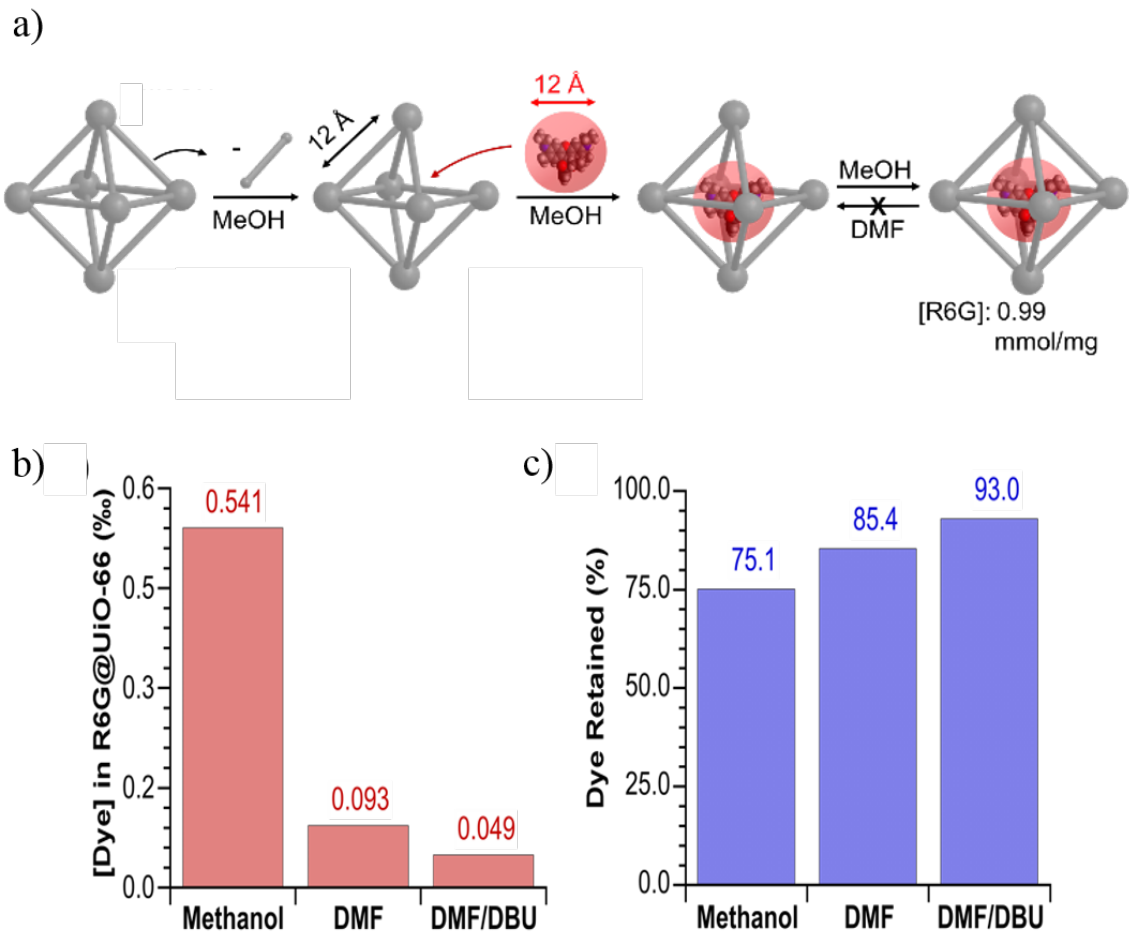

Figure 3-4. a) Encapsulation of R6G in UiO-66 in methanol at 55 ºC for 5 days; [Ru]@UiO-66 in DMF at 55 ºC for five days resulted in no change in [R6G]. b) Amount of dye encapsulated in MOF in neat solvent at 55 ºC for 5 days. c) percent of original encapsulated dye remaining in R6G@UiO-66 after exposure to solvents at 55 ºC for 2 days.

Due to the linker exchange reaction occurring at the solid-liquid interface, and due to the transient nature of the intermediate involved, direct observation of the proposed

aperture-opened intermediate (e.g., 2, Scheme 3-1) is difficult. Therefore, to further probe the mechanism for guest encapsulation, two additional experiments were carried out (Figure 3-5).

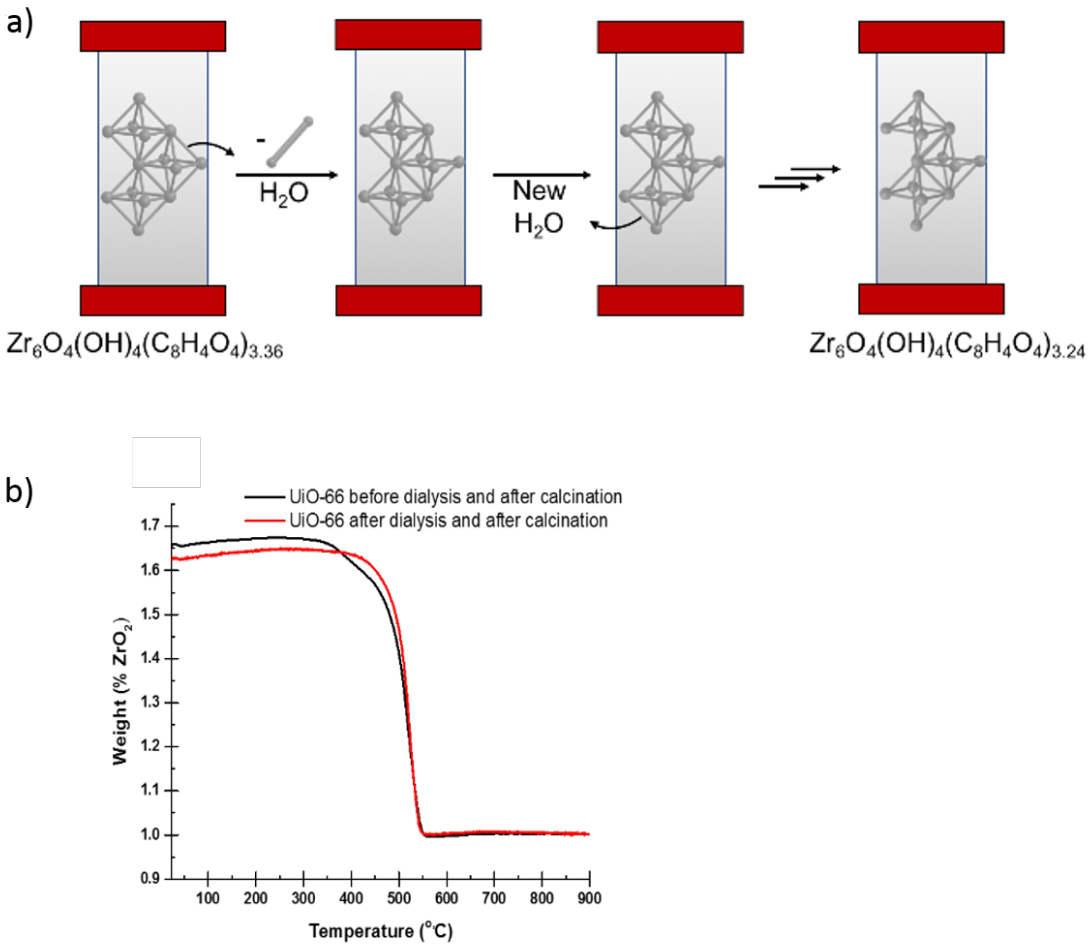

Figure 3-5. a) Dialysis experiment with UiO-66 in water at 55 ºC for 18 days; empirical formula for UiO-66 as determined from TGA analysis of MOF shown below corresponding dialysis bags. b) TGA trace of samples UiO-66 before dialysis (black), UiO-66 after dialysis after thermal activation (red)

Evidence for the existence of the aperture-opened intermediate was obtained by subjecting UiO-66 to dialysis under conditions that were best for encapsulation (Figure 3-

5a). We hypothesized that if linkers were to dissociate from UiO-66 to form the aperture-opened intermediate, then they would diffuse through the dialysis bag instead of re-associating with UiO-66. Periodic removal of water external to the dialysis bag would ultimately result in UiO-66 that contained more missing terephthalic linkers. Consistent with these expectations, thermogravimetric analysis (TGA) of UiO-66 after dialysis revealed that there was less weight percentage loss around 400 °C for the UiO-66 after dialysis in water for 18 days, which was indicative of less terephthalic acid linkers per zirconium node compared to UiO-66 before dialysis[8b] (Figure 3-5b).

Next, to illustrate that encapsulation of guest molecules requires properly-sized guest molecules for diffusion through opened apertures (e.g. 2 → 3, Scheme 3-1), Brilliant Blue G (BBG) was subjected to the same encapsulation conditions (Figure 3-6a). BBG (26 Å) is larger than the successfully-encapsulated R6G (12 Å) (Figure 3-6b), and the size of the opened apertures that would result upon dissociation of a terephthalic acid linker (12 Å). Therefore, if aperture-opening was the key step for R6G encapsulation, BBG should not be encapsulated. Consistent with this rationale and unlike R6G, BBG demonstrated no appreciable incorporation (0.01 mmol/mg) beyond the amount adsorbed to the surface of the MOF (Figure 3-6c). In addition, the leaching experiments were carried out using R6G dye as a probe, where the encapsulated dye molecules were exposed to various solvents (Table 3-1). Understanding the nature of guest leaching was crucial for applying this aperture-opening encapsulation strategy in catalysis. The leaching experiment here using dye as a probe provided insight into the leaching behavior of the following organometallic complexes.

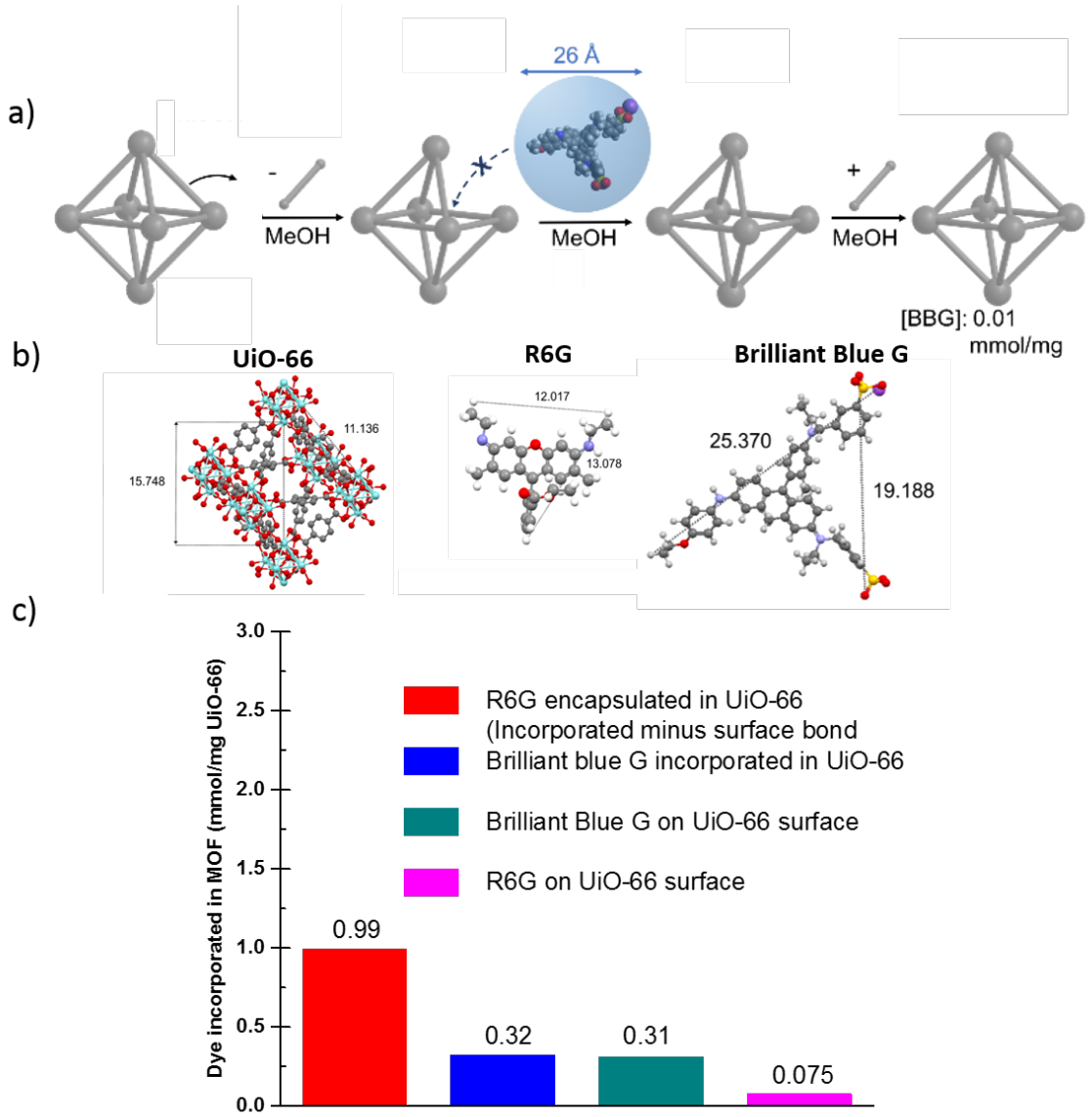

Figure 3-6. a) Attempted encapsulation of BBG in UiO-66 in methanol at 55 ºC for five days. b) Comparison of molecular size between MOF host (Left), Rhodamine 6G (Middle), Brilliant Blue G (Right). c) Comparison of the amount of Brilliant Blue G physically adsorbed on UiO-66 and incorporated through aperture opening encapsulation, and its comparison to R6G encapsulated in UiO-66 and on UiO-66.

Table 3-1. Observation of guest leaching from R6G@UiO-66 in DMF, methanol, a DMF/DBU mixture, and water for catalysis.

Solvent	Dye retained (%)
Methanol	75.1 ± 1.22
DMF	85.4 ± 8.61
DMF/DBU mixture	93.0 ± 6.43
25% Formic acid in DMF	86.2 ± 6.31
50% Methanol in DMF	92.6 ± 4.32
Water	52.1 ± 1.45

3.3 Encapsulation of a homogeneous catalyst into UiO-66

One catalyst candidate identified for CO_2 hydrogenation reaction was (^{i}PrPNP)Ir(CO)H_3 (^{iPr}PNP = 2,6-bis((i-propyl-phosphino)methyl)pyridine) (**1**) by Nozaki. Another catalyst (^{tBu}PNP)Ru(CO)HCl (^{tBu}PNP = 2,6-bis((di-*tert*-butyl-phosphino)methyl)pyridine) (**2**) was a highly active catalyst in non-aqueous condition.[9] **2** was popularized by Milstein[10] and explored extensively for CO_2 hydrogenation by Pidko.[7b,11] Both catalysts are suitable as a guest molecule in UiO-66 because they are larger than the UiO-66 aperture size but smaller than its pore size (Figure 3-7). It is also appropriate for our strategy because both are soluble and stable in methanol. **2** is an active catalyst for CO_2 hydrogenation in DMF/1,8-diazabicyclo(5.4.0)undec-7-ene (DBU) mixtures, while **1** is active in aqueous alkaline base.[11b]

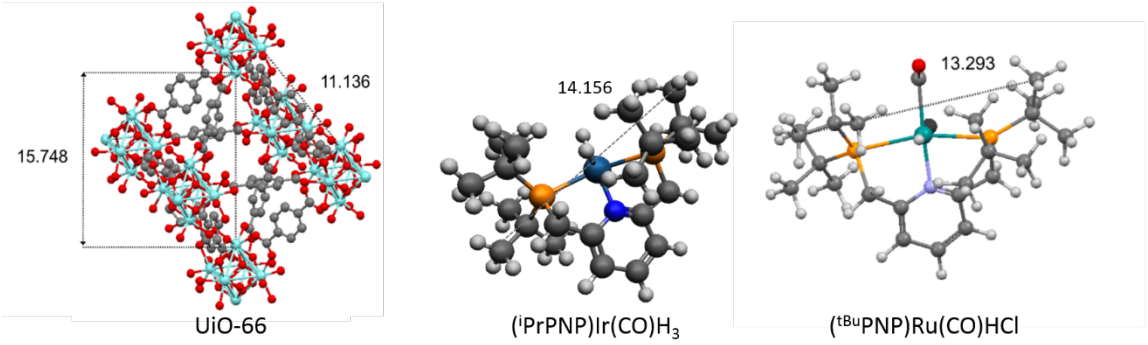

Figure 3-7. Comparison of molecular size between MOF host (Left), (^{i}PrPNP)Ir(CO)H_3 (Middle), and (^{tBu}PNP)Ru(CO)HCl (Right).

The encapsulated iridium and ruthenium catalysts, henceforth referred to as **1**@UiO-66 and **2**@UiO-66, were prepared by exposing UiO-66 to the complexes in methanol at 55 ºC for five days.[12] After a pretreatment procedure to remove surface-bound complex (See Experimental Section), the loading was determined from analysis of the digested solid via inductively coupled plasma optical emission spectrometry (ICP-OES). From the ratio of ruthenium to zirconium in **2**@UiO-66, the catalyst loading was determined to be 0.35 wt. ‰. The phosphorous to ruthenium ratio was 2:1, suggesting that the ligand did not dissociate from the ruthenium complex. ^{1}H-NMR analysis of the ruthenium complex that remained in the supernatant indicated that it was unchanged during encapsulation, which further supported the absence of complex decomposition during the loading process. Powder X-ray diffraction (PXRD) analysis indicated that the crystal structure of UiO-66 was unchanged after encapsulation (Figure 3-8). The same analysis was applied for **1**@UiO-66, where ICP-OES and PXRD analysis suggested the iridium complex retained its structural integrity after the encapsulation.

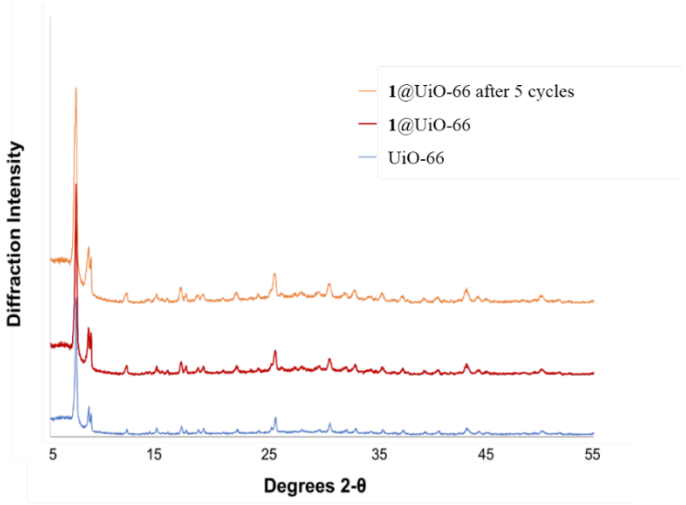

Figure 3-8. Comparison of crystallinity of pristine UiO-66 (blue), **2**@UiO-66 before catalysis (red) and **2**@UiO-66 after 5 cycles of catalysis (yellow) by PXRD.

Catalyst **1** and **1**@UiO-66 were subjected to catalysis due to the easy access to the catalyst. The catalytic results showed the encapsulation did not sacrifice the accessibility of the catalyst where both homogeneous catalyst and the encapsulated catalyst gave similar yield under the same condition. Again, the ICP-OES analysis of the **1**@UiO-66 revealed that the iridium catalyst still retained its structural integrity after the catalysis with 0.42 wt. ‰ catalyst loading.

To provide additional support that the iridium complex in **1**@UiO-66 is encapsulated in the MOF rather than on its surface, CO_2 hydrogenation reactions were carried out in the presence of thiols which are known poisons for many transition metal catalysts (Figure 3-9). The catalytic results showed that the activity of **1**@UiO-66 was less susceptible to the poisoning, suggesting the active site was indeed encapsulated in the cage.

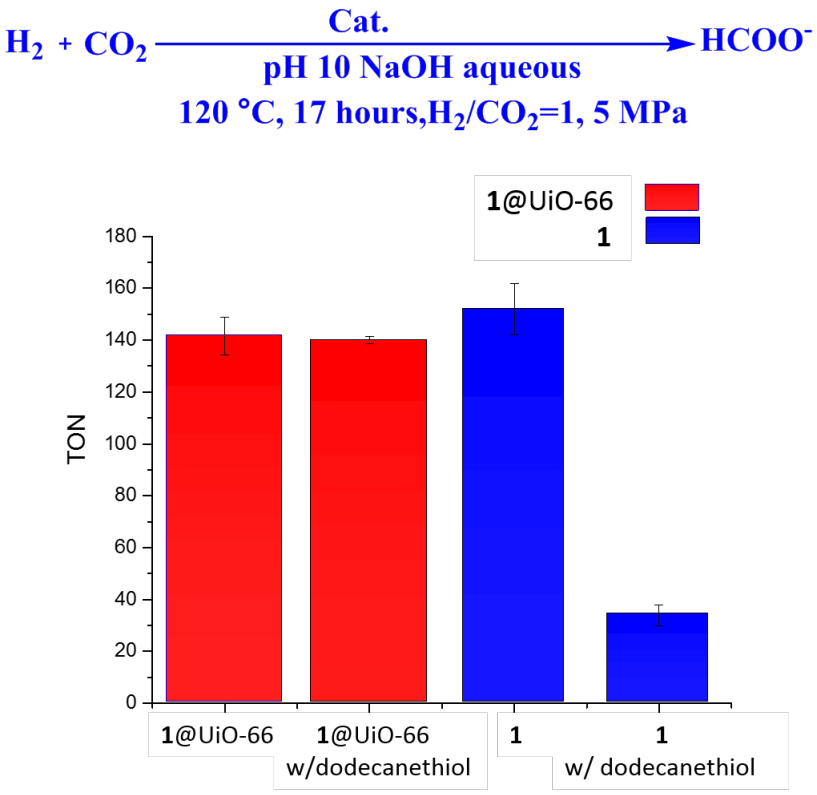

Figure 3-9. (a) Comparison of the activity of encapsulated (red) and homogeneous (blue) catalysts in the presence of a bulky thiol poison, 1-dodecanethiol. (b) Recyclability test of **1**@UiO-66.

One benefit of heterogenizing homogeneous catalyst is to increase its recyclability. **1**@UiO-66 show poor recyclability, as the TON gradually decreased, dropping 25% in the 2nd cycle and 50% in the 3rd cycle (Figure 3-10). Elemental analysis also showed that 26% and 55% of **1** leached out from the framework in the 2nd cycle and the 3rd cycle, according to the ICP-OES analysis of the digested **1**@UiO-66. These results suggested that the **1**@UiO-66 structure had significant leaching issue during catalysis, despite the success of the initial encapsulation of **1** into the cavity of UiO-66.

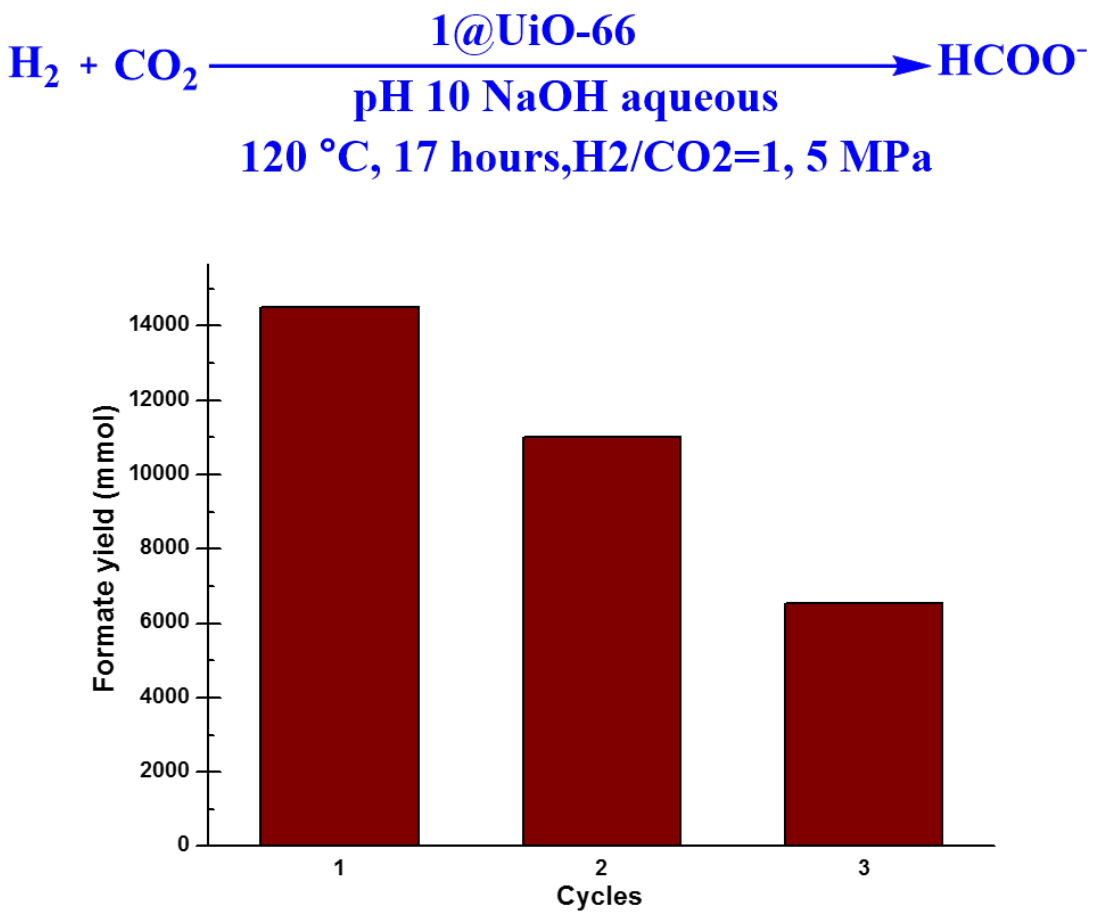

Figure 3-10. Recyclability test of **1**@UiO-66. Elemental analysis also showed that 26% and 55% of **1** leached out from the framework in the 2nd cycle and the 3rd cycle, according to the ICP-OES analysis of the digested **1**@UiO-66.

Past reports have suggested that linker exchange is sensitive to the acidity of the solvent.[13] Hence, we speculated that leaching of **1** was likely caused by the increased acidity of the solvent during catalysis as sodium hydroxide was consumed to form formate. Catalysis was thus performed with a variety of buffer solutions, such as TAPS/TAPS sodium salt buffer ([Tris(hydroxymethyl)methyl]-3-aminopropanesulfonic salt), Et_2NHCl/Et_2NH buffer, and Borax buffer, to test this hypothesis.

Table 3-2. CO_2 hydrogenation by **1** and **1**@UiO-66 using TAPS buffer with various conditions.

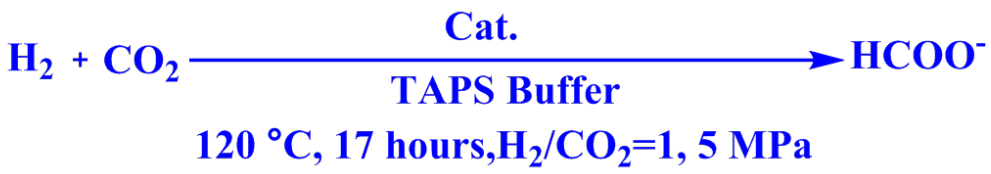

Entry	Catalyst	cat. (nmol)	Condition	Poison	Formate(umol)	TON	MOF structure
1	1	177	[TAPS]=1M	No	150	8650	
2	1	177	[TAPS]=0.2M	No	770	4380	
3	1	43.8	[TAPS]=0.2M	No	390	9090	
4	1	43.8	[TAPS]=0.2M	1-dodecanethiol	97	2230	
5	1	43.8	[TAPS]=0.1M	1-dodecanethiol, terephthalic acid	180	4340	
6	1@UiO66	43.8	[TAPS]=0.1M	No	330	7960	
7	1@UiO66	43.8	[TAPS]=0.1M	1-dodecanethiol	340	7790	Amorphous
8	1@UiO66	43.8	[TAPS]=0.05M	No	260	6110	
9	1@UiO66	43.8	[TAPS]=0.05M	1-dodecanethiol	230	5410	Partial crystalline

The yield to formate decreased by half as [TAPS] decreased from 1 M to 0.2 M, which suggesting the reaction became base limited at 0.2 M (Table 3-2, Entry 1, 2). Under [TAPS]=0.2 M condition, the TON of homogeneous catalyst was brought back to around 9000 by using three quarters of less catalyst loading in the reaction (Table 3-2, Entry 2,3). This observation suggested the homogeneous catalyst was likely deactivated under high catalyst loading due to bimolecular decomposition. The poisoning study was next carried out for homogenous catalyst under the aforementioned condition and the catalyst lost its 75% activity in the present of 1-dodecanethiol (Table 3-2, Entry 3,4) Interestingly, in the present of additional terephthalic acid, the homogeneous catalyst was less prone to poisoning compared to reactions without terephthalic acid (Table 3-2, Entry 5). With the understanding of how [TAPS] and thiol poison work in the homogeneous catalyst system,

we next set out to test the catalytic performance of the encapsulated catalyst under those conditions. Notably, PXRD analysis of the **1**@UiO-66 after the catalysis revealed UiO-66 was incompatible with the combination of 0.1 M [TAPS] and 1-dodecanethiol (Table 3-2, Entry 6, 7). The [TAPS] was further reduced to 0.05 M, and unfortunately, UiO-66 still turned partial amorphous after the catalysis (Table 3-2, Entry 8, 9). All these experiments suggested TAPS failed to improve the system in terms of both the poison study and the compatibility with the encapsulated catalyst.

Next, Et_2NHCl/Et_2NH buffer, and Borax buffer were attempted to improve the catalytic system. However, **1**@UiO-66 was not compatible under either of these two buffer systems.

The failed improvement of **1**@UiO-66 has led us to reevaluate the system and investigation was drawn to **2**@UiO-66 which was active in a aprotic and polar solvent instead, such as DMF.

Due to the robustness of the catalyst, **2**@UiO-66 was mixed with virgin UiO-66 with no catalyst in the framework to lower the catalyst loading. Afterwards, a pretreatment method involving running the catalyst at elevated temperature was necessary to remove all the surface bond catalyst. Consistent with the complex integrity being maintained during the encapsulation process was the observation that **2**@UiO-66 is an excellent catalyst for CO_2 hydrogenation (TON: 2.9E05), comparable to the homogeneous ruthenium catalyst (TON: 3.1E05). A key difference between the homogeneous ruthenium catalyst, and the **2**@UiO-66 encapsulated catalyst is the ability to recycle the catalyst.[14] As shown in Figure 3-11a, **2**@UiO-66 retained its activity through five cycles. PXRD analysis after the fifth cycle and the absence of terephthalic acid in the ^{1}H-NMR spectrum of the reaction

supernatant provided support that the UiO-66 host maintained its integrity. The ruthenium loading in **2**@UiO-66 after the fifth cycle detected by ICP-OES was 0.35 wt. ‰ with a phosphorous: ruthenium ratio of 2.4, similar to the catalyst composition prior to the first cycle. Additionally, the supernatant from reactions using **2**@UiO-66 was inactive for CO_2 hydrogenation, providing more evidence that catalyst leaching did not occur.

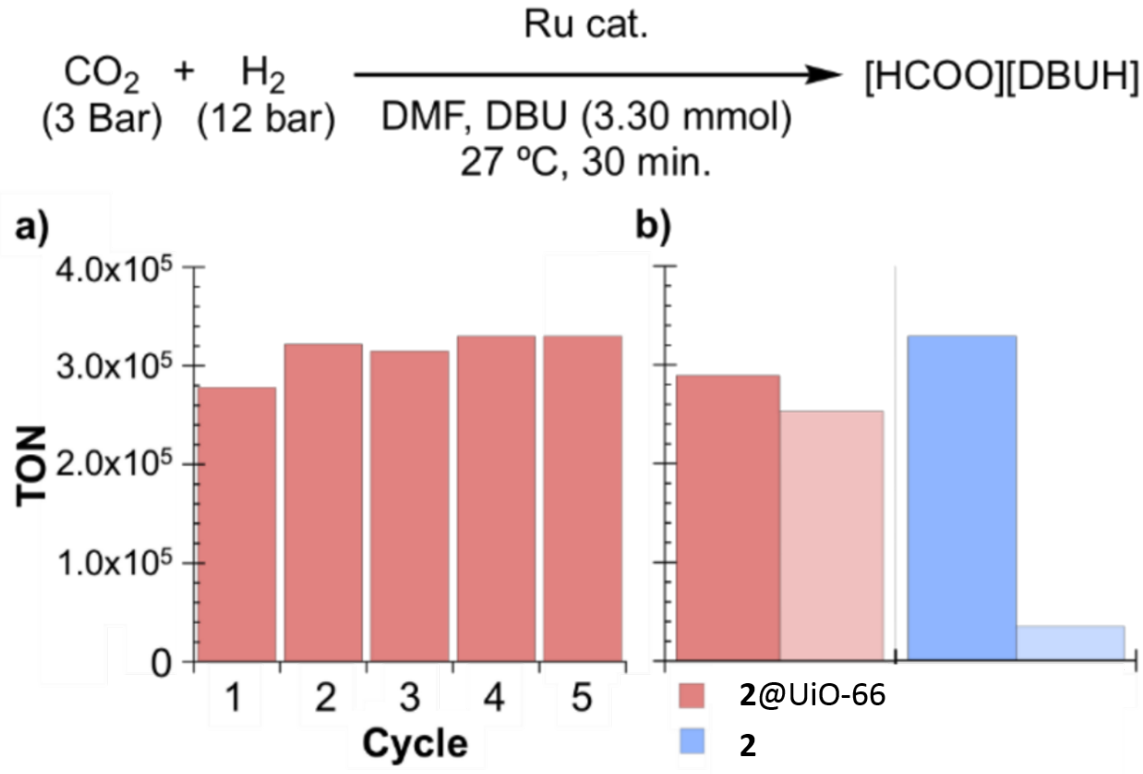

Figure 3-11. a) Activity of **2**@UiO-66 (TON = mmol $HCOO^-$/mmol Ru) upon catalyst recycling. b) comparison of catalyst activity in first cycle (dark) to that upon addition of a second aliquot of DBU (light).

Recyclability and stability of the encapsulated catalyst was further evaluated by an alternative method. A second aliquot of DBU was added to reactions catalyzed by **2** and **2**@UiO-66, and the reaction mixtures were then re-subjected to the hydrogenation conditions. A significant decrease in activity was observed for the reaction catalyzed by **2**,

whereas activity remained virtually the same for the reaction catalyzed by **2**@UiO-66 (Figure 3-11b). This outcome suggests that bimolecular decomposition limits recyclability of the homogeneous catalyst, which is not the case for **2**@UiO-66.[11b] Additional evidence that the homogeneous catalyst undergoes bimolecular catalyst deactivation more readily than the encapsulated catalyst was obtained by evaluating the activity of the two catalysts at different catalyst concentrations (Figure 3-12). The homogeneous catalyst demonstrated a polynomial decrease in turnover number with increasing catalyst loading, which is characteristic of a catalyst that undergoes bimolecular catalyst deactivation. In contrast, turnover in **2**@UiO-66 was constant irrespective of catalyst loading, which is expected for a catalyst that does not undergo bimolecular decomposition.

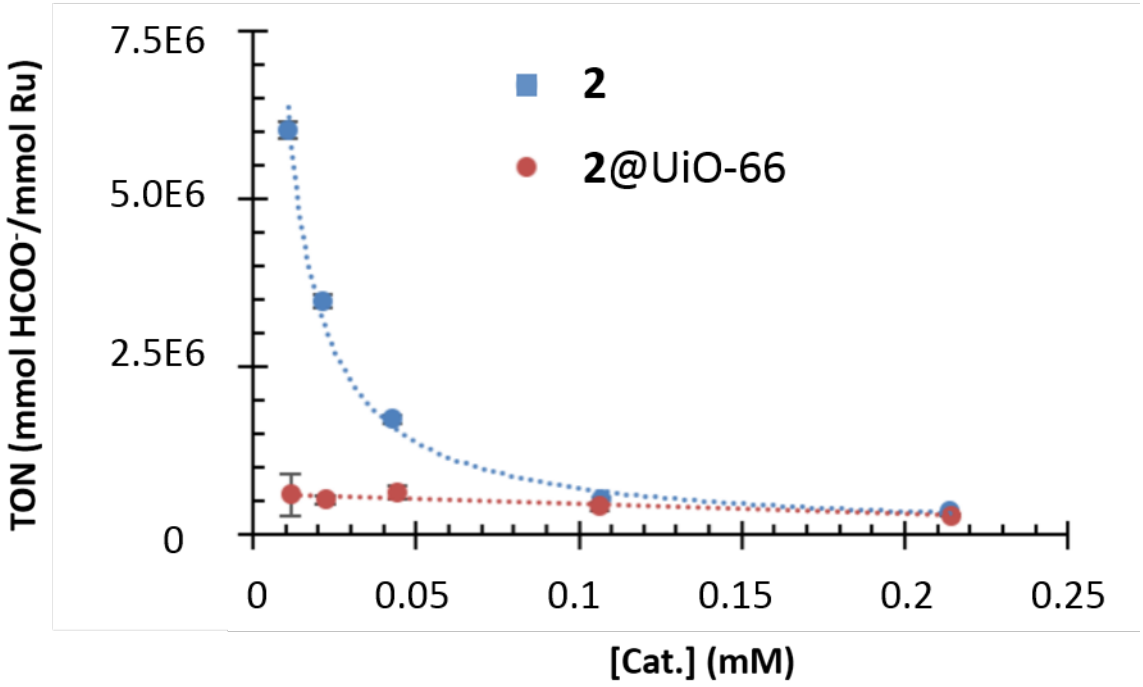

Figure 3-12. Turnover number for homogenous catalyst (blue) and hybrid catalyst (red) as a function of catalyst concentration (mM).

The susceptibility of the catalysts to poisoning was next probed by carrying out catalysis in the presence of a series of thiols (Figure 3-13). In all cases, catalytic activity was higher for **2**@UiO-66 compared to **2** in the presence of the thiol poisons. Moreover, all reactions catalyzed by **2** were poisoned to approximately the same degree regardless to the identity of the thiol poison. In contrast, poisoning in reactions catalyzed by **2**@UiO-66 was dependent on the identity of the thiol, with the most effective poisons being the least sterically demanding. These results are consistent with the catalyst being situated inside, instead of on the surface of UiO-66, because more facile diffusion of the smaller thiols through the aperture of UiO-66 is expected, resulting in more poisoning of the catalyst than with larger and more sterically bulky thiol poisons.[15]

For comparison, a sample in which the complex was adsorbed to the surface of MOF crystals was also prepared, which will be referred to as **2**onUiO-66. After pretreatment of **2**onUiO-66, the catalyst loading was determined to be nearly an order of magnitude lower ([Ru] = 0.0375 ‰) than the loading in **2**@UiO-66.

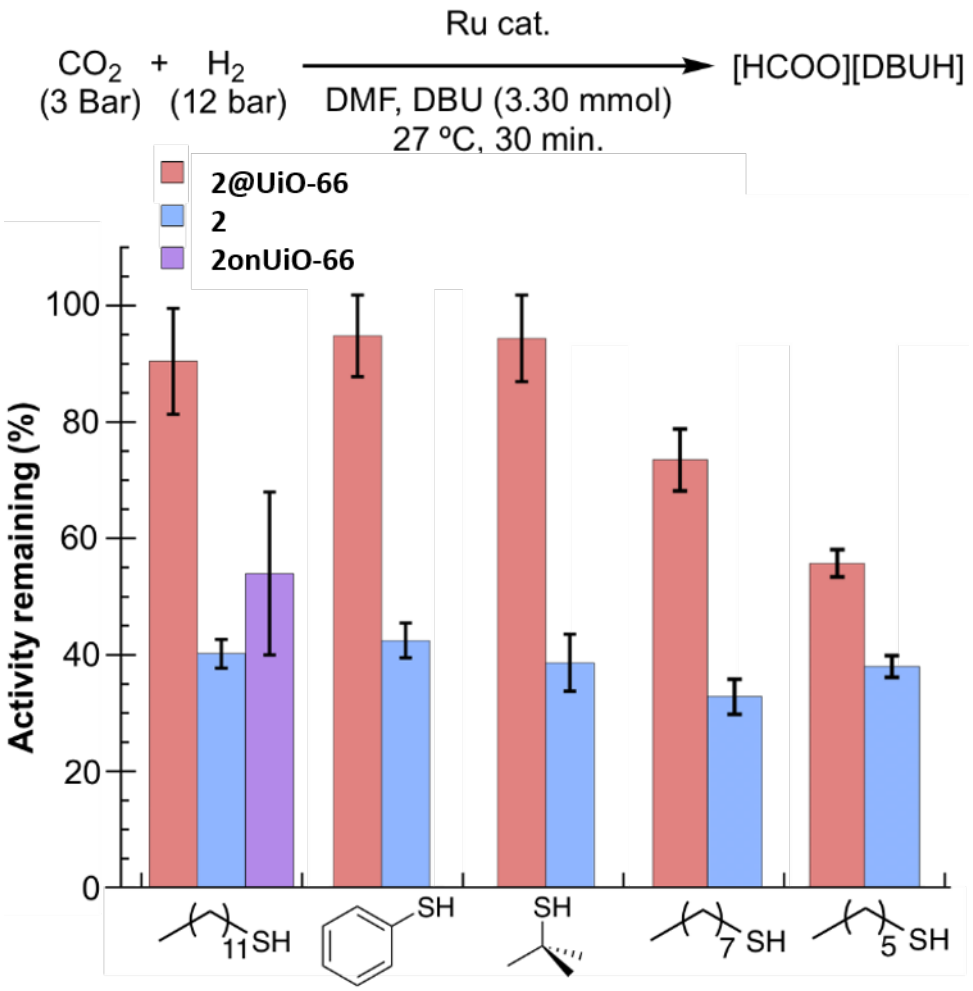

Figure 3-13. Comparison of the activity of homogeneous (left) and encapsulated (right) catalysts in the presence of differently sized thiol poisons.

So far we have been able to show that the solvent dependency of the aperture-opening encapsulation allows us to rationally choose solvents that prevent active sites from leaching in catalysis. The combined results of **1**@UiO-66 and **2**@UiO-66 again suggest that leaching of the active site during catalysis is facilitated by protic and polar solvents such as H_2O, and can be prevented in aprotic and polar solvent such as DMF.

3.4 Summary

In summary, a new method for encapsulation of a transition metal complex within a MOF was developed that capitalizes on the existence of solvent-dependent, aperture-opening events resulting from dissociative linker exchange reactions in MOFs. An encapsulated catalyst for CO_2 hydrogenation prepared using this method exhibited greater recyclability, slower bimolecular deactivation events, and resistance to poisoning compared to its homogeneous counterpart. It is necessary to select a catalyst that is stable in protic solvent and active in aprotic solvent to maximize the aperture-opening encapsulation and minimize the leaching issue during the catalysis. These benefits are a direct consequence of the molecular size-selectivity and isolation of individual complexes encapsulated within the solid framework. Notably, the new method for encapsulation does not require engineering of the guest or host materials, allowing for independent modification of the host material and guest catalyst structure. This feature makes it easier to exploit the unique advantages for catalysts encapsulated in molecularly sized cages.[16]

The distribution of active sites is important for the catalytic performance of the host-guest composite. The aforementioned strategies like anchoring (Chapter 1) usually results in active sites distributed in a mixture of encapsulated and surface-bond species, which does not fully take advantage of the well-defined local environment of the cavity of MOF. Anchoring the catalyst to the MOF nodes or bridging linker also lead to less freedom in catalyst mobility, which could cause inferior catalytic activity. The 'Ship-in-a-bottle' approach and strategies relying on electrostatic interaction between the host and guest highly depend on the identity of the host and guest. Unlike any of those strategies, 'aperture-opening encapsulation' provides a practical method allowing for the active sites to be incorporated exclusively in the cavity without being chemically bound to the MOF

itself. The next important question to ask is how the distribution of the catalyst is in the MOF crystal as a result of the 'aperture-opening encapsulation'. Are the active species in cages closer to the surface or are they distributed throughout the MOF crystal? Answering this question is beneficial for addressing some of the important topics in heterogenzing a homogeneous catalyst, such as understanding the role of mass transport. We will shed some insight on these important topics in the next chapter.

3.5 Experimental section

General Considerations Unless otherwise stated, all manipulations were carried out in air using standard analytical procedures. Catalytic carbon dioxide hydrogenation reactions were carried out in 5.0 mL ampules placed in a 450 mL stainless steel Parr reactor with stirring. Included with each reaction were positive and negative controls (using (^{tBu}PNP)Ru(CO)HCl and no catalyst, respectively) to ensure proper operation and ensure that no cross contamination between ampules occurred. To ensure that all catalyst activity in the hybrid materialwas coming from the encapsulated complex, a control reaction with virgin UiO-66 was carried out, which revealed only trace amounts of formate being formed. Experiments carried out in an air-free environment were conducted under a positive pressure of N_2 using standard glovebox or Schlenk line techniques.[17] UiO-66 was synthesized as previously described. (^{tBu}PNP)Ru(CO)HCl was synthesized following a procedure adapted from the literature.[8b] All [Ru]@UiO-66 catalyst employed was pre-treated as noted and subjected to serial solid dilution with UiO-66 in a mortar and pestle to achieve sufficiently low catalyst loading so that the reactions were not base-limited. [Ru]-on-UiO-66 used in catalysis was subjected to solid dilution without pre-treatment because this procedure led to complete removal of catalyst from the surface of the MOF.

2,6-lutidine (Aldrich), di-tert-butylchlorophosphine (Acros Organics), polyvinylpyrrolidone (TCI), and Rhodamine 6G (Sigma-Aldrich) were purchased from the indicated sources and used without further purification. Dialysis tubes were purchased from BioDesignDialysis Tubing with 15.5 mm wet diameter, 1.91 ml/cm volume and 8000 MWCO. STA analysis was carried out in NETZSCH STA 449F. Powder X-ray diffraction traces were collected on a Bruker AXS diffractometer with Cu Kα radiation (λ=1.5418 Å). ^{1}H-NMR and ^{31}P-NMR spectra were collected on a Varian Unity INOVA spectrometers (400 MHz, 500 MHz, or 600 MHz, as indicated), with all chemical shifts reported in ppm. Chemical shifts were reported in reference to tetramethylsilane and phosphoric acid for ^{1}H-NMR and ^{31}P-NMR spectra, respectively (δ 0.0 ppm for both). Formate production in catalysis was quantified using ^{1}H NMR spectroscopy using benzene (10 μL) as an external standard in a mixture of D_2O (450 μL) and reaction mixture (250 μL). ^{1}H-NMR spectra were acquired in 16 transients. ^{31}P-NMR spectra were acquired in 160 transients. All centrifugation steps were performed at 4000 revolutions per minute for 10 minutes using a Thermo Scientific CL2 centrifuge unless otherwise noted. All UV-visible absorbance measurements were obtained using a refurbished Molecular Devices Spectramax M5 spectrometer. Inductively coupled plasma optical emission (ICP-OES) spectrometry was recorded in an Agilent 5100 instrument that was calibrated using known concentrations of standard solutions to quantify Zr, Ru, and P. Ru (1000±4 ppm), P (100.04±0.55 ppm), Zr (999±5 ppm) single elemental standards were purchased from Inorganic Ventures.

Digestion of R6G/UiO-66 samples Each dried solid sample (5 mg) was added to a 1.5-mL centrifugation tube. Dimethylsulfoxide (1.5 mL) was added to each sample. One

drop of 15 wt% hydrofluoric acid was added to each sample, which was then left to digest overnight. Each sample was then neutralized using excess sodium bicarbonate and subjected to centrifugation.

Development of calibration curves Rhodamine 6G was weighed directly in a 50-mL volumetric flask, which was then filled to the volumetric marking with the solvent to be tested. This solution was then distributed among as many 20-mL scintillation vials as necessary. 1 mL of each calibration solution was removed and diluted using a volumetric flask (10 mL or 50 mL) to yield various concentrations to be used to calibrate. The absorbance of each solution was taken at 530 nm and 25 ºC using a compatible cuvette.

Encapsulation of Rhodamine 6G in UiO-66, R6G@UiO-66 Following a procedure similar to previously published procedure,[5] the intended encapsulation solvent (15 mL) was added to a 20-mL scintillation vial for each sample or to 20 mL crimp-sealed vials for reactions carried out at 85 ºC. UiO-66 (15 mg) and Rhodamine 6G (14.8 mg) were added to the vial, which was then sealed and heated at the noted temperature (55 ºC or 85 ºC) for five days. Upon cooling, the solid sample was isolated by centrifugation, and then triturated by washing the solid with a 14 wt.% polyvinylpyrrolidone mixture in methanol followed by centrifugation. Trituration was carried out twice more and the samples were allowed to dry in air at room temperature overnight. The MOF material was digested using the above digestion procedure, and the absorbance of each resulting solution was collected at 530 nm and 25 ºC in DMSO using a 0.7-mL VWR quartz cuvette. The concentration of the dye was determined by comparison to a standard curve, which was then related to the amount of digested MOF to get the loading of Rhodamine 6G in UiO-66.

Physical mixture control sample, R6GonUiO-66 UiO-66 (15 mg in each vial) was weighed out in a 20-mL scintillation vial. Methanol (15 mL) was added to this vial, which was subjected to sonication for approximately 10 minutes to disperse the solid. Rhodamine 6G (14.8 mg) was added to this vial, which was inverted twice, then immediately subjected to centrifugation. The supernatant was then decanted and the solids were obtained without further washing.

I/A Measurements A "Surface-bound dye" sample was prepared using the above procedure. This sample and all R6G@UiO-66 samples were added to separate 20 mL scintillation vials. All solids were dispersed in neat methanol, and transferred to quartz cuvettes. The samples were excited at 530 nm and emission intensity measurements were obtained at 552 nm. The solids were then allowed to air-dry overnight. The solids were then digested using the above procedure and the absorbance of each resulting solution at 530 nm and 25 ºC was obtained using a 0.7-mL VWR quartz cuvette in dimethyl sulfoxide. These readings were normalized by mass and analyzed to find a ratio of fluorescence intensity to absorbance of the solution.

Influence of exogenous terephthalic acid linker concentration on dye encapsulation in R6G@UiO-66 The general procedure used for encapsulating Rhodamine 6G was used as described above except different amounts of terephthalic acid (30.3 mg, 60.6 mg, 90.9 mg, or 250.9 mg) were also added to the reaction and an additional washing step using N,N'-dimethylformamide in place of the PVP/methanol solution. Analysis of dye encapsulation was carried out in an analogous fashion as described above.

Rhodamine 6G leaching studies from R6G@UiO-66 Solid samples of R6G@UiO-66 (encapsulated in water at 55 ºC, 5 mg each) were weighed out in separate

20 mL scintillation vials and dried for three days in a vacuum oven at 130 ºC to remove residual water. Solvent (5.0 mL) was added to each of these vials, which were then sealed and heated for two days at either 55 ºC or 85 ºC. The solid from the samples were isolated by centrifugation, washed three times with a mixture of polyvinylpyrollidone (PVP) in methanol (14 wt %), then allowed to dry in air overnight at room temperature. The dye concentration was then determined as described above. The resulting dye loading values were compared to loadings from R6G@UiO-66 obtained from the same source directly after its synthesis.

Synthesis of 2,6-bis((di-*tert*-butylphosphino)methyl)pyridine (^{tBu}PNP) The synthesis of this species was adapted from a literature procedure.[10] On a Schlenk line under nitrogen atmosphere, a solution of 2,6-lutidene (0.54 mL, 4.7 mmol) in diethyl ether (1.96 mL) was prepared in a 50-mL two-neck flask, then cooled to 0 ºC. n-Butyl lithium in hexanes (2.0 M, 4.8 mL, 9.6 mmol) was added slowly by syringe to this cooled solution, which resulted in the homogeneous reaction mixture to turn a dark maroon-red color. The reaction mixture was allowed to warm to room temperature and heated to 40 ºC for fifteen hours. After cooling to room temperature, the reaction mixture was brought -78 ºC where di-tert-butylchlorophosphine (1.85 mL, 9.74 mmol) was added dropwise to the reaction mixture via syringe. The reaction mixture was allowed to warm to room temperature where it reacted for one hour, retaining its deep red coloration. The reaction mixture was quenched with degassed methanol (40 mL), resulting in a color change to light-yellow. The reaction mixture was left without stirring for one hour to allow the resulting lithium salt to settle. The liquid product mixture was transferred by cannula filtration to another two-necked flask, and the lithium salt was washed twice with diethyl ether. The solvent mixture was

removed by vacuum at 55 ºC resulting in an off-white solid. This solid was transferred to the glovebox and extracted in diethyl ether, then recrystallized in diethyl ether at -40 ºC. The clear-white crystalline product was recovered and washed with cold diethyl ether (492.8 mg, 53% yield). ^{1}H and ^{31}P-NMR spectra matched literature values.[10] $^{31}P\{^{1}H\}$ NMR (C_6D_6): 37.60 (s). ^{1}H NMR (C_6D_6): 1.13 (d, $^{3}J_{PH}$) 10.8 Hz, 36H, $PC(CH_3)_3$), 3.09 (d, $^{2}J_{PH}$) 2.4 Hz, 4H, CH_2P), 7.17 (d, $^{3}J_{HH}$) 7.5 Hz, 2H, pyridine-H3,5), 7.25 (t, $^{3}J_{HH}$) 7.8 Hz, 1H, pyridine-H4). $^{13}C\{^{1}H\}$ NMR (C_6D_6): 29.68 (d, $^{2}J_{PC}$) 54.0 Hz, $PC(CH_3)_3$), 31.69 (d, $^{1}J_{PC}$) 94.2 Hz, CH_2P), 32.23 (d, $^{1}J_{PC}$) 103.8 Hz, CH_2P), 120.64 (d, $^{3}J_{PC}$) 36.6 Hz, pyridine-C3,5), 135.68 (s, pyridine-C4), 161.40 (d, $^{2}J_{PC}$) 59.4 Hz, pyridine-C2,5).

Synthesis of (^{tBu}PNP)Ru(CO)HCl. (Adapted from literature)[7b] In an inert atmosphere glove box, $RuHCl(PPh_3)_3(CO)$ (257.7 mg, 0.2707 mmol) was suspended in tetrahydrofuran (10 mL) in a 100 mL Schlenk tube. ^{tBu}PNP (110.2 mg, 0.2786 mmol) was added to this suspension. The solution was diluted with THF (20 mL). This reaction mixture was sealed and removed from the glovebox, then heated at 65 ºC for 3 hours. The resulting mixture was returned to the glove box and filtered through celite on a coarse fritted funnel. The remaining THF was removed *en vacuo*. The resultant oily yellow solid was dissolved in THF (0.5 mL), and precipitated into pentane to give a yellow solid. This solid was then washed with pentane (50 mL), and the crude product was recrystallized in pentane at -40 ºC. The recrystallized product (87.3 mg, 0.155 mmol, 57.4% yield) ^{1}H and ^{31}P-NMR spectra matched literature values.

Synthesis of UiO-66 This synthesis was adapted from the literature[8b] N,N'-dimethylformamide (DMF) (25 mL) was added to a 45 mL Teflon-lined steel autoclave. Zirconium tetrachloride (241.4 mg, 1.036 mmol) and terephthalic acid (342.8 mg, 2.063

mmol) and concentrated hydrochloric acid (180 μL) was added to the autoclave, which was then sealed and heated at 220 ºC for 20 hours. The reaction mixture was then allowed to cool to room temperature and agitated to suspend the solid. This solid was isolated by centrifugation, then washed with DMF (15 mL) and left to soak in this solvent overnight. This solid was isolated again by centrifugation and washed twice with methanol (15 mL), then left to soak overnight in methanol. The solid was isolated by centrifugation and dried in a vacuum chamber overnight, then dried overnight in an oven at 70 ºC. Powder X-Ray diffraction traces matched literature precedents.[8b]

Synthesis of 2@UiO-66 In an inert atmosphere glovebox, methanol (10 mL) was added to a 20-mL crimp-sealed vial in a glovebox. UiO-66 (200 mg) and (^{tBu}PNP)Ru(CO)HCl (5.0 mg, 5.3 μmol) were added to the vial, which was then sealed. This mixture was heated at 55 ºC for five days, and then allowed to cool to room temperature. The resulting mixture was brought into a glovebox. The vial was unsealed, and the resultant mixture was transferred to a 20 mL scintillation vial and subjected to centrifugation. Trituration was achieved by decanting the supernatant from this mixture, which was set aside for NMR analysis. The remaining solid was further triturated three times with methanol (10 mL) each time using centrifugation to ensure quantitative mass transfer. After three washing cycles, 188 mg of a pale yellow solid (94%) was obtained. This solid was dried overnight in a vacuum chamber. A portion of this material (100 mg) was suspended in 15 mL of degassed DMF, and then transferred as a slurry to a 20 mL ampule containing a stir bar using a 9” glass pipet. 1,8-diazabicyclo[5.4.0]undec-7-ene (DBU) (2.465 mL, 2.505 g, 15.50 mmol) was added to this ampule. The ampule was added to a 450-mL stainless steel Parr reactor. The vessel was purged with carbon dioxide for 5

minutes and then pressurized to 42 psi. The vessel was then pressurized with hydrogen gas to achieve a total pressure of 542 psi at room temperature. The reactor was heated to 129 ºC and left to react for 45 minutes. The heating mantle was removed, the reactor was cooled using a room-temperature water bath, and the pressure was released slowly from the vessel. The vessel was opened and the ampule was removed. The reaction mixture was transferred as a slurry to a 20-mL scintillation vial and subjected to centrifugation at 3000 revolutions per minute for 15 min, after which the supernatant was decanted. The solid was triturated twice with methanol (20 mL) followed by centrifugation and dried overnight in a vacuum chamber to give a pale yellow powder (93 mg, 93%). The loading of catalyst in the MOF was determined by ICP-OES (see "Preparation of (^{tBu}PNP)Ru(CO)HCl stock solutions" and "Digestion of UiO-66 for ICP-OES analysis", below).

Procedure for preparing 2onUiO-66 In an inert atmosphere glovebox, methanol (10 mL) was added to a 20-mL scintillation vial. UiO-66 (100 mg) and (^{tBu}PNP)Ru(CO)HCl (5.0 mg, 5.3 μmol) were added to the vial, which was then sealed. This mixture was agitated by shaking for several seconds, then immediately subjected to centrifugation. Trituration was achieved by decanting the supernatant from this mixture. The remaining solid was further triturated three times with methanol (10 mL) each time using centrifugation to ensure quantitative mass transfer and dried overnight in a vacuum chamber. After three washing, 92 mg of a pale yellow solid (92%) was obtained and used without further manipulation in catalysis. This solid was dried overnight in a vacuum chamber and the loading of catalyst in the MOF was determined by ICP-OES (see "Preparation of (^{tBu}PNP)Ru(CO)HCl stock solutions" and "Digestion of UiO-66 for ICP-OES analysis", below).

Preparation of (^{tBu}PNP)Ru(CO)HCl stock solutions (^{tBu}PNP)Ru(CO)HCl (5.0 mg, 5.3 μmol) was added to a 20 mL scintillation vial. Degassed N,N'-dimethylformamide (DMF) (3.0 mL) was added to this vial. From this solution, 1.0 mL was extracted and diluted to 5.0 mL in a class A 10-mL volumetric flask using DMF. Further serial dilution was achieved by removing 1.0 mL of this solution and diluting to 10 mL in a class A 10-mL volumetric flask. The catalytic solution (0.033 μM) was transferred to a 20-mL scintillation vial, sealed, and stored at -40 ºC in a glovebox. Solutions were allowed to warm to room temperature before use in catalysis.

General Procedure for the hydrogenation of carbon dioxide For homogeneous catalysis, a stock solution (3.0 mL) of (^{tBu}PNP)Ru(CO)HCl in DMF was prepared as previously noted and added to a 5.0-mL ampule using a 9" glass pipet. For the heterogeneous catalyst, unless otherwise noted, the solid was suspended in 3 mL of degassed DMF, and then transferred as a slurry to 5-mL ampules using a 9" glass pipet. 1,8-diazabicyclo[5.4.0]undec-7-ene (DBU) (0.493 mL, 0.501 g, 3.30 mmol) was added to each ampule with a stir bar. These ampules were arranged in a 450 mL stainless steel Parr reactor that contained a thermocouple to ensure thermostated reactions. The vessel was placed on a Parr instrument stand atop a stir plate and surrounded by a heating mantle. The reaction vessel was purged with carbon dioxide for 5 minutes and then pressurized to 42 psi. The vessel was pressurized with hydrogen to a total pressure of 212 psi, and the reactions were allowed to react at room temperature for 30 minutes. Upon conclusion of the reaction, the heating mantle was removed and the pressure was released slowly from the vessel. The vessel was opened and the ampules were removed. The colorless slurry obtained from reactions involving heterogeneous catalysis were transferred to 20 mL

scintillation vials and subjected to centrifugation, after which the supernatant was decanted. The homogeneous reactions were removed from the ampoules and the supernatant was analyzed as described below without further manipulation. A 0.25 mL aliquot of the supernatant was removed and combined with benzene (0.01 mL) and D_2O (0.45 mL) in 4.0-mL vials. These mixtures were then transferred to individual NMR tubes and quantitative ^1H NMR was used to determine the yield of formate by integration of the formate peak in reference to benzene.

Digestion of UiO-66 for ICP-OES analysis Solid MOF material (5.00 mg) was weight out into a 1.5 mL Teflon vial. DMSO (300 μL) and 1 drop of 15 wt.% aqueous hydrofluoric acid solution were added in sequence. The mixture was sonicated for 1 minute and left to digest for 1 hour. The digested samples then heated to approximately 150 °C overnight in a sand bath open to the air to remove solvent. The resulting solid was dissolved and transferred to a 20 mL glass scintillation vial using a mixture (10% v/v) of hydrochloric acid in deionized water (300 μL). Each sample was diluted with additional deionized water (3.7 mL) and analyzed by ICP-OES.

ICP-OES Standard preparation Four standards were prepared by dilution from commercially available zirconium (999 ± 5 ppm), ruthenium (999 ± 5 ppm), and phosphorus (100.04 ± 0.55 ppm) standards using serial dilution in grade A volumetric glassware to cover the expected concentration ranges. The standards were then employed in a calibration curve to determine the loading of catalyst in a tested solid. These standards consisted of Zr/Ru/P concentrations in ppm at the proportions: 250/5/5, 150/2/2, 25/0.5/0.5, 2.5/0.05/0.05

Procedure for carbon dioxide hydrogenation recycling studies using 2@UiO-66 Carbon dioxide hydrogenation was carried out using the "general procedure for carbon dioxide hydrogenation" at 5x scale in a 20-mL ampule. The solid was washed twice with methanol (20 mL) and dried overnight in a vacuum chamber between cycles.

Procedure for carbon dioxide hydrogenation in the presence of thiols Carbon dioxide hydrogenation was carried out using the "general procedure for carbon dioxide hydrogenation" with the addition of different thiols. 1-dodecanethiol (0.15ml, 0.627 mmol), 1-hexanethiol (0.09 ml, 0.627 mmol), 1-octanethiol (0.11ml, 0.627 mmol), benzenethiol (0.064 ml, 0.627 mmol), 2-ethylhexanethiol (0.109 ml, 0.627 mmol), or tert-butylthiol (0.07ml, 0.627 mmol) was added to the reaction mixture in a fume hood. These ampules were added to a 450 mL stainless steel Parr reactor. Upon conclusion of the reaction, the heating mantle was removed and the pressure was released slowly from the vessel into a fume hood. The vessel was brought to a fume hood and opened and the ampules were removed. The ampules and reactor were cleaned after the reaction with a solution of bleach (20%) in water.

Procedure for carbon dioxide hydrogenation to test catalyst deactivation Carbon dioxide hydrogenation was carried out using the "general procedure for carbon dioxide hydrogenation". After the first cycle, an aliquot of reaction mixture (0.25 mL) was removed from the ampule set aside in a small vial. DBU (0.493 mL, 3.30 mmol) was added to each ampule, and the ampules were again subjected to reaction conditions. Catalyst deactivation was determined as the difference between formate production in the first and second reactions.

Procedure for BET measurement The samples "UiO-66" and "UiO-66 after linker exchange" (with no catalyst being added) were incubated in methanol for 7 days with solvent replaced every twelve hours. The solids were isolated by centrifugation and dried, then activated by first ramping the temperature to 200 °C at a rate of 5 °C/min, remaining constant for 10 minutes, then ramping to 270 °C and remaining constant for twelve hours. The nitrogen gas adsorption-desorption was carried out on quodrasorb evo provided by ShanghaiTech University.

Procedure for UiO-66 dialysis experiment A dialysis tube was soaked in water first for 5 minutes until it was fully solvated. One side of the tube was clamped tightly and UiO-66 (200 mg) and deionized water (3ml) were added to the tube, and then the other side was clamped. The dialysis tube was placed in a 1-L beaker and suspended in water (1 L) with stirring at 55 ºC for 18 days. The external water was refreshed daily, and water removed was collected and concentrated by heating for LC-MS analysis.

Procedure for STA analysis Prior to STA analysis, all samples were dried under vacuum and heat at 150 °C to ensure the complete dryness before the TGA measurement. Analysis was carried out in an Al_2O_3 crucible on NETZSCH STA 449F1. Samples were thermally activated in air by STA with first ramping to 270 ºC with 10 ºC/min and stay isotherm at 270 ºC for 12 hours and cool back down to room temperature. After the thermal acitivation to get rid of any residue solvent and organic impuries, the samples were ran from room temperature to 900 ºC at 5 ºC/min in air. Unless otherwise stated, all the measurements were carried out using air as carrier gas and nitrogen as the protection gas.

Calculation of missing linkers from TGA data[8b]

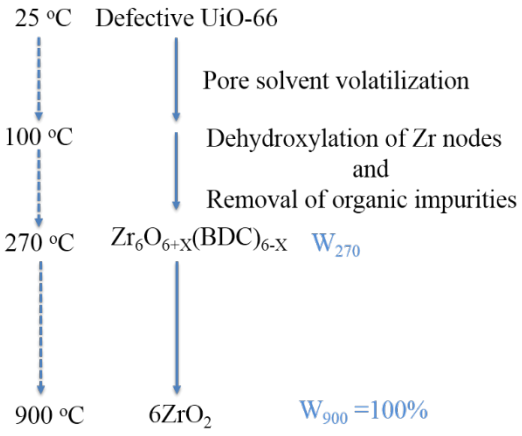

The missing linker (x) per Zr_6-oxo cluster of the defective UiO-66 was calculated by the following formula

$$X= 6 - \frac{W270 - W900}{(Wtheo.270 - W900)/6} = 6 - \frac{W270 - W900}{(220.2\% - 100\%)/6} = 6 - \frac{W270 - 100\%}{20.03\%}$$

Where, the final weight W_{900} ($6ZrO_2$) was normalized to 100%. $W_{theo.270}$ is the ideal weight of a defect-free UiO-66, $Zr_6O_4(OH)_4(BDC)_6$, after the normalization which equals to 220.2%. W_{270} is the actual normalized weight at 270 ºC detected from TGA trace of the sample.

Encapsulation of Brilliant Blue G in UiO-66, Dye-at-UiO-66 Following a procedure similar to previously published procedure,[5] methanol (15 mL), UiO-66 (15 mg) and Brilliant blue G (15 mg) were added to a 20-mL scintillation vial. The vial was then sealed and heated at 55 ºC for five days. Upon cooling, the solid sample was isolated by centrifugation, and then triturated by washing the solid with a 14 wt.% polyvinylpyrrolidone mixture in methanol followed by centrifugation. Trituration was carried out twice more and the samples were allowed to dry in air at room temperature overnight. The MOF material was digested using the above digestion procedure, and the

absorbance was collected at 624 nm and 25 ºC in DMSO using a 0.7-mL VWR quartz cuvette. The concentration of the dye was determined by comparison to a standard curve.

Physical mixture control sample, dye-on-UiO-66 UiO-66 was weighed out in a 20-mL scintillation vial. Methanol (15 mL) was added to this vial, which was subjected to sonication for approximately 10 minutes to disperse the solid. Brilliant Blue G (15 mg) was added to this vial, which was inverted twice, then immediately subjected to centrifugation. The supernatant was then decanted and the solids were obtained without further washing.

Detection of formate by mass spectrometry A carbon dioxide hydrogenation product mixture (3 mL) was placed in a 50-mL round-bottom flask and hooked up to an air-free manifold. This flask was put under vacuum and heated at 120 ºC for three hours. The mixture was allowed to cool to room temperature and transferred to a 20-mL scintillation vial. Methanol (5 mL) was then added to this mixture, and the product formate was detected using Direct Analysis in Real Time in the negative ion mode on a JEOL AccuTOF 4G LC-Plus. (CH_2O_2 expected: 45.017g/mol; found: 45.000 g/mol)

Procedure for testing pre-treated homogeneous catalyst mixture for catalytic activity A solution of (^{tBu}PNP)Ru(CO)HCl (7.0 mg, .0125 mmol) in DMF was prepared and added to a 5.0-mL ampule, then subjected to pre-treatment as described above. The supernatant was concentrated by rotary evaporation and tested by ^{31}P-NMR to observe decomposition of the homogeneous catalyst. Carbon dioxide hydrogenation was carried out using the "general procedure for carbon dioxide hydrogenation". This experiment was run simultaneously with a sample of (^{tBu}PNP)Ru(CO)HCl that had not been pre-treated to properly observe the effect of pre-treatment on the homogeneous catalyst.

Procedure for testing pre-treated supernatant and UiO-66 for catalytic activity UiO-66 (10 mg) and (^{tBu}PNP)Ru(CO)HCl (7.4 mg, 0.0132 mmol) were mixed together in a 5.0-mL glass ampule and subjected to pre-treatment as described above. The solid and supernatant were then separated by centrifugation. The solid was washed once with methanol and dried overnight in a vacuum chamber. The supernatant was concentrated by rotary evaporation and tested by ^{31}P-NMR to observe decomposition of the homogeneous catalyst. Carbon dioxide hydrogenation was carried out using the "general procedure for carbon dioxide hydrogenation" for each of these species. These experiments were run simultaneously with a sample of [Ru]@UiO-66 to ensure the activity of the hybrid species in the absence of activity for the pre-treated UiO-66 and supernatant.

Statement on base limitation in CO_2 hydrogenation studies The conditions reported for carbon dioxide hydrogenation using (^{tBu}PNP)Ru(CO)HCl as the catalyst result in full conversion of the requisite DBU base additive to [HCOO][DBUH].[18] While these conditions maximize catalytic turnover, the status of the base as the limiting reagent in the system precludes an accurate comparison between the activity of the homogeneous and encapsulated catalysts. Therefore, the reaction conditions were modified by lowering the reaction temperature, catalyst loading, and hydrogen pressure so that the reaction was not base-limited (i.e. [formate]:$[DBU]_0 \leq 1$)

Statement on alternative method for detection of formate Though detection of formate in a product mixture is achievable through either mass spectrometry or NMR spectroscopy, we primarily utilized the latter method for ease of quantification.

Statement on the effect of pre-treatment upon the identity of the active species Two control experiments were carried out that provide indirect evidence that the initially formed

catalyst is unlikely being converted into a different catalytically active species. Firstly, the homogeneous complex was exposed to the pretreatment conditions using significantly higher concentrations than were used in reactions catalyzed by **2**@UiO-66. Evaluation of the supernatant by NMR spectroscopy revealed that the homogeneous complex was converted into a new species that was found to be catalytically inactive for CO_2 hydrogenation. To rule out the possibility that a new heterogeneous catalyst supported by the MOF may form that is otherwise unstable in the absence of the MOF, we have carried out a second control experiment, in which the homogeneous complex is exposed to the pretreatment procedure in the presence of virgin UiO-66. As was found with the homogenous complex, neither the supernatant nor the heterogeneous material that was recovered were found to be catalytically competent for CO_2 hydrogenation.

Synthesis of (^{i}Pr-PNP)Ir(H)$_3$ To a 50ml stainless autoclave, $[Ir(coe)_2Cl]_2$ (291 mg, 0.325 mmol, 1 equiv.), ^{i}Pr-PNP (389 mg, 1.05 mmol, 3.2 equiv.), and THF (4 ml) were charged under N_2 atmosphere. The mixture was pressurized with H_2 (360 psi) and stirred at 90 °C for 6 hours. After 6 hours, the color of reaction mixture turns from red initially into light yellow. Solvent was removed in vacuum, and then add approximate 1 ml of THF to re-dissolve most of the solid in. Drop-wisely add 3 ml hexane to precipitate the product out. After precipitation, wait a couple of minutes until the supernatant is clear light yellow and then carefully decant the upper layer. The residue yellow-white compound was then washed extensively with large quantities of hexane to get rid of minor impurities. The residue solvent was removed in vacuum to deliver a pale yellow compound (^{i}Pr-PNP)Ir(H)$_2$Cl. Afterwards, to a solution of (^{i}Pr-PNP)Ir(H)$_2$Cl (60 mg, 0.1 mmol, 1 equiv.) in THF (2mL), a slurry suspension of NaH (163 mg, 6.8 mmol, 68 equiv.) in THF was

added drop-wise. The mixture was stirred at room temperature for 24 hours and the color of the solution changes from orange yellow to red wine. The mixture was filtered through a pad of Celite. The solvent was removed in vacuum, and the title compound was recrystallized from a mixture of THF/hexane as yellow crystals. ^{1}H, ^{31}P NMR spectra match literature precedence.[9]

Reference

(1) (a)Sumida, K.; Rogow, D. L.; Mason, J. A.; McDonald, T. M.; Bloch, E. D.; Herm, Z. R.; Bae, T.-H.; Long, J. R. *"Carbon Dioxide Capture in Metal–Organic Frameworks"* Chem. Rev. **2012**, *112*,724-728; (b)Li, J.-R.; Kuppler, R. J.; Zhou, H.-C. *"Selective gas adsorption and separation in metal-organic frameworks"* Chem. Soc. Rev. **2009**, *38*,1477-1480.

(2) Horcajada, P.; Gref, R.; Baati, T.; Allan, P. K.; Maurin, G.; Couvreur, P.; Férey, G.; Morris, R. E.; Serre, C. *"Metal–Organic Frameworks in Biomedicine"* Chem. Rev. **2012**, *112*,1232-1236.

(3) Kreno, L. E.; Leong, K.; Farha, O. K.; Allendorf, M.; Van Duyne, R. P.; Hupp, J. T. *"Metal–Organic Framework Materials as Chemical Sensors"* Chem. Rev. **2012**, *112*,1105-1110.

(4) (a)Lee, J.; Farha, O. K.; Roberts, J.; Scheidt, K. A.; Nguyen, S. T.; Hupp, J. T. *"Metal-organic framework materials as catalysts"* Chem. Soc. Rev. **2009**, *38*,1450-1456; (b)Hu, P.; Morabito, J. V.; Tsung, C.-K. *"Core–Shell Catalysts of Metal Nanoparticle Core and Metal–Organic Framework Shell"* ACS Catal. **2014**, *4*,4409-4412; (c)Liang, J.; Liang, Z.; Zou, R.; Zhao, Y. *"Heterogeneous Catalysis in Zeolites, Mesoporous Silica, and Metal–Organic Frameworks"* Adv. Mater. **2017**, *29*,1701139-1701160; (d)Manna, K.; Ji, P.; Lin, Z.; Greene, F. X.; Urban, A.; Thacker, N. C.; Lin, W. *"Chemoselective single-site Earth-abundant metal catalysts at metal–organic framework nodes"* Nat. Commun. **2016**, *7*,12610-12615.

(5) Morabito, J. V.; Chou, L.-Y.; Li, Z.; Manna, C. M.; Petroff, C. A.; Kyada, R. J.; Palomba, J. M.; Byers, J. A.; Tsung, C.-K. *"Molecular Encapsulation beyond the Aperture Size Limit through Dissociative Linker Exchange in Metal–Organic Framework Crystals"* J. Am. Chem. Soc. **2014**, *136*,12540-12546.

(6) Morabito, J. V., Li, Z., Byers, J. A., Tsung, C.-K., Boston College, Chestnut Hill, MA, Unpublished work, 2017.

(7) (a)Filonenko, G. A.; Conley, M. P.; Copéret, C.; Lutz, M.; Hensen, E. J. M.; Pidko, E. A. *"The impact of Metal–Ligand Cooperation in Hydrogenation of Carbon Dioxide Catalyzed by Ruthenium PNP Pincer"* ACS Catal. **2013**, *3*,2522-2526; (b)Filonenko, G. A.; Hensen, E. J. M.; Pidko, E. A. *"Mechanism of CO_2 hydrogenation to formates by homogeneous Ru-PNP pincer catalyst: from a theoretical description to performance optimization"* Catal. Sci. Technol. **2014**, *4*,3474-3478; (c)Ge, H.; Jing, Y.; Yang, X. *"Computational Design of Cobalt Catalysts for Hydrogenation of Carbon Dioxide and Dehydrogenation of Formic Acid"* Inorg. Chem. **2016**, *55*,12179-12185.

(8) (a)Cavka, J. H.; Jakobsen, S.; Olsbye, U.; Guillou, N.; Lamberti, C.; Bordiga, S.; Lillerud, K. P. *"A New Zirconium Inorganic Building Brick Forming Metal Organic Frameworks with Exceptional Stability"* J. Am. Chem. Soc. **2008**, *130*,13850-13855; (b)Shearer, G. C.; Chavan, S.; Ethiraj, J.; Vitillo, J. G.; Svelle, S.; Olsbye, U.; Lamberti, C.; Bordiga, S.; Lillerud, K. P. *"Tuned to Perfection: Ironing Out the Defects in Metal–Organic Framework UiO-66"* Chem. Mater. **2014**, *26*,4068-4071; (c)Loredana Valenzano, B. C., Sachin Chavan, Silvia Bordiga, Merete H. Nilsen, Søren Jakobsen,

Karl Petter Lillerud, and Carlo Lamberti *"Disclosing the Complex Structure of UiO-66 Metal Organic Framework: A Synergic Combination of Experiment and Theory"* Chem. Mater. **2011**, *23*,17001718.

(9) Tanaka, R.; Yamashita, M.; Nozaki, K. *"Catalytic Hydrogenation of Carbon Dioxide Using Ir(III)−Pincer Complexes"* Journal of the American Chemical Society **2009**, *131*,14168-14172.

(10) Hermann, D.; Gandelman, M.; Rozenberg, H.; Shimon, L. J. W.; Milstein, D. *"Synthesis, Structure, and Reactivity of New Rhodium and Iridium Complexes, Bearing a Highly Electron-Donating PNP System. Iridium-mediated Vinylic C-H Bond Activation"* Organometallics **2002**, 21, 812-818.

(11) (a)Filonenko, G. A.; Smykowski, D.; Szyja, B. M.; Li, G.; Szczygieł, J.; Hensen, E. J. M.; Pidko, E. A. *"Catalytic Hydrogenation of CO2 to Formates by a Lutidine-Derived Ru–CNC Pincer Complex: Theoretical Insight into the Unrealized Potential"* ACS Catal. **2015**, *5*,1145-1150; (b)Filonenko, G. A.; van Putten, R.; Schulpen, E. N.; Hensen, E. J. M.; Pidko, E. A. *"Highly Efficient Reversible Hydrogenation of Carbon Dioxide to Formates Using a Ruthenium PNP-Pincer Catalyst"* ChemCatChem **2014**, *6*,1526-1530.

(12) We have subsequently found that catalyst encapsulation over a 24-hour period achieved comparable loadings.

(13) Karagiaridi, O.; Bury, W.; Mondloch, J. E.; Hupp, J. T.; Farha, O. K. *"Solvent-Assisted Linker Exchange: An Alternative to the De Novo Synthesis of Unattainable Metal–Organic Frameworks"* Angewandte Chemie International Edition **2014**, *53*,4530-4535.

(14) Reports that the homogeneous catalyst can be recycled have appeared previously (see ref. 14b), but these studies were conducted by cycling between hydrogenation of CO_2 and dehydrogenation of formate under base-limiting condi-tions (see experimental section).

(15) Dinelli, G.; Civitano, L.; Rea, M. *"Industrial experiments on pulse corona simultaneous removal of NO_x and SO_2 from flue gas"* IEEE Transactions on Industry Applications **1990**, *26*,535-539.

(16) (a)Garcia-Garcia, P.; Muller, M.; Corma, A. *"MOF catalysis in relation to their homogeneous counterparts and conventional solid catalysts"* Chem. Sci. **2014**, *5*,2979-2983; (b)Davis, A. V.; Raymond, K. N. *"The Big Squeeze: Guest Exchange in an M4L6 Supramolecular Host" J. Am. Chem. Soc.* **2005**, *127*,7912-7916; (c)Hong, C. M.; Kaphan, D. M.; Bergman, R. G.; Raymond, K. N.; Toste, F. D. *"Conformational Selection as the Mechanism of Guest Binding in a Flexible Supramolecular Host"* J. Am. Chem. Soc. **2017**, *139*,8013-8016.

(17) Burger, B. J.; Bercaw, J. E. *"Vacuum line techniques for handling air-sensitive organometallic compounds"* ACS Symposium Series **1987**, 357, 79-115.

(18) Li, B.; Zhang, Y.; Ma, D.; Ma, T.; Shi, Z.; Ma, S. *"Metal-Cation-Directed de Novo Assembly of a Functionalized Guest Molecule in the Nanospace of a Metal–Organic Framework"* J. Am. Chem. Soc. **2014**, *136*,1202-1206.

Chapter 4. Investigating the effect of particle size on catalysis

4.1 The role of particle size in heterogeneous catalysis

Heterogeneous catalysts are favored in industrial applications due to their high activity, ease of recycling, resiliency to harsh conditions, and resistance to CO poisons.[1] As such, heterogeneous catalysis is estimated to have a global impact of around $10 trillion per year.[1] Common industrial catalysts include noble metals (e.g., Pt-Rh alloy nanoparticles can perform a variety of hydrogenations),[2] metal oxides (e.g., vanadium oxide catalyzes the synthesis of sulfuric acid, and iron oxides are involved in the formation of ammonia),[3] and inorganic conjugated frameworks (e.g., zeolites are responsible for the bulk of industrial alcohol dehydrogenation).[4] In particular, encapsulating homogeneous/heterogeneous catalyst into MOFs could potentially have advantages for catalytic performance especially for size selectivity due to the inherent selective sieving of the MOF cages. Studies have shown that catalyst activity is highly affected by changing the size of a catalytically active nanoparticle in a MOF.[5] However, there is a lack of understanding of how the change of MOF size affects the selectivity and activity of the composite when a homogeneous catalyst is encapsulated inside the cage. Understanding this effect is important to integrate the homogenous moiety onto the heterogeneous platform. This chapter focuses on how the change of MOF size can affect the catalytic performance of a homogeneous CO_2 hydrogenation catalyst encapsulated in the metal-organic framework UiO-66.

Extensive efforts have been made using MOFs to construct a host-guest catalyst system, including catalyst anchoring[6] and post-synthetic modification.[7] Recently, the role

the host structure plays in catalysis has begun to receive recognition despite the difficulty in synthesizing well-defined size and shape of the host material.[8] As a result, the rational design of size-controlled MOF crystals has not yet been used to mitigate possible mass transport limitations and enhance catalytic performance.

In the previous chapter, we demonstrated the successful encapsulation of a Ru-PNP pincer complex (**2**) in the cavity of UiO-66 by utilizing the 'aperture-opening encapsulation' that is made possible from the dissociative linker exchange reactions that occur for UiO-66 in protic solvents (Figure 4-1). The catalyst is referred to as **2**@UiO-66 and displays properties that are hybrid between homogeneous and heterogeneous catalysts: it is selective for the formation of formate, recyclable, resistant to thiol poisons, and does not suffer from bimolecular decomposition.[9]

a)

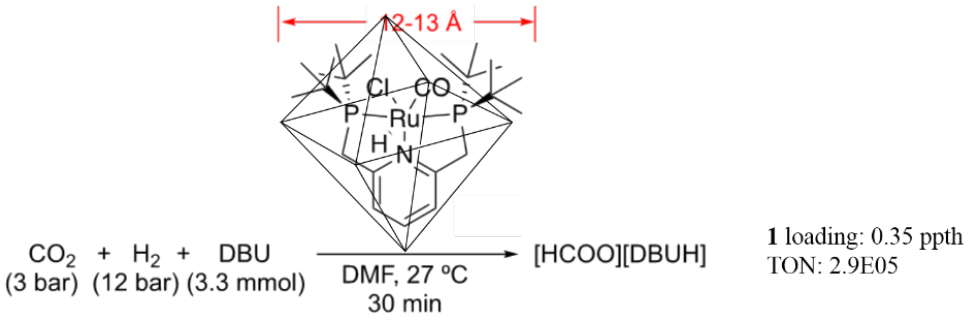

b)

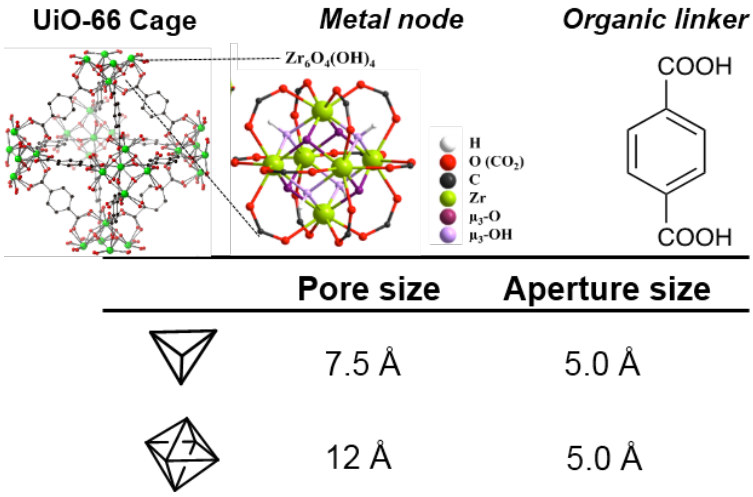

Figure 4-1. Structures of a)**2** catalyst, **2**@UiO-66 catalytic reaction and b) UiO-66 structure.

Despite these notable advantages, the homogeneous catalyst outperforms **2**@UiO-66 at low [Ru] (Figure 4-2). Mass transport limitations are a common issue for substrates and products in heterogeneous catalysis.[10] In this case, a low TON could be attributed to the limited mass transport of one of the reactants or the product from the reaction (or both). In order to understand the role that mass transport plays in CO_2 hydrogenation, it is first important to understand how the active sites are distributed in the inorganic matrix of **2**@UiO-66.

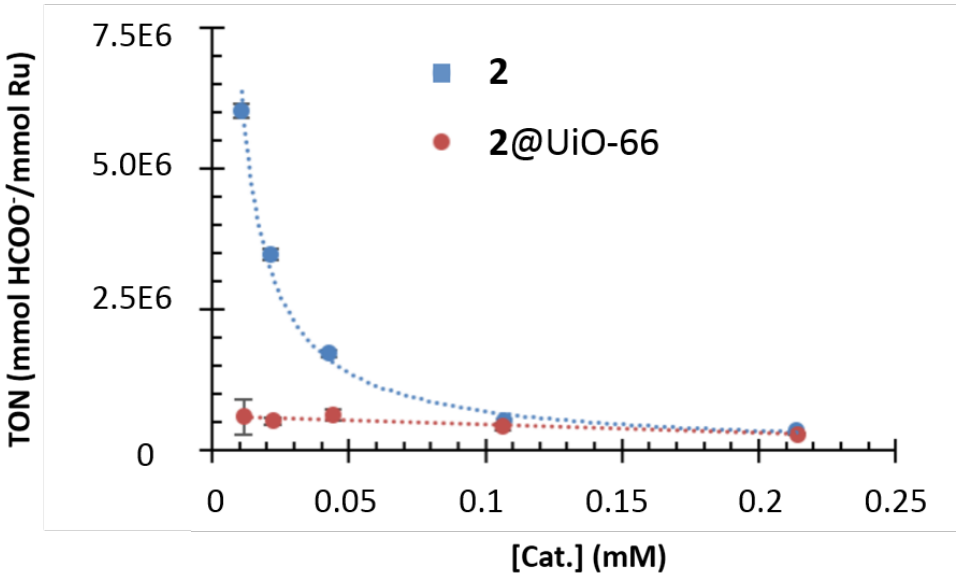

Figure 4-2. Turnover number for **2** (blue) and **2**@UiO-66 (red) as a function of catalyst.

We expect the distribution of active sites are related to the mechanism for encapsulation of the transition metal complex. Three competing factors are important for the aperture-opening encapsulation process: diffusion of the guest into the framework, diffusion of the guest within the framework, and the linker exchange rate of the terephthalic acid linkers. The distribution of the guest within the MOF crystal likewise depends on the relative rate of these three process.

Two extreme cases are possible, depending on the relative rates between the diffusion of the guest (into and within the framework) and the linker exchange (Figure 4-3). If the average diffusion rate is much faster than the rate of linker exchange, uniformly distributed **1**@UiO-66 throughout the MOF crystals is likely to result. Conversely, if the diffusion rate into the framework is larger but the diffusion rate within the framework is much slower than the rate of linker exchange, the active sites are more likely to be located in the outer shell, close to the crystal surface. If the two rates are similar, the distribution

will likely fall somewhere in between. It's worth noting that it is possible in the real situation that linker exchange and diffusion rates vary within the depths of the MOF crystal (i.e. it may become harder/easier for the linkers to dissociate and/or the complex to diffuse from one pore to the next).

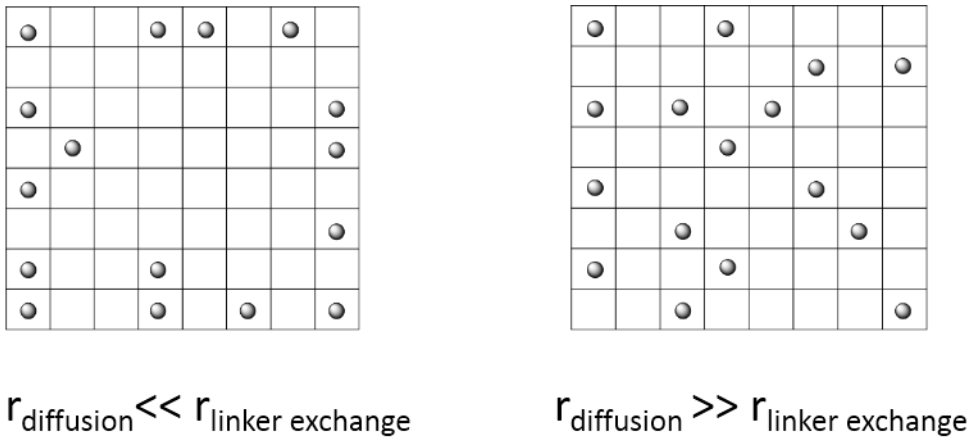

Figure 4-3. Two extreme situations of guests in a MOF matrix (left) distributed in the cage closer to the surface and (right) distributed throughout the whole MOF crystal.

To evaluate the importance of mass transport and to assess how metal complexes are distributed during aperture-opening encapsulation, **2** was encapsulated into UiO-66 of various sizes. If the TON of the hybrid catalyst increases as particle size decreases, then we mass transport of the product is likely causing the lower activity for the hybrid catalyst compared to the homogeneous catalyst. Moreover, this outcome would be more consistent with even distribution of the homogeneous catalyst through the MOF crystal. On the other hand, if the smaller UiO-66 particle size does not affect the TON, then the lower TON we observed in the hybrid catalyst is likely not from product diffusion limitations, and the active sites are likely located in the cavity closer to the surface.

4.2 Synthesis of UiO-66 particles with different sizes

Acetic acid is commonly utilized in MOF synthesis to slow down the nucleation process and achieve higher crystallinity and better morphology, which is due to the fact that acetic acid is a monocarboxylate that can bridge zirconium oxide clusters.[11] The advantage of using acetic acid, compared to other carboxylic acid modulators (e.g. benzoic acid), is that acetic acid also participates in the hydrolysis of Zr-oxo clusters.[12] Pursuant to our experimental goals outlined above, we followed a published method to synthesize a series of size-controlled UiO-66, where acetic acid and trimethylamine (NEt_3) was used as co-modulators (Table 4-1).[13] Here, acetic acid reacts with the organic base NEt_3. We hypothesized that varying the amount of NEt_3 can buffer the amount of acetic acid available to participate in the nucleation process. We believed doing so could alter the rate of nucleation, allowing for modulation of the size of UiO-66 crystals.

Table 4-1. UiO-66 synthesis with acetic acid/NEt_3 as co-modulator.

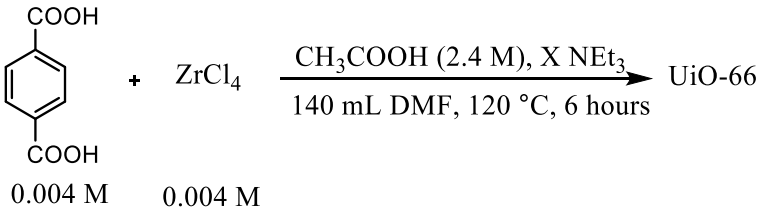

Entry	[NEt_3] (M)	Yield (%)	Average Size(μm)	Standard deviation
1	0	48	0.72	0.032
2	0.001	55	0.23	0.020
3	0.004	56	0.21	0.011
4	0.008	48	0.19	0.009

Small particle sizes were observed in the presence of trimethylamine and larger particle sizes were obtained in the absence of trimethylamine (Figure 4-4). This observation

is consistent with our hypothesis that the NEt_3 behaves like a buffer influencing the ability of the acetic acid to bind to the Zr-oxo clusters. The acidity of the solution containing NEt_3 changed dramatically before reaching the buffer equilibrium between acetic acid and NEt_3, substantially influencing the nucleation of UiO-66. The particular size significantly decreased upon addition of NEt_3. As [NEt_3] continues to increase, there is less acetic acid available to assist the formation of nucleation. The particle size did not continuously decrease in size with increasing NEt_3 but was rather insensitive to the amount of [NEt_3] added to the reaction. This is likely due to the fact that there is a constant amount of acetic acid participating in the formation of MOF crystals when acetic acid/NEt_3 reaches an equilibrium.

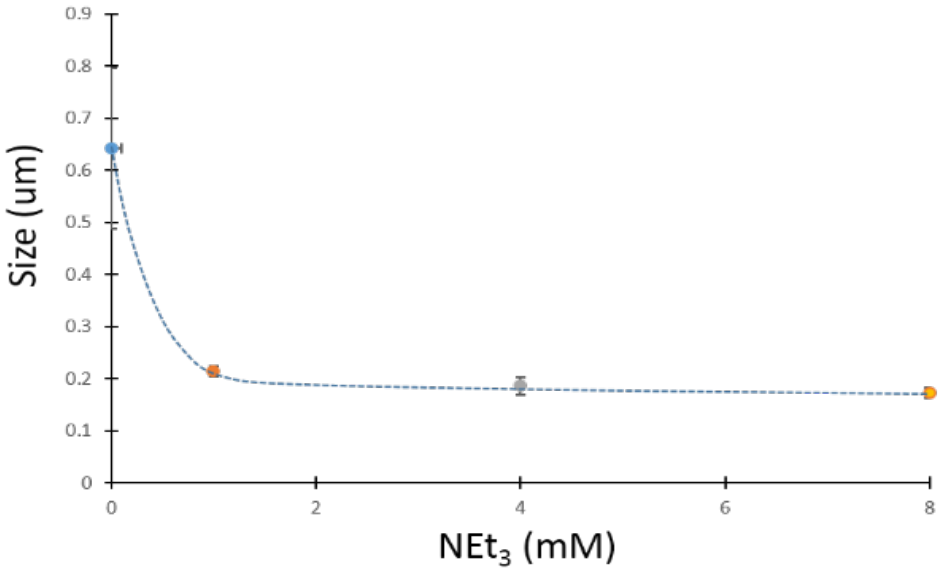

Figure 4-4. The average of the size of UiO-66 as the change of [NEt_3], and the error bar represents the average error. Size distribution was generated from manually counting 100 particles from scanning electron microscope (SEM).

We also notice from the particle counting that the size distribution is broader when no NEt_3 is added during the synthesis. (Figure 4-5) This observation suggests that nucleation is less well-controlled without the acetic acid/NEt_3 buffer. We speculate this originates from the fluctuating pH caused by the continuous consumption of acetic acid since there is no base to provide a buffer.

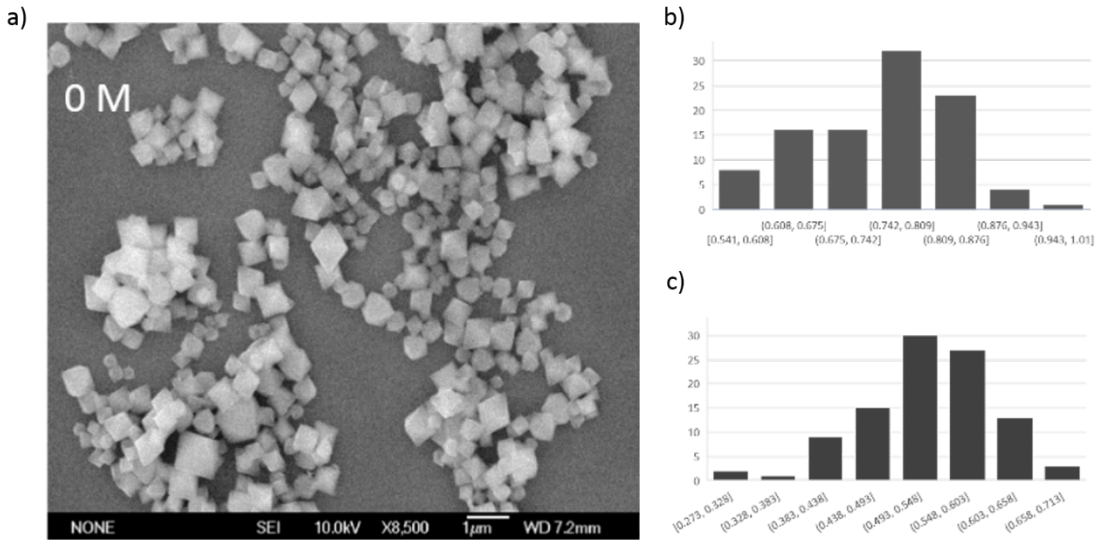

Figure 4-5. UiO-66 synthesized in the absence of NEt_3, a) SEM images, b) particle counting of one batch (average: 0.75 μm), c) particle counting of another batch synthesized in parallel (average: 0.53 μm) . SEM images and the particle size analysis demonstrate wide size distribution.

Benzoic acid with mono-carboxylate moiety has been widely used in modulating MOF synthesis. In particular, it's structural similarity with terephthalic acid makes it attractive in UiO-66 synthesis. Researchers have shown that benzoic acid can promote the formation of ''missing-cluster defects'' in the formation of UiO-66. In the formed "defective" UiO-66, the charge and coordination deficiencies are compensated by modulator ligands, which further causes the change of the particle size. As a result, the size

of UiO-66 can be potentially modulated by the varying the addition of benzoic acid as a modulator. While most study is focused on investigating the generated defect content, there are very limited reports on understanding the size effect from the use of benzoic acid. Herein, we propose to generate large particle size of UiO-66 by using the combination of benzoic acid and acetic acid.

The synthesis of UiO-66 was attempted by varying the amount of added acetic acid while keeping the amount of benzoic acid constant. Doing so allowed us to systematically approach the best combination of those two modulators. SEM images showed the size and shape of UiO-66 particles could be modulated by the addition of acetic acid and the most well defined shape and size were achieved when the largest amount of acetic acid was added (x=2.2) (Figure 4-6). The average size for x equals 2.2 was 1.3 μm calculated by counting at least 100 particles from the SEM image manually.

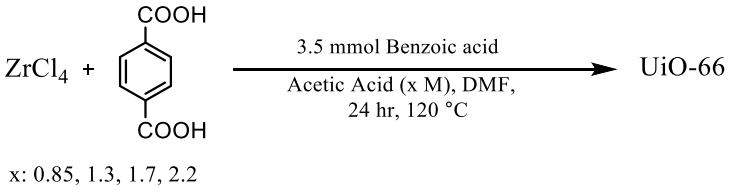

x: 0.85, 1.3, 1.7, 2.2

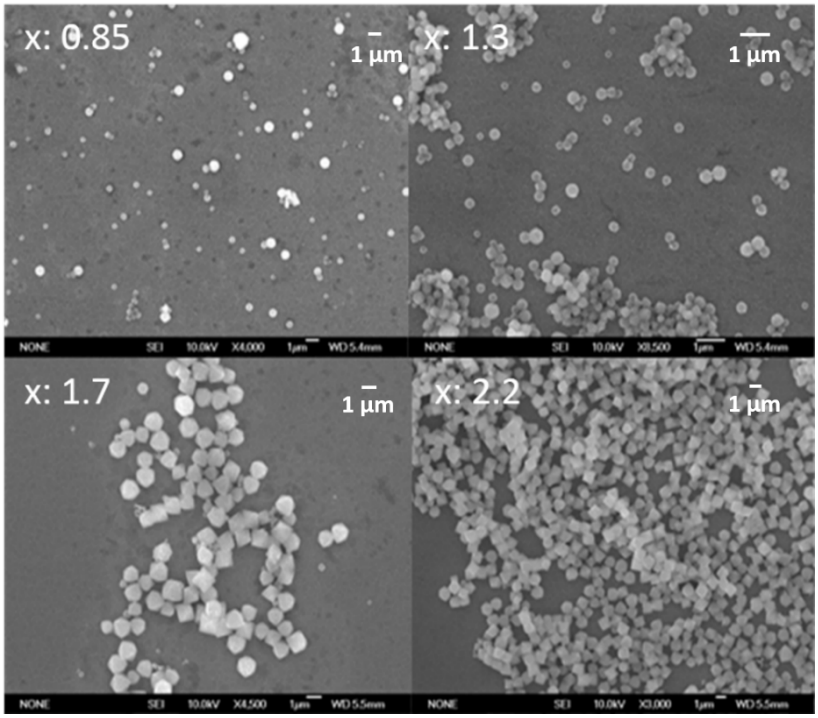

Figure 3-6. SEM images of synthesized UiO-66 particles with varying amount of acetic acid (x: 0.85, 1.3, 1.7, 2.2).

Next, three sizes (0.2 um, 0.7 um and 1.3 um) of UiO-66 were chosen to perform the aperture-opening encapsulation of the Ru-PNP pincer complex (Scheme 4-2).

Scheme 4-2. Synthesis of **2**@UiO-66 through aperture-opening encapsulation.

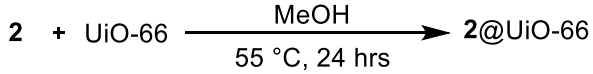

4.3 Catalytic performance of 2@UiO-66 at different UiO-66 particle sizes

To best compare the effect that UiO-66 crystal size has on catalytic efficiency in **2**@UiO-66 hybrid catalysts, the loading of **2** must be kept consistent in all particle sizes. The extent of encapsulation in this aperture-opening encapsulation process is believed to be proportional to the exposed surface area of solid as a result of diffusion control. Small particles are expected to incorporate more **2** per unit volume than large particles in the

presence of the same concentration of **2** in solution. This expectation was confirmed experimentally (Table 4-1, Entry 1-5). The loading of **2** in UiO-66 with the size of 0.2 μm was kept constant, and the loading of **2** in UiO-66 with the size of 0.7 μm was brought down to the same loading by changing the concentration of **2** in solution. Attempts with initial [Ru] brought from 0.5 mmol to 0.4 mmol in 20 ml DMF, the loading of 1 was approximately the same in UiO-66 at size of 0.2 um and 0.7 um. The P/Ru atomic ratio was found to be approximately 2 by ICP-OES from the digested composite. These data suggest the complex remains intact during the encapsulation process. A similar screening process was carried out with the size of 1.3 um particles, and the results were summarized in Table 4-1 (Entry 6).

Table 4-1. Attempts of obtaining three different sizes of [Ru]@UiO-66 with same [Ru] loading by varing the amount of initial [Ru]. The [Ru] loaing was determined by ICP-OES of disgested samples after pretreatment to remove the surface bond catalyst.

Entry	Samples	Size (um)	[Ru]/MeOH (20 ml)	[Ru] loading in UiO-66 (ppth)	P/Ru atomic ratio
1	**2**@UiO-66	0.2	2.5	0.040	2.4
2	**2**@UiO-66 #1	0.7	2.5	0.030	1.8
3	**2**@UiO-66 #2	0.7	5.2	0.065	1.8
4	**2**@UiO-66 #3	0.7	4.5	0.060	2.0
5	**2**@UiO-66 #4	0.7	4.0	0.038	2.5
6	**2**@UiO-66	1.3	5.1	0.039	2.2

To remove surface bound complex, the samples with different particle sizes were first subjected to the same pre-treatment conditions (45 mins, 129 °C, H_2: 37 bar, CO_2: 3 bar) as described in Chapter 3. As described in Chapter 3, **2**@UiO-66 had to be diluted with virgin UiO-66 to achieve catalyst loadings that were low enough so that reactions could be in run without complications from base limitations. The pretreated catalysts were

mixed with UiO-66 crystals with their own sizes (eg. **2**@UiO-66 with particle size of 0.2 um was diluted with 0.2 um empty UiO-66). Afterwards, the diluted samples were tested for catalysis.

The hybrid catalysts with different sizes exhibit the same activity and recyclability as the non-size-controlled sample (Figure 4-7). The surface area per volume being irrelevant to the catalyst activity suggests that the active sites are more likely to be distributed in the shell near the surface of UiO-66 particles using aperture-opening encapsulation. Compared to the post-linker functionalization encapsulation method where the active sites are likely distributed through the entire crystal, the aperture-opening encapsulation method provides a desired catalyst distribution that allows more active sites to be accessible to the substrates. To understand the mass transport with the base, NEt_3 with a smaller size than DBU was used as a base instead. Despite the lower TON of **2** and **2**@UiO-66 in the present of NEt_3 compared to DBU, the activity difference between **2** and **2**@UiO-66 is smaller in lower [Ru], from almost twelve times to less than twice for the ratio of homogeneous catalyst to the encapsulated hybrid catalyst (Figure 4-8). This observation suggested the discrepancy in activities could be attributed to the fact that large base has difficulties in accessing the catalyst through apertures of the MOF. Having catalyst predominately in the cages closer to the MOF surface and (or) using smaller base could potentially alleviate this issue.

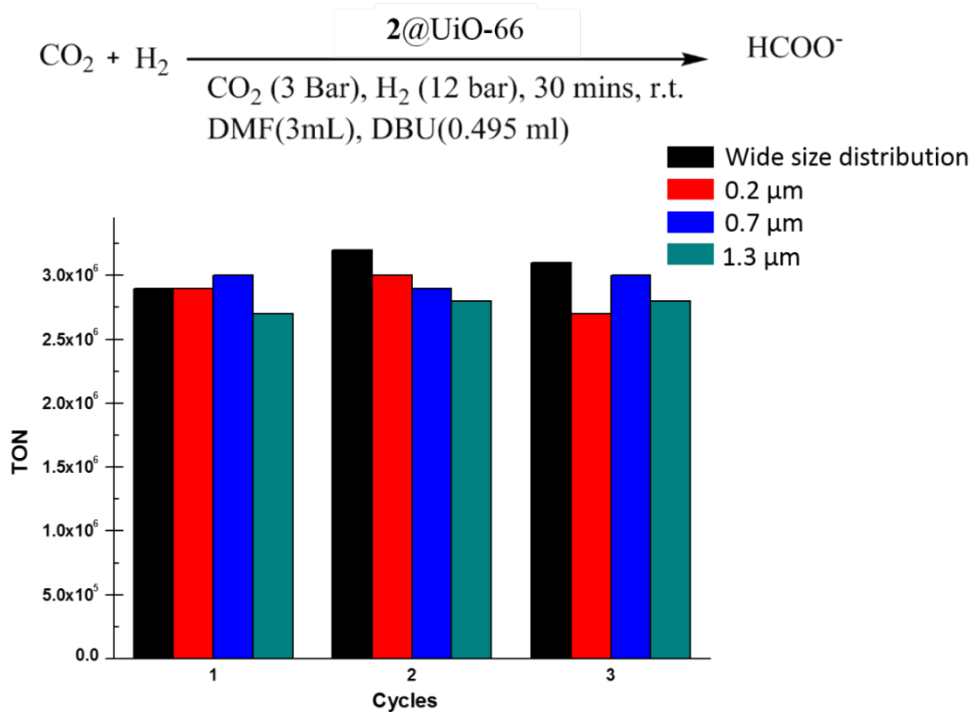

Figure 4-7. CO_2 hydrogenation reaction to formate by **2**@UiO-66 with defined size as a comparison to the previous hybrid catalyst with wide particle size distribution.

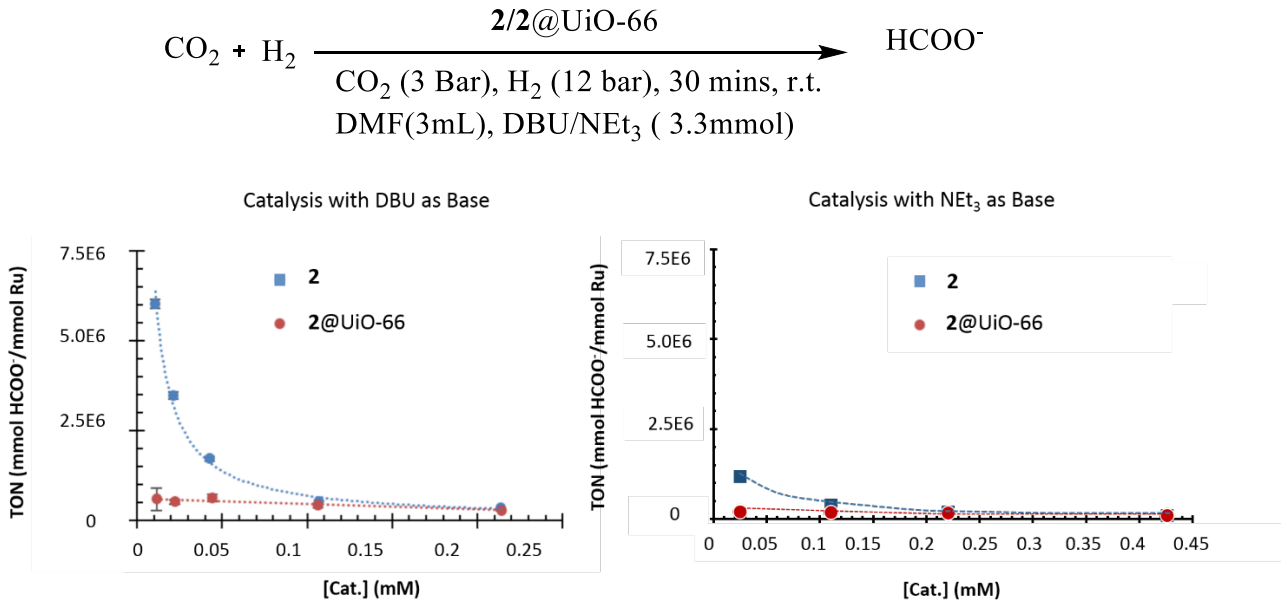

Figure 4-8. Comparison between homogeneous catalyst **1** and hybrid catalyst **1**@UiO-66 in the present of DBU and NEt_3.

4.4 Förster Resonance Energy Transfer (FRET) of C151 and R6G

To further support our hypothesis of guest distribution, Förster Resonance Energy Transfer (FRET) experiment was designed and conducted by Noella D'Souza who was my undergraduate mentee. Förster Resonance Energy Transfer (FRET), is the spatially-dependent, nonradiative energy transfer between a donor and acceptor molecule pair.[14] For FRET to occur, the molecules must be within 10-100Å of each other, and the overlap between donor emission and acceptor excitation spectra allows donor to transfer energy to the acceptor, upon the excitation of the donor.[14] In this study, FRET was used as a "molecular ruler" to determine the separation distance between a guest FRET donor, encapsulated in a host metal-organic framework (MOF), and an exogenous acceptor in solution, which sheds light on the distribution of guests in MOFs.

For this study, the fluorescent dye Coumarin 151 (C151) was chosen as a FRET donor since it's size (8.3Å) is smaller than the pore size yet larger than the aperture size of UiO-66 to prohibit guest diffusion out of the MOF.[15] Rhodamine 6G (R6G) was chosen as the FRET acceptor, since its excitation spectrum overlaps well with the emission spectrum of C151 and the guest, with a diameter of 13.7Å, is too large to diffuse into the MOF pores. Samples of C151 incorporated into the MOF via de novo and aperture-opening encapsulation were prepared and suspended in ethanol solutions with varying concentrations of Rhodamine 6G to observe the FRET efficiency.

Comparing samples of C151@UiO66 synthesized via the de novo and aperture-opening encapsulation methods support that the C151 is encapsulated close to the MOF surface with aperture-opening encapsulation. FRET was not demonstrated for the sample prepared in de novo, since only a peak at 468.9nm, corresponding to the emission of C151, was visible, and no R6G emission peak in the 560nm area (Figure 4-9a). This observation

was attributed to low loading of guest incorporation in UiO-66 through the do novo encapsulation, according to the UV-Vis measurement of the digested sample. Hence, C151@UiO-66-NO_2 was synthesized to provide a de novo encapsulation comparison with appreciable dye loading. Varying the acceptor concentration in solution for C151@UiO-66-NO_2 changes FRET efficiency most significantly when the concentration increases by an order of magnitude rather than in smaller increments (Figure 4-9b). Furthermore, the maximum acceptor emission intensity for C151@UiO66-NO_2 by de novo encapsulation is weaker than that of C151@UiO-66 by aperture-opening encapsulation, 175.324 a.u. vs. 316.805 a.u., for samples of similar donor loadings and acceptor concentration. Both observations indicate that more of the dye is encapsulated within the MOF, rather than at the surface, for C151@UiO66-NO_2 since the FRET is less receptive to smaller changes in acceptor concentration and is comparably less intense, overall, relative to that of the aperture opening sample. These findings are consistent with the spatially homogeneous incorporation of guests during de-novo encapsulation.

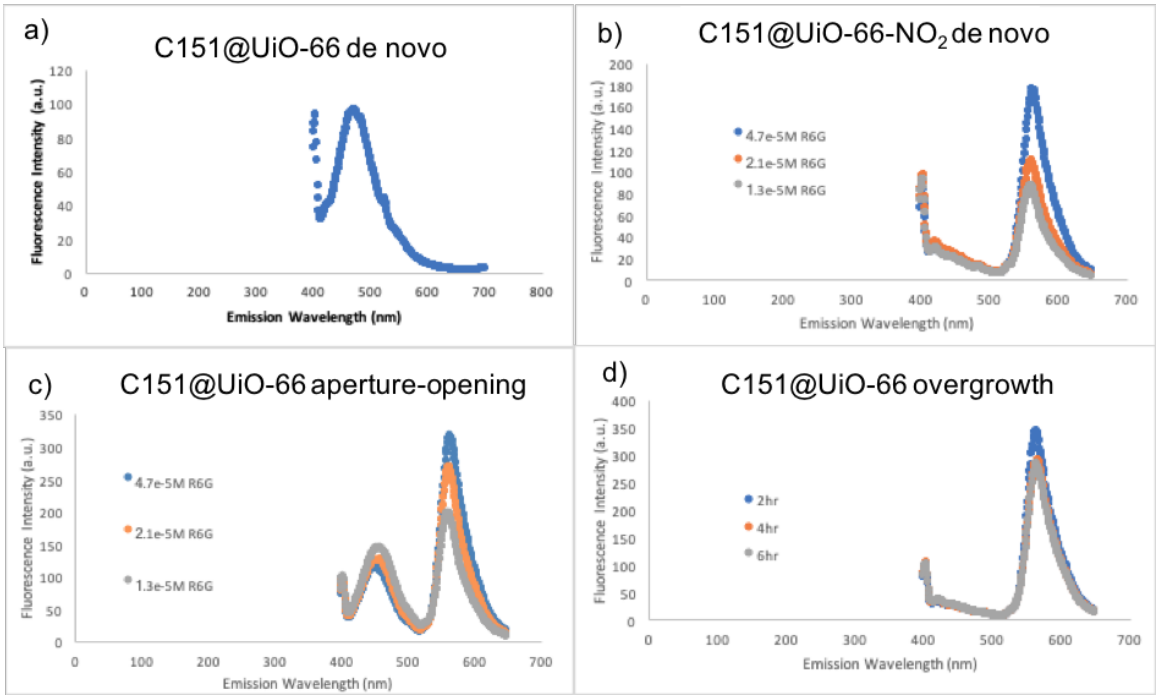

Figure 4-9. Fluorescence emission spectra at λ_{ex}=385nm for a) C151@UiO-66 through de novo, b) C151@UiO-66-NO_2 through de novo and c) C151@UiO-66 through aperture-opening encapsulation in contact with varying concentrations of exogenous R6G suspended in ethanol. d) After aperture-opening encapsulation, C151@UiO-66 overgrown with UiO-66 for 2, 4, and 6 hours suspended in 3mL of a 5.7010^{-5}M solution of R6G in ethanol.

On the other hand, FRET was observed for the sample of C151@UiO66 encapsulated via aperture-opening, as evidenced by the C151 emission peak at λ_{max}=450nm and R6G emission peak at λ_{max}=565nm (Figure 4-9c). Additionally, a smaller 66% increase in exogenous R6G concentration improves acceptor emission intensity by 35%, relative to the sample in the least concentrated solution of R6G, compared to a corresponding 25% increase in acceptor emission intensity demonstrated by the C151@UiO-66-NO_2 sample. Increased sensitivity to smaller changes in acceptor concentration is possible only if the guest molecule is encapsulated close to the MOF surface, where it is most likely to interact with exogenous R6G and undergo FRET. This supports the near-surface-encapsulation of molecular guests via the aperture-opening encapsulation method.

To further demonstrate near-surface-encapsulation via aperture-opening, samples of C151@UiO-66 prepared by aperture-opening encapsulation were added to MOF precursor solution and resubjected to UiO66 synthesis conditions for 2, 4, and 6 hours to form a MOF overgrowth on the dye encapsulated sample with different thickness of new layers. Subsequent FRET measurements on these samples displayed a general decrease in the acceptor emission intensity, relative to the C151@UiO-66 of equivalent loading (Figure 4-9d). This phenomenon can be attributed to the overgrowth layer increasing the minimum separation between donor and acceptor, which limits the extent of energy transfer in comparison to a non-overgrown sample. Furthermore, as the overgrowth period is extended, the acceptor emission intensity noticeably decreases. As the thickness of the overgrowth layer increases, the minimum separation between the donor/acceptor pair increases proportionally, which steadily decreases the ability to transfer energy to acceptor.

4.5 Summary

This chapter primarily focused on assessing the importance of mass transport for CO_2 hydrogenation catalysts encapsulated in UiO-66 and to better understand the distribution of catalysts in MOFs when the aperture-opening encapsulation method is used to encapsulate transition metal complexes in UiO-66. We proposed mass transport of formate could be responsible for the lower activity of **2**@UiO-66 compared to **2** at low catalyst loadings, due to the inherent heterogeneity of the hybrid catalyst. To test this hypothesis, **2**@UiO-66 with different UiO-66 particle sizes were synthesized. The catalytic results show there is no difference in TON, yield to formate and recyclability

between **2**@UiO-66 at size of 0.7 μm, 0.2 μm and 0.7 μm, and the hybrid catalyst with large size distribution. These observations suggest mass transport of formate is not responsible for limiting catalytic performance. Further understanding of the guests' distribution is achieved through the FRET experiment of C151@UiO-66/UiO-66. In comparison with C151@UiO-66 constructed by de novo method, FRET spectra of samples prepared by aperture-opening encapsulation demonstrate the encapsulated guests are distributed in the cages near the surface. Since the donor/acceptor interactions for the MOF host-guest system are not as precisely defined as the protein-protein interactions used in traditional biological applications of FRET, there are limitations to the accuracy of distance measurements that can be obtained. However, quantifying a certain distance range from the surface in which the guest is encapsulated can still provide relevant information for catalysis. This fact is promising for future catalyst@MOF constructs because this distribution limits contributions from mass transport and it can be used to position multiple, catalytically active subunits in close proximity with one another.

4.6 Experimental section

General Considerations Unless otherwise stated, all manipulations were carried out in air using standard analytical procedures. Catalytic carbon dioxide hydrogenation reactions were carried out in 5.0 mL ampules placed in a 450 mL stainless steel Parr reactor with stirring. Included with each reaction were positive and negative controls (using (^{tBu}PNP)Ru(CO)HCl and no catalyst, respectively) to ensure proper operation and ensure that no cross contamination between ampules occurred. To ensure that all catalyst activity in the hybrid material was coming from the encapsulated complex, a control reaction with

virgin UiO-66 was carried out, which revealed only trace amounts of formate being formed. Experiments carried out in an air-free environment were conducted under a positive pressure of N_2 using standard glovebox or Schlenk line techniques.[16] UiO-66 was synthesized as previously described. (^{tBu}PNP)Ru(CO)HCl was synthesized following a procedure adapted from the literature.[17] All [Ru]@UiO-66 catalyst employed was pre-treated as noted and subjected to serial solid dilution with UiO-66 in a mortar and pestle to achieve sufficiently low catalyst loading so that the reactions were not base-limited. [Ru]-on-UiO-66 used in catalysis was subjected to solid dilution without pre-treatment because this procedure led to complete removal of catalyst from the surface of the MOF.

Digestion of 1@UiO-66 samples Each dried solid sample (5 mg) was added to a 1.5-mL centrifugation tube. Dimethylsulfoxide (1.5 mL) was added to each sample. One drop of 15 wt% hydrofluoric acid was added to each sample, which was then left to digest overnight. Each sample was then neutralized using excess sodium bicarbonate and subjected to centrifugation.

Synthesis of UiO-66 (Large size distribution) This synthesis was adapted from the literature[15] N,N'-dimethylformamide (DMF) (25 mL) was added to a 45 mL Teflon-lined steel autoclave. Zirconium tetrachloride (241.4 mg, 1.036 mmol) and terephthalic acid (342.8 mg, 2.063 mmol) and concentrated hydrochloric acid (180 μL) was added to the autoclave, which was then sealed and heated at 220 ºC for 20 hours. The reaction mixture was then allowed to cool to room temperature and agitated to suspend the solid. This solid was isolated by centrifugation, then washed with DMF (15 mL) and left to soak in this solvent overnight. This solid was isolated again by centrifugation and washed twice with methanol (15 mL), then left to soak overnight in methanol. The solid was isolated by

centrifugation and dried in a vacuum chamber overnight, then dried overnight in an oven at 70 ºC. Powder X-Ray diffraction traces matched literature precedents.[17]

Synthesis of 1@UiO-66 In an inert atmosphere glovebox, methanol (10 mL) was added to a 20-mL crimp-sealed vial in a glovebox. UiO-66 (200 mg) and (^{tBu}PNP)Ru(CO)HCl (5.0 mg, 5.3 μmol) were added to the vial, which was then sealed. This mixture was heated at 55 ºC for five days, and then allowed to cool to room temperature. The resulting mixture was brought into a glovebox. The vial was unsealed, and the resultant mixture was transferred to a 20 mL scintillation vial and subjected to centrifugation. Trituration was achieved by decanting the supernatant from this mixture, which was set aside for NMR analysis. The remaining solid was further triturated three times with methanol (10 mL) each time using centrifugation to ensure quantitative mass transfer. After three washing cycles, 188 mg of a pale yellow solid (94%) was obtained. This solid was dried overnight in a vacuum chamber. A portion of this material (100 mg) was suspended in 15 mL of degassed DMF, and then transferred as a slurry to a 20 mL ampule containing a stir bar using a 9" glass pipet. 1,8-diazabicyclo[5.4.0]undec-7-ene (DBU) (2.465 mL, 2.505 g, 15.50 mmol) was added to this ampule. The ampule was added to a 450-mL stainless steel Parr reactor. The vessel was purged with carbon dioxide for 5 minutes and then pressurized to 42 psi. The vessel was then pressurized with hydrogen gas to achieve a total pressure of 542 psi at room temperature. The reactor was heated to 129 ºC and left to react for 45 minutes. The heating mantle was removed, the reactor was cooled using a room-temperature water bath, and the pressure was released slowly from the vessel. The vessel was opened and the ampule was removed. The reaction mixture was transferred as a slurry to a 20-mL scintillation vial and subjected to centrifugation at 3000 revolutions

per minute for 15 min, after which the supernatant was decanted. The solid was triturated twice with methanol (20 mL) followed by centrifugation and dried overnight in a vacuum chamber to give a pale yellow powder (93 mg, 93%). The loading of catalyst in the MOF was determined by ICP-OES (see "Preparation of (^{tBu}PNP)Ru(CO)HCl stock solutions" and "Digestion of UiO-66 for ICP-OES analysis", below).

Preparation of (^{tBu}PNP)Ru(CO)HCl stock solutions (^{tBu}PNP)Ru(CO)HCl (5.0 mg, 5.3 μmol) was added to a 20 mL scintillation vial. Degassed N,N'-dimethylformamide (DMF) (3.0 mL) was added to this vial. From this solution, 1.0 mL was extracted and diluted to 5.0 mL in a class A 10-mL volumetric flask using DMF. Further serial dilution was achieved by removing 1.0 mL of this solution and diluting to 10 mL in a class A 10-mL volumetric flask. The catalytic solution (0.033 μM) was transferred to a 20-mL scintillation vial, sealed, and stored at -40 ºC in a glovebox. Solutions were allowed to warm to room temperature before use in catalysis.

General Procedure for the hydrogenation of carbon dioxide For homogeneous catalysis, a stock solution (3.0 mL) of (^{tBu}PNP)Ru(CO)HCl in DMF was prepared as previously noted and added to a 5.0-mL ampule using a 9" glass pipet. For the heterogeneous catalyst, unless otherwise noted, the solid was suspended in 3 mL of degassed DMF, and then transferred as a slurry to 5-mL ampules using a 9" glass pipet. 1,8-diazabicyclo[5.4.0]undec-7-ene (DBU) (0.493 mL, 0.501 g, 3.30 mmol) was added to each ampule with a stir bar. These ampules were arranged in a 450 mL stainless steel Parr reactor that contained a thermocouple to ensure thermostated reactions. The vessel was placed on a Parr instrument stand atop a stir plate and surrounded by a heating mantle. The reaction vessel was purged with carbon dioxide for 5 minutes and then pressurized to 42

psi. The vessel was pressurized with hydrogen to a total pressure of 212 psi, and the reactions were allowed to react at room temperature for 30 minutes. Upon conclusion of the reaction, the heating mantle was removed and the pressure was released slowly from the vessel. The vessel was opened and the ampules were removed. The colorless slurry obtained from reactions involving heterogeneous catalysis were transferred to 20 mL scintillation vials and subjected to centrifugation, after which the supernatant was decanted. The homogeneous reactions were removed from the ampoules and the supernatant was analyzed as described below without further manipulation. A 0.25 mL aliquot of the supernatant was removed and combined with benzene (0.01 mL) and D_2O (0.45 mL) in 4.0-mL vials. These mixtures were then transferred to individual NMR tubes and quantitative ^1H NMR was used to determine the yield of formate by integration of the formate peak in reference to benzene.

Digestion of UiO-66 for ICP-OES analysis Solid MOF material (5.00 mg) was weight out into a 1.5 mL Teflon vial. DMSO (300 μL) and 1 drop of 15 wt.% aqueous hydrofluoric acid solution were added in sequence. The mixture was sonicated for 1 minute and left to digest for 1 hour. The digested samples then heated to approximately 150 °C overnight in a sand bath open to the air to remove solvent. The resulting solid was dissolved and transferred to a 20 mL glass scintillation vial using a mixture (10% v/v) of hydrochloric acid in deionized water (300 μL). Each sample was diluted with additional deionized water (3.7 mL) and analyzed by ICP-OES.

ICP-OES Standard preparation Four standards were prepared by dilution from commercially available zirconium (999 ± 5 ppm), ruthenium (999 ± 5 ppm), and phosphorus (100.04 ± 0.55 ppm) standards using serial dilution in grade A volumetric

glassware to cover the expected concentration ranges. The standards were then employed in a calibration curve to determine the loading of catalyst in a tested solid. These standards consisted of Zr/Ru/P concentrations in ppm at the proportions: 250/5/5, 150/2/2, 25/0.5/0.5, 2.5/0.05/0.05

Procedure for carbon dioxide hydrogenation recycling studies using 1@UiO-66 Carbon dioxide hydrogenation was carried out using the "general procedure for carbon dioxide hydrogenation" at 5x scale in a 20-mL ampule. The solid was washed twice with methanol (20 mL) and dried overnight in a vacuum chamber between cycles.

Synthesis of UiO-66 with different sizes (0.2 um, 0.7 um) This synthesis was adapted from the literature.[18] $ZrCl_4$ (4 mM) and BDC (4 mM) were dissolved in 140 ml DMF containing acetic acid (2.4 M) in a glass vial. Afterwards, different amount of NEt_3 (0 M, 0.001 M, 0.004 M, 0.008 M) was added to the solution. Than the vial was heated in an oven at 120 ^oC for 6 hours. After the sample was cooled to room temperature, the product was collected by centrifugation, washed three times with DMF and three times with methanol, and then soaked in methanol for three days with replacing the soaking solvent every 12 hours to exchange DMF. The solid was isolated by centrifugation and dried in a vacuum chamber overnight, then dried overnight in an oven at 70 ºC. The yields were around 50% for all reactions, even while varying the amount of NEt_3. The products were characterized by powder X-ray diffraction (PXRD) to confirm their crystallinity and scanning electron microscope (SEM) to generate their size distribution, counting at least 100 particles.

Synthesis of UiO-66 with 1.3 um particle size $ZrCl_4$ (4 mM) and BDC (4 mM) were dissolved in 20 ml DMF containing 3.5 mmol benzoic acid in a glass vial. Afterwards,

different amount of acetic acid (0.85 M, 1.3 M, 1.7 M, 2.2 M) was added to the solution. Than the vial was heated in an oven at 120 ^{o}C for 24 hours. After the sample was cooled to room temperature, the product was collected by centrifugation, washed three times with DMF and three times with methanol, and then soaked in methanol for three days with replacing the soaking solvent every 12 hours to exchange DMF. The solid was isolated by centrifugation and dried in a vacuum chamber overnight, then dried overnight in an oven at 70 ºC. The yields are around 30% for all reactions, even while varying the amount of acetic acid. The products were characterized by powder X-ray diffraction (PXRD) to confirm their crystallinity and scanning electron microscope (SEM) to generate their size distribution, counting at least 100 particles.

Reference

1. de Vries, J. G.; Jackson, S. D., *"Homogeneous and heterogeneous catalysis in industry."* Catalysis Science & Technology **2012**, 2 (10), 2009-2009.

2. Huang, W.; Kuhn, J. N.; Tsung, C.-K.; Zhang, Y.; Habas, S. E.; Yang, P.; Somorjai, G. A., *"Dendrimer Templated Synthesis of One Nanometer Rh and Pt Particles Supported on Mesoporous Silica: Catalytic Activity for Ethylene and Pyrrole Hydrogenation."* Nano Letters **2008**, 8 (7), 2027-2034.

3. Weckhuysen, B. M.; Keller, D. E., *"Chemistry, spectroscopy and the role of supported vanadium oxides in heterogeneous catalysis."* Catalysis Today **2003**, 78 (1), 25-46.

4. Choi, S.-W.; Kim, W.-G.; So, J.-S.; Moore, J. S.; Liu, Y.; Dixit, R. S.; Pendergast, J. G.; Sievers, C.; Sholl, D. S.; Nair, S.; Jones, C. W., *"Propane dehydrogenation catalyzed by gallosilicate MFI zeolites with perturbed acidity."* Journal of Catalysis **2017**, 345, 113-123.

5. Liu, Y.; Tang, Z., *"Multifunctional Nanoparticle@MOF Core–Shell Nanostructures."* Advanced Materials **2013**, 25 (40), 5819-5825.

6. An, B.; Zeng, L.; Jia, M.; Li, Z.; Lin, Z.; Song, Y.; Zhou, Y.; Cheng, J.; Wang, C.; Lin, W., *"Molecular Iridium Complexes in Metal–Organic Frameworks Catalyze CO2 Hydrogenation via Concerted Proton and Hydride Transfer."* Journal of the American Chemical Society **2017**, 139 (49), 17747-17750.

7. Karagiaridi, O.; Lalonde, M. B.; Bury, W.; Sarjeant, A. A.; Farha, O. K.; Hupp, J. T., *"Opening ZIF-8: A Catalytically Active Zeolitic Imidazolate Framework of Sodalite Topology with Unsubstituted Linkers."* Journal of the American Chemical Society **2012**, 134 (45), 18790-18796.

8. Zhao, M.; Yuan, K.; Wang, Y.; Li, G.; Guo, J.; Gu, L.; Hu, W.; Zhao, H.; Tang, Z., *"Metal–organic frameworks as selectivity regulators for hydrogenation reactions."* Nature **2016**, 539, 76-78.

9. Li, Z.; Rayder, T. M.; Luo, L.; Byers, J. A.; Tsung, C.-K., *"Aperture-Opening Encapsulation of a Transition Metal Catalyst in a Metal–Organic Framework for CO2 Hydrogenation."* Journal of the American Chemical Society **2018**, 140 (26), 8082-8085.

10. Weckhuysen, B. M., *"Solid catalysts under the spotlight."* Nature Catalysis **2018**, 1 (2), 101-102.

11. Pham, M.-H.; Vuong, G.-T.; Fontaine, F.-G.; Do, T.-O., *"Rational Synthesis of Metal–Organic Framework Nanocubes and Nanosheets Using Selective Modulators and Their Morphology-Dependent Gas-Sorption Properties."* Crystal Growth & Design **2012**, 12 (6), 3091-3095.

12. Vermoortele, F.; Bueken, B.; Le Bars, G.; Van de Voorde, B.; Vandichel, M.; Houthoofd, K.; Vimont, A.; Daturi, M.; Waroquier, M.; Van Speybroeck, V.; Kirschhock, C.; De Vos, D. E., *"Synthesis Modulation as a Tool To Increase the Catalytic Activity of Metal–Organic Frameworks: The Unique Case of UiO-66(Zr)."* Journal of the American Chemical Society **2013**, 135 (31), 11465-11468.

13. Han, Y.; Liu, M.; Li, K.; Zuo, Y.; Wei, Y.; Xu, S.; Zhang, G.; Song, C.; Zhang, Z.; Guo, X., *"Facile synthesis of morphology and size-controlled zirconium metal–organic framework UiO-66: the role of hydrofluoric acid in crystallization."* CrystEngComm **2015**, 17 (33), 6434-6440.

14. Jang, S.; Newton, M. D.; Silbey, R. J., *"Multichromophoric F\"orster Resonance Energy Transfer."* Physical Review Letters **2004**, 92 (21), 218301-218305.

15. Neugebauer, J.; Jacob, C. R.; Wesolowski, T. A.; Baerends, E. J., *"An Explicit Quantum Chemical Method for Modeling Large Solvation Shells Applied to Aminocoumarin C151."* The Journal of Physical Chemistry A **2005**, 109 (34), 7805-7814.

16. Burger, B. J.; Bercaw, J. E., *"Vacuum Line Techniques for Handling Air-Sensitive Organometallic Compounds."* In Experimental Organometallic Chemistry, ACS Symposium Series **1987**; 357,79-115.

17. Shearer, G. C.; Chavan, S.; Ethiraj, J.; Vitillo, J. G.; Svelle, S.; Olsbye, U.; Lamberti, C.; Bordiga, S.; Lillerud, K. P., *"Tuned to Perfection: Ironing Out the Defects in Metal–Organic Framework UiO-66."* Chem. Mater. **2014**, 26 (14), 4068-4071.

18. Zhao, Y.; Zhang, Q.; Li, Y.; Zhang, R.; Lu, G., *"Large-Scale Synthesis of Monodisperse UiO-66 Crystals with Tunable Sizes and Missing Linker Defects via Acid/Base Co-Modulation."* ACS Applied Materials & Interfaces **2017**, 9 (17), 15079-15085.

Chapter 5. Understanding Non-covalent Interactions in a Host-guest System

5.1 Outer sphere interactions in a host-guest system

Historically, pure inorganic porous materials such as zeolites,[1] supramolecular cages,[2] and tetrahedral inorganic cages[3] have been explored as host materials. These host materials are capable of immobilizing large libraries of transition metal complexes, however, they are often limited by structural tunability or sophisticated material characterization (See Chapter 1), and systematic investigations of outer sphere interactions are uncommon in those host-guest systems.

Recently, researchers have tested the photodynamic behaviors of incorporated chromophores in MOFs and observed the effect of spatial-confining characteristics of the porous materials on the photophysical behavior of the chromophores.[4] The inherent sensitivity of this approach is powerful in revealing the dye molecule's orientation and energy migration properties when confined in the host matrix. However, few reports have detailed a systematic investigation to correlate chromophore-MOF non-covalent interactions and the properties of differently substituted linkers.[5] Because non-covalent interactions can be highly influenced by the subtle changes of functional groups, we have interrogated chromophore-MOF interactions by systematically installing substitutions on linkers, where the substitutes on linkers are not interfering with the MOF structure.

UiO-66, consisting of Zr-oxo cluster nodes and terephthalic acid linkers, is one of the most chemically and thermally robust MOFs reported.[6] In addition, modifications to UiO-66 are easily achievable by two methods: direct synthesis of analogs[6] and post-synthetic linker exchange reactions.[7] In Chapter 2 and 3, our group has developed a method

called “aperture-opening encapsulation” that allows molecules larger than its aperture size of the MOF but smaller than the cavity size to be encapsulated in the cavity without relying on covalent bonds to anchor the guest to the host.[8] Herein, we report the encapsulation of a weakly solvatochromic dye, Rhodamine 6G into a series of functionalized UiO-66 derivatives using the “aperture-opening encapsulation” method. Rhodamine dyes were identified as a promising probe due to high quantum yield, strong absorption, and emission in the visible (500-600 nm) range.[9] Outer sphere interactions between the dye and the guest were evaluated by monitoring the absorption and fluorescent properties of the dye. Further, Kamlet-Abboud-Taft solvation energy relationships and linear free energy relationships were used to reveal a sophisticated and synergistic relationship between the solvent and the substituent installed on the terephthalic aicd linkers, both of which modulate the local environment in the cavity of the MOF in ways that are more significant than observed for R6G in solution.

5.2 The photophysical behavior of UiO-66 encapsulated Rhodamine 6G

To probe host-guest interactions in the chromophore-MOF system, Rhodamine 6G (R6G) was encapsulated in UiO-66 using the aperture-opening encapsulation described in Chapter 2.[8b] The encapsulated Rhodamine 6G's photophysical behavior was analyzed by ultraviolet-visible spectroscopy in an array of solvents: CH_2Cl_2, MeOH, H_2O, acetone, n-butanol, ethanol, 1-hexanol, 1-heptanol, DMF, dioxane and DMSO, which covers a large spectrum of solvent properties. The magnitude of the bathochromic shift in the emission λ_{max} of the encapsulated dye was greater than the free Rhodamine 6G dye molecules in the same solvent. For example, R6G@UiO-66 (564 nm) exhibited a 10 nm bathochromic shift from free Rhodamine 6G (554 nm) in 1-hexanol (Figure 5-1a). Rhodamine 6G dye has

been reported to be weakly solvatochromatic,[1] which is consistent with our observation (Figure 5-1b). In the chosen solvents, the emission λ_{max} of homogenous Rhodamine 6G spanned 22 nm from CH_2Cl_2 (539 nm) to DMSO (561 nm) (Figure 5-1b). Unlike any other solvent evaluated, the emission λ_{max} of free Rhodamine 6G in CH_2Cl_2 (539 nm) was significantly hypsochromic shifted compared to the rest of solvents.

Compared to free Rhodamine 6G, the UiO-66-encapsulated dyes molecules exhibited a bathochromic shift in emission for most solvents employed. The emission λ_{max} for free Rhodamine 6G was in the order of CH_2Cl_2, MeOH, H_2O, acetone, n-butanol, ethanol, 1-hexanol, 1-heptanol, DMF, dioxane, DMSO, and that for UiO-66 encapsulated Rhodamine 6G is MeOH, H_2O, dioxane, CH_2Cl_2, n-butanol, 1-hexanol, ethanol, 1-heptanol, acetone, DMSO, DMF. For example, the emission λ_{max} for free Rhodamine 6G was in the range from 539 nm (CH_2Cl_2) to 561 nm (DMSO), and R6G@UiO-66 emitted from 556 nm (MeOH) to 569 nm (DMF) (Figure 5-1b). Although R6G@UiO-66 exhibited a greater bathochromic shift in most solvents, there was no particular trend in shift based on solvent. Despite the overall bathochromic shift of the encapsulated Rhodamine 6G, there was no obvious correlation between the amount that dye's fluorescence was shifted and solvent properties, such as dielectric, hydrogen bonding capabilities, etc. (vide supra) One notable observation was that some solvents led to more significant shifts than others such as DMSO and dioxane. This observation indicates that the bathochromic shifts are a consequence of more than just dye encapsulation and that the local environment of the dye is significantly affected by the encapsulation.

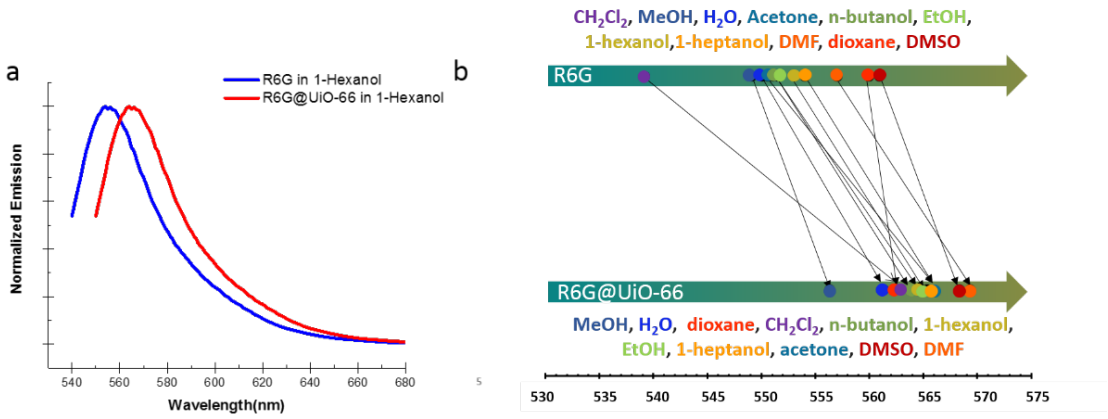

Figure 5-1. The Emission spectra of Rhodamine 6G and R6G@UiO-66 (a) in 1-Hexanol, (b) in solvent array: Top: CH_2Cl_2, MeOH, H_2O, acetone, n-butanol, ethanol, 1-hexanol, 1-heptanol, DMF, dioxane, DMSO; Bottom: methanol, H2O, dioxane, CH_2Cl_2, n-butanol, 1-hexanol, ethanol, 1-heptanol, acetone, DMSO, DMF.

To test whether the difference in R6G fluorescence originated from encapsualting the dye in the MOF as oppsoed to being a consequence of the dye being adsorbed to the surface of the MOF, a control experiment was carried out in which a physical mixture of Rhodamine 6G and MOF was prepared. No bathochromic shift was observed in the emission spectra (Figure 5-2a). This observation demonstrated that the change of photophysical behavior of Rhodamine 6G was caused by the dye molecule encapsulated in the MOF cavity.

To test whether possibilities other than encapsulation could contribute to the bathchromic shift in emission spectra, absorption spectra were taken for free Rhodamine 6G and encapsulated Rhodamine 6G dissolved/suspended in water (Figure 5-2b). Two bands in the absorption profile of free R6G were observed, and in sharp contrast, only one absorption band was observed in R6G@UiO-66 in water. Rhodamine 6G in known to dimerize in the aqueous solvent and this phenominon is particularly problematic at high-

concentrations where dye aggregation is likely.[10] For instance, Rhodamine 6G is known to form dimers and aggregates in aqueous solution at high concentrations, which leads to bathochromic emission shifts or even quenching.[11] Two types of dimers are common, where two dye molecules in the dimer structure in parallel is referred to as H-dimer, and J-dimer are two molecules in orthogonal. Here, two absorption bands observed for free Rodamine 6G in water have been attributed to the H- and J-dimers as a result of dye aggregation.[11] Rhodamine 6G is of similar size (13 Å) to the octahedral cavity size of UiO-66 (12 Å), meaning that hypothetically only one molecule can fit in each cage. The observation that only one absorption band was observed in R6G@UiO-66 indicates that the dye molecule does not exist as a dimer even though the spectrum was collected in water and at concentrations where dye aggregation is known to occur for R6G dissolved in water. This finding strongly supports the encapsulation of R6G in the pores of UiO-66 rather than being supported on the surface of UiO-66. Thus, the observed change in the photophysical properties of Rhodamine 6G is most likely a consequence of dye molecules being confined in the cage rather than surface supported dye-dye interactions.

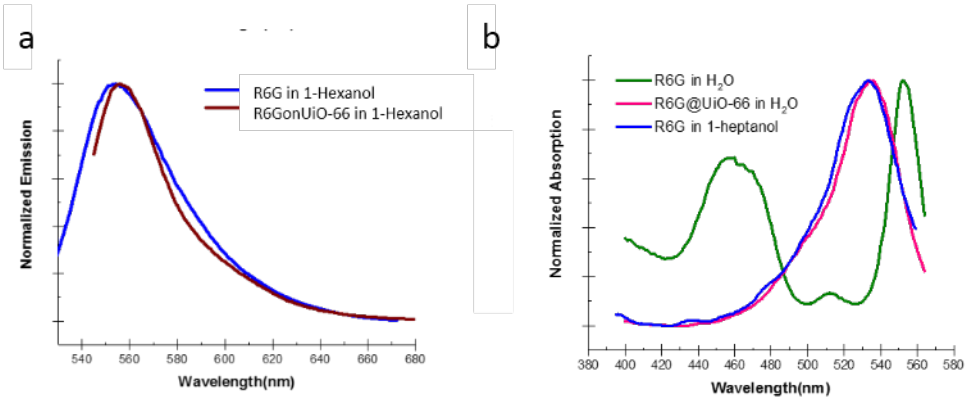

Figure 5-2. The Emission spectra of (a) physical mixture of Rhodamine 6G with UiO-66 in 1-hexanol. (b) Absorption spectra of R6G, R6G@UiO-66in water and R6G in 1-heptanol.

To investigate whether the interactions is depenent on the distance between the host and guest, Rhodamine 6G was encapsulated in UiO-67, a MOF with larger pore sizes than UiO-66. UiO-67 has the same topology with UiO-66, yet it consists of biphenyl-4,4'-dicarboxylate linkers rather than terephthalic acid. A diminished bathochromic shift in emission λ_{max} was observed in R6G@UiO-67 compared to R6G@UiO-66 in 1-hexanol (Figure 5-3a). Moreover, compared to free Rhodamine 6G, R6G@UiO-67 exhibited less significant bathochromic shifts in the array of solvents studied ranging from acetone (555 nm) to dioxane (560 nm). Based on these comparisons, we concluded that the observed behavior resulted from the dye being constrained in the cage environment played a role in the chromophore-solvent interaction. Although, it is still not clear why dichloromethane displays significant bathochromic shifts when R6G is encapsulated in UiO-66 or UiO-67.

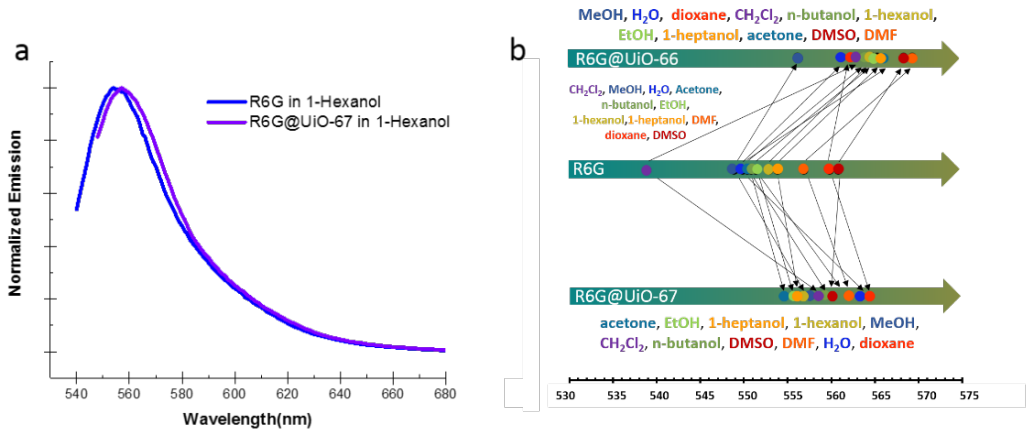

Figure 5-3. The emission spectra of Rhodamine 6G and R6G@UiO-67 (a) in 1-hexanol, (b) in solvent array: Bottom: acetone, ethanol, 1-heptanol, 1-hexanol, MeOH, CH_2Cl_2, n-butanol, DMSO, DMF, H_2O, dioxane.

5.3 The photophysical behavior of UiO-67 and UiO-66-OMe encapsulated Rhodamine 6G

We postulated that the photophysical properties of Rhodamine 6G could be further tuned by introducing structurally-inert substitutions on the organic bridging linker of the MOF. UiO-66-OMe, which features 2-methoxyterephthalic acid as the organic linker,[12] was chosen as a host candidate to evaluate this hypothesis. Installing a methoxide substitute on the terephthalic acid linker introduces significant steric bulk and significantly alters the electronic characteristics of the linker. The installed functionalities are expected to interact with entrapped solvent molecules differently compared to the unfunctionalized terephthalic acid linkers in UiO-66.

We observed the emission spectra of R6G@UiO-66-OMe exhibited a significant amplification of the observed bathochromic shift. For instance, the emission λ_{max} of R6G@UiO-66-OMe (570 nm) was shifted 6 nm further than that of R6G@UiO-66 (564 nm), and 16 nm further than that of free R6G (554 nm) in 1-hexanol. (Figure 5-2c) More importantly, the solvatochromic behavior of Rhodamine 6G was significantly amplified when being encapsulated in UiO-66-OMe. The λ_{max} range of R6G@UiO-66-OMe spanned up to 36 nm from 553 nm (ethanol) to 589 nm (dioxane), which is 23 nm larger than that of R6G@UiO-66. The higher sensitivity of R6G@UiO-66-OMe to solvent polarity could be attributed to the confinement and electronic and steric influences from the –OMe group.

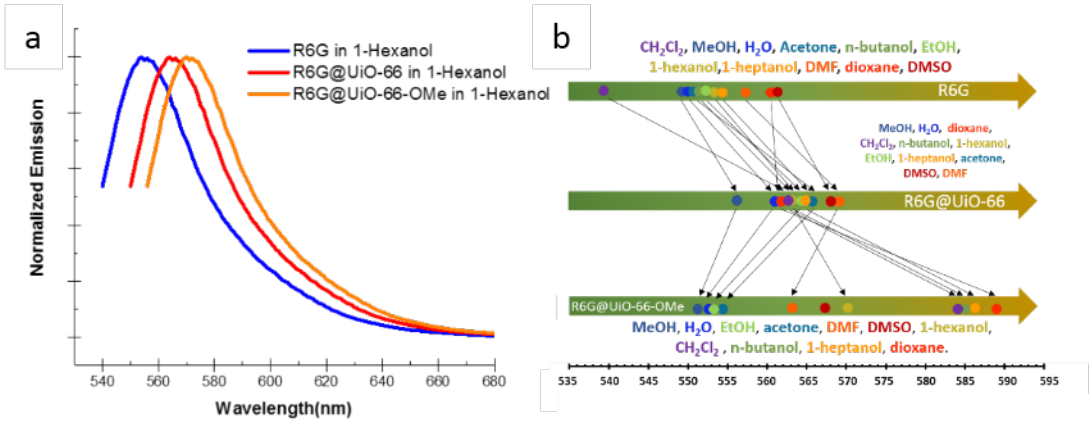

Figure 5-4. The Emission spectra of Rhodamine 6G, R6G@UiO-66 and R6G@UiO-66-OMe (a) in 1-hexanol, (b) in solvent array: Top: CH_2Cl_2, MeOH, H_2O, acetone, n-butanol, ethanol, 1-hexanol, 1-heptanol, DMF, dioxane, DMSO; middle: MeOH, H_2O, Dioxane, CH_2Cl_2, n-butanol, 1-hexanol, ethanol, 1-heptanol, acetone, DMSO, DMF. Bottom: MeOH, H_2O, ethanol, acetone, DMF, DMSO, 1-hexanol, CH_2Cl_2, n-butanol, 1-heptanol, dioxane.

5.4 Systematic change of substitutes on MOF linker

After demonstrating the impact of -OMe on the MOF backbone to the solvatochromic behavior of the dye, next, we investigated the effect of systematic changes of functional groups in UiO-66 on solvent stabilization of the excited state of Rhodamine 6G. Doing so requires analyzing the emission λ_{max} of various R6G@UiO-66-X derivatives in the same solvent.

In addition to UiO-66-OMe, a library of UiO-66 variants UiO-66-X (X=H, Br, Cl, NH_2, NO_2, Me, I) was synthesized by literature protocols.[6,15] Rhodamine 6G was encapsulated through an aperture-opening encapsulation method identical to that for UiO-66, UiO-67, and UiO-66-OMe, and the absorption and emission λ_{max} of R6G@UiO-66-X were measured in an array of solvents (Table 5-1).

Table 5-1. The absorption λ_{max}, emission λ_{max} and Stokes shift of free Rhodamine 6G and R6G@UiO-66-X (X=H, Br, NH_2, NO_2, Cl, OMe, Me, I).

a)

Absorption	R6G	R6G@UiO-66-Br	R6G@UiO-66-NH_2	R6G@UiO-66-NO_2	R6G@UiO-66	R6G@UiO-66-Cl	R6G@UiO-66-OMe	R6G@UiO-66-Me	R6G@UiO-66-I
Protic solvents									
H_20	525	539	528	524	532	522	528	545	526
MeOH	527	541	532	532	535	524	527	553	525
nButanol	531	540	538	535	536	532	533	541	533
1-heptanol	533	539	542	537	536	538	533	540	535
1-hexanol	532	538	541	536	538	538	532	542	537
Ethanol	533	544	536	533	537	529	531	548	533
Aprotic solvents									
DMSO	539	538	546	540	541	542	534	552	541
DMF	535	541	540	538	541	533	536	546	539
Dioxane	539	540	554	534	537	537	537	546	529
CH_2Cl_2	521	537	545	525	533	535	529	542	521
Acetone	528	539	533	531	538	530	529	548	525

b)

Florescence	R6G	R6G@UiO-66-Br	R6G@UiO-66-NH_2	R6G@UiO-66-NO_2	R6G@UiO-66	R6G@UiO-66-Cl	R6G@UiO-66-OMe	R6G@UiO-66-Me	R6G@UiO-66-I
Protic solvents									
H_2O	550	573	553	557	561	573	553	575	569
MeOH	549	579	550	560	556	574	551	582	560
nButanol	551	574	556	563	564	579	585	574	560
1-heptanol	554	579	555	561	565	581	586	571	565
1-hexanol	553	579	555	562	564	578	570	570	562
Ethanol	551	580	552	564	564	579	553	576	561
Aprotic solvents									
DMSO	561	578	564	567	568	577	567	575	567
DMF	557	579	559	568	569	578	563	571	565
Dioxane	560	577	566	563	562	586	589	575	542
CH_2Cl_2	539	570	555	560	562	583	584	571	542
Acetone	550	578	551	565	565	585	554	579	562

c)

Stokes shift	R6G	R6G@UiO-66-Br	R6G@UiO-66-NH_2	R6G@UiO-66-NO_2	R6G@UiO-66	R6G@UiO-66-Cl	R6G@UiO-66-OMe	R6G@UiO-66-Me	R6G@UiO-66-I
Protic solvents									
H_20	25	34	25	33	29	51	25	30	43
MeOH	22	38	18	28	21	50	24	29	35
nButanol	20	34	18	28	28	47	52	33	27
1-heptanol	21	40	13	24	29	43	53	31	30
1-hexanol	21	41	14	26	26	40	38	28	25
Ethanol	18	36	16	31	27	50	22	28	28
Aprotic solvents									
DMSO	22	40	18	27	27	35	33	23	26
DMF	22	38	19	30	28	45	27	25	26
Dioxane	21	37	12	29	25	49	52	29	13
CH_2Cl_2	18	33	10	35	29	48	55	29	21
Acetone	22	39	18	34	27	55	25	31	37

In a single solvent, the emission profiles of R6G@UiO-66-X changed significantly with change to the MOF linker functionality (Figure 5-5). In particular, the emission λ_{max} of R6G@UiO-66-OMe (586 nm) and R6G@UiO-66-Cl (581 nm) in 1-heptanol exhibited bathochromic shifts of 32 nm (5.7%) and 27 nm (4.9 %) compared to free Rhodamine 6G, respectively (Figure 5-5a). The magnitude of the shifts observed is remarkable, considering that Rhodamine 6G has limited solvatochromism in the array of solvents investigated. The large bathochromic shifts observed by changing the functionality in the MOF suggest that non-covalent host-guest interactions have a stronger impact on the excited state of the guest when it is constrained in the solid matrix with solvent compared to when the unencapsulated guest molecule is surrounded by freely moving solvent molecules. In other words, changing the substitutes on the linker from hydrogen to methoxide has a much larger impact on the local environment in which the dye resides than does changing the

solvent from methanol to hexane. In addition, the degree of the enhancement was dependent on the sterics and electronics of the substitutions.

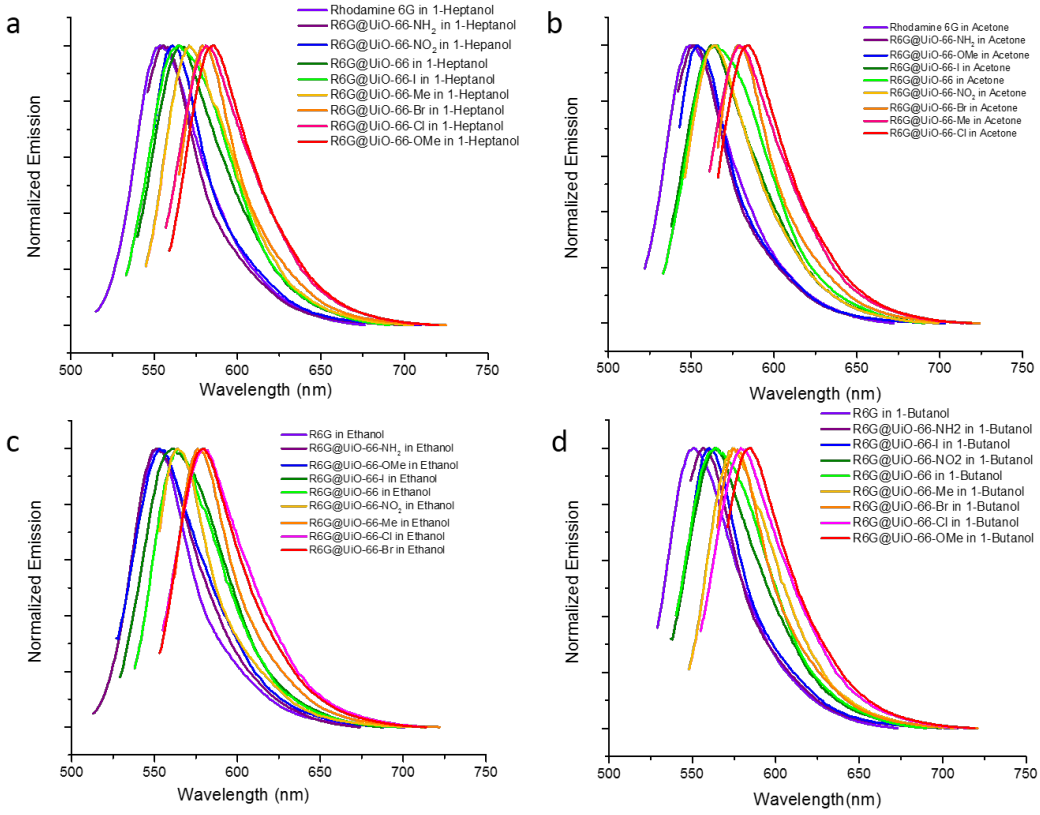

Figure 5-5. The Emission spectra of R6G@UiO-66-X in (a) 1-heptanol, (b) acetone, (c) ethanol, (d) n-butanol.

Rhodamine 6G was encapsulated into functionalized UiO-67-X (X: NO_2, NH_2, Br) as well. Consistent with the hypothesis that confinement of the dye is necessary to amplify solvent/solute interactions, the emission maximum of Rhodamine 6G was less sensitive to changes in a host with a larger pore size (Table 5-2).

Table 5-2. The emission λ_{max} of R6G@UiO-67-X (X=H, Br, NO_2, NH_2), and the graphical presentation.

Fluorescence	R6G@UiO-67	R6G@UiO-67-Br	R6G@UiO-67-NO_2	R6G@UiO-67-NH_2
Protic solvents				
H_2O	564	561	559	555
MeOH	558	554	551	550
nButanol	561	564	562	552
1-Heptanol	556	561	559	557
1-Hexanol	557	562	562	555
Ethanol	555	560	560	552
Aprotic solvents				
DMSO	562	565	566	561
DMF	563	562	568	557
Dioxane	564	566	562	555
CH_2Cl_2	560	564	560	551
Acetone	555	558	560	554

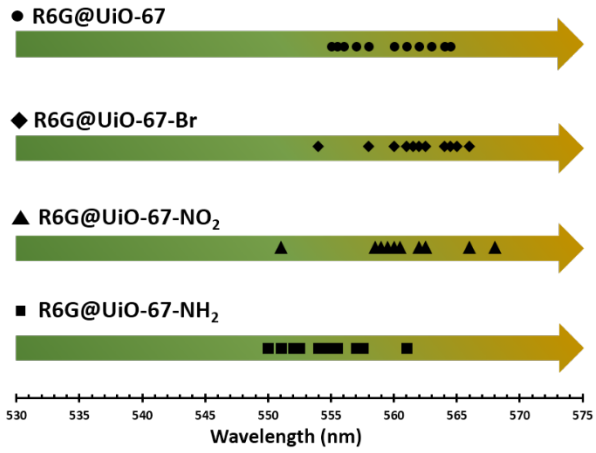

5.5 Linear solvation energy relationship

Having demonstrated the amplification of solvatochromism due to substitutions on the MOF linker, we explored the linear solvation energy relationships in the form of Kamlet-Abboud equation to analyze the effect of solvent properties on the spectral features of Rhodamine 6G.

The linear solvation energy relationship is a powerful model to correlate solvent properties with the photophysical behavior of chromophores.[13] Solvatochromic behavior of xanthene dyes results from various solute-solvent interactions in a given medium.[14] In principle, there are two categories of solute-solvent interactions: non-specific interactions, such as the enhancement of dipole moment, and specific interactions, such as hydrogen bonding. The parameters governing the contribution of solvent parameters upon spectral shifts regarding specific and non-specific interactions have been evaluated using the Kamlet-Abboud-Taft equation. (Eq. 1) [13]

$$(V_a-V_f)=(V_a-V_f)_0 + a\alpha + b\beta + s\pi^* \qquad \text{Eq. 1}$$

In this model, π* is the measurement of the solvent polarizability, α is the scale of the solvent hydrogen bond donor ability (HBD) and β is the scale of the solvent hydrogen bond acceptor ability (HBA). (Table 5-3) V_a is the absorption energy and V_f is the emission energy. The value of $(V_a-V_f)_0$ is obtained from linear regression fitting and is related to the energy loss from the Stokes shift. The coefficients (a, b and s) are weighted, suggesting which interaction plays the major role.

Table 5-3. α, β and π* values of the listed solvents.

Parameters	α	β	Π*
Protic solvents			
H_2O	1.17	0.47	1.09
MeoH	0.98	0.66	0.60
nButanol	0.84	0.84	0.47
Dioxane	0	0.37	0.49
1-Heptanol	0.64	0.96	0.39
1-Hexanol	0.67	0.94	0.40
Ethanol	0.86	0.75	0.54
Aprotic solvents			
DMSO	0	0.76	1.00
DMF	0	0.69	0.88
Dioxane	0	0.37	0.49
CH_2Cl_2	0.13	0.1	0.73
Acetone	0.08	0.48	0.62

First, the Kamlet-Abboud-Taft equation was applied to the UV-Vis data for all solvents for absorption, emission, and the Stokes shift of Rhodamine 6G, R6G@UiO-66,

and R6G@UiO-66-OMe. R6G, R6G@UiO-66, and R6G@UiO-67 exhibited a poor correlation between the spectra and the employed solvent properties. Although satisfactory fits could not be obtained when considering all the solvents in the study, decent fits to the data could be obtained by separating the solvents into protic and aprotic solvents. In this case, absorption and emission features exhibited good correlation with solvent properties. The Stokes shift, defined as the energy difference between absorption energy and emission energy, correlated to the relative change of energy between ground and excited states. By fitting the Stokes shift data, the effect that the solvent has on the ground state and excited state is manifested in a single number (Figure 5-6).

Entry	Protic solvents					Aprotic solvents			
	V_a-V_f	a	b	s	R^2	V_a-V_f	b	s	R^2
R6G	231	249	601	479	0.98	664	334	-186	0.99
R6G@UiO-66	1418	490	1756	910	0.81	770	-80	190	0.88
R6G@UiO-66-OMe	16418	7712	12629	2126	0.91	2215	-3110	1118	0.95

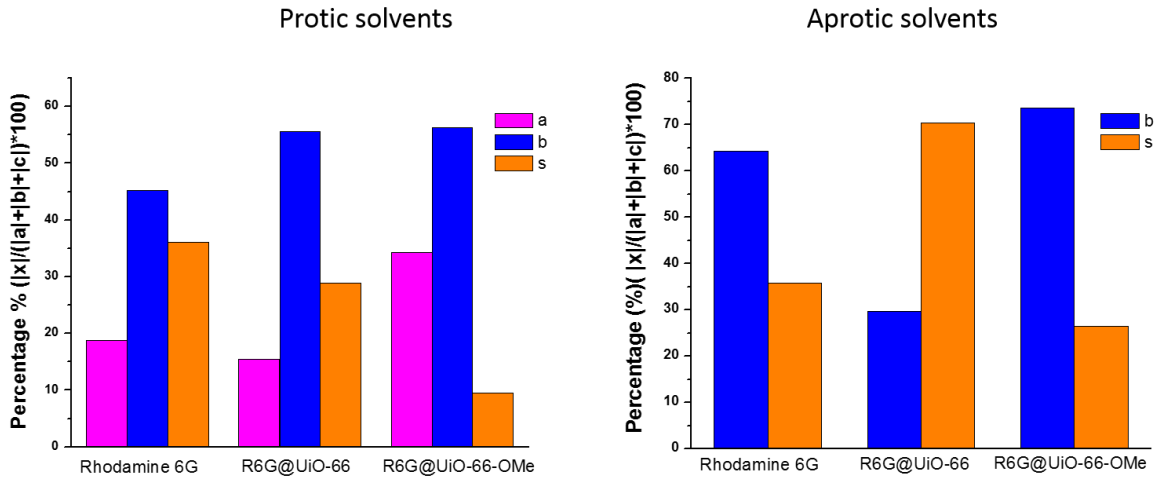

Figure 5-6. Values of Kamlet--Abboud-Taft coefficients a, b, and s, and their weightage fitted from spectra date in protic solvents and aprotic solvents for Rhodamine 6G(R6G), R6G@UiO-66, and R6G@UiO-66-OMe.

All coefficients a, b, and s showed positive values in protic solvents, indicating an increase of Stokes shift with an increase in hydrogen bonding capability (α, β) and solvent polarizability (π*). All a, b, and s values from free Rhodamine 6G to R6G@UiO-66 increased, and increased significantly from R6G@UiO-66 to R6G@UiO-66-OMe indicating the enhancement of chromophore-solvent interaction. These coefficients further signified hydrogen bonding interactions dominating the solvent polarizability based on the observed Stokes shifts in protic solvents. All of those interactions between the host and guest can be altered by simply changing the substituents on the linker.

In contrast, the coefficients a, b and s have either positive or negative values in aprotic solvents. However, the a value is irrelevant to the Stokes shift since α values are negligible in aprotic solvents (Table 5-3). The contributions from hydrogen accepting interactions (β only) decreased and solvent polarizability increased as Rhodamine 6G changed from its solvated state to being encapsulated in UiO-66, which implied the confined cavity played a major role in influencing the solvent polarizability. Interestingly, after the addition of the electron donating –OMe group to UiO-66, the contribution of hydrogen-bond interactions was similar to that of free Rhodamine 6G, which suggested the enhanced solvent polarization capability was balanced by the electronic impact of –OMe.

These results suggested that the factors that influence the change in Rhodamine 6G's solvatochromic behavior are diverse and complex, with influence from the identity of the solvent, the nature of the substituents on the MOF, and the synergistic effect between chromophore-solvent interaction and host-guest interaction.

Generally, solvents that are polar, viscous, or can engage in hydrogen bonding have high chromophore-solvent interaction that stabilize excited states and facilitate relaxation

of excited electrons to the ground state.[11] Solvents with these features – DMF, dioxane, and alcohols – have resulted in the greatest bathochromic shifts. Despite the significant bathochromic shift in fluorescence spectra, there is minimal change in the absorption for encapsulated R6G dye with change in solvent (Table 5-4).

Table 5-4. Absorption λ_{max} of Rhodamine 6G, R6G@UiO-66, and R6G@UiO-66-OMe in protic solvents and aprotic solvents, and the graphical presentation.

Absorption	R6G	R6G@UiO-66	R6G@UiO-66-OMe
Protic solvents			
H_2O	525	532	528
MeOH	527	535	527
nButanol	531	536	533
1-heptanol	533	536	533
1-hexanol	532	538	532
Ethanol	533	537	531
Aprotic solvents			
DMSO	539	541	534
DMF	535	541	536
Dioxane	539	537	537
CH_2Cl_2	521	533	529
Acetone	528	538	529

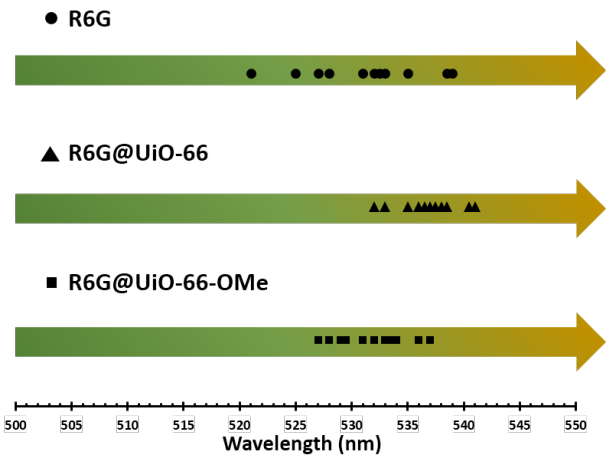

We hypothesize that the observed fluorescence shifts are a product of chromophore-solvent interactions. According to the Franck-Condon principle, a change from one vibrational energy level to another will be more likely to happen if the two vibrational wave functions overlap more significantly. This principle can also be applied to the electronic transitions of a chromophore dissolved in a liquid where the chromophore and solvent molecules have different energies in their ground and excited states. The solvent molecules rearrange themselves to accommodate the change of the electronic configuration of the excited states. Essentially, the change of the dipole moment of a dye

molecule in response to the surrounding solvent molecules leads to the shift in absorption and emission spectra. Since both absorption and emission maxima are similar among solvents for free R6G molecules, we speculate that those solvents employed exhibited similar stabilization of the ground state and excited states of R6G. However, when R6G dye is encapsulated in the solid matrix where functional groups had a substantial electronic and steric influence, the interaction of the electronic states of the dye with the employed solvent in the pore and the surrounding cage environment is significantly perturbed. The amplified solvatochromism observed in R6G@UiO-66-OMe is likely a result of the enhanced solvent-sensitive stabilization of the excited state of Rhodamine 6G by the cage environment. However, the stabilization of the ground state of R6G by solvent is expected to be less pronounced because of its lower charge and weaker dipole moment.

5.6 Linear free energy relationship: Taft equation

After the correlation between substitutes on MOF linker and the solvatochromism of the MOF-encapsulated dye was demonstrated, attempts were made to correlate the solvatochromism to linear free energy relationship (LFER) for electronic and steric factors using Hammet σ or Es. However, no correlation was drawn between these two. It was hypothesized that a correlation was possible by combining both electronic and steric factors using the Taft equation where σ and Es were both involved. Hence, the electronic and steric contributions from the aryl substituents were quantitatively analyzed by applying linear free energy relationships (LFER) in the form of the following Taft equation. (Eq. 2)

$$\log(V_X/V_H)=x*\sigma+y*Es \qquad \text{Eq. 2}$$

Where $\log(V_X/V_H)$ is the logarithmic ratio of the energy (Absorption/Emission/Stokes shift) of the selected functionalized UiO-66-X sample to UiO-66, σ is the polar substituent constant that describes the field and inductive effect of the substituent, and Es is the steric substituent constant (Table 5-5).

Table 5-5. A list of σ and Es values of functional groups (H, NH_2, NO_2, Br, Cl, OMe, Me, I).

Substitutes on Linker	σ (meta)	Es
-H	0	0
$-NH_2$	-0.09	-0.61
$-NO_2$	0.71	-2.52
-Br	0.37	-1.16
-Cl	0.37	-0.97
-OMe	0.1	-0.55
-Me	-0.06	-1.24
-I	0.35	-1.4

The correlation between the absorption spectra and the Taft parameters of functional groups was poor, presumably due to a subtle change in absorption λ_{max} for those samples. For emission and Stokes shift, good correlations could not be observed with linear free energy relationships pertaining to the electronic (σ) or steric (E_s) factors of the

substituents separately but could be obtained if both factors were incorporated in the LFER. For example, a good correlation was found in DMF for R6G@UiO-66-X (R^2=0.94) when both σ and E_s were considered, while no trend was observed if only σ (R^2=0.33) or E_s (R^2=0.03) was included (Figure 5-7).

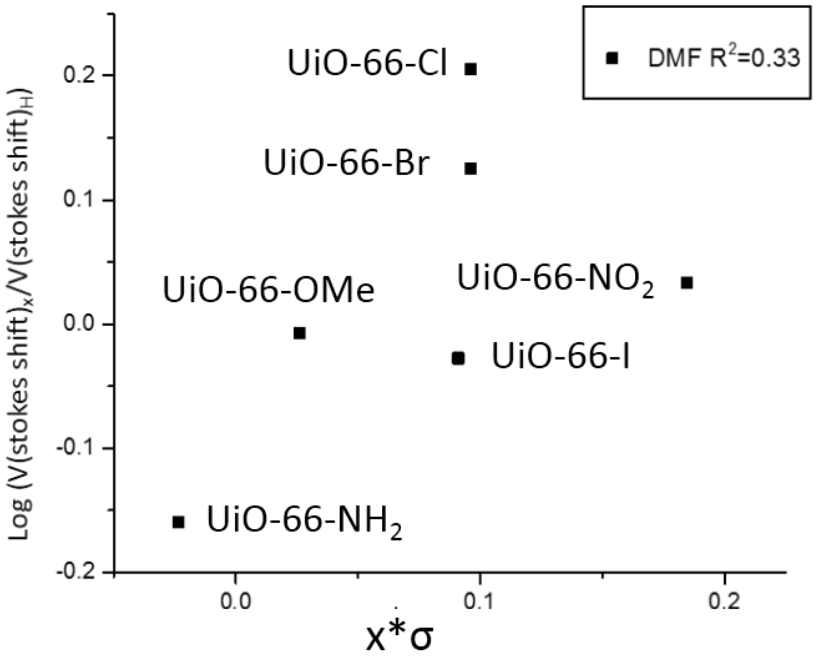

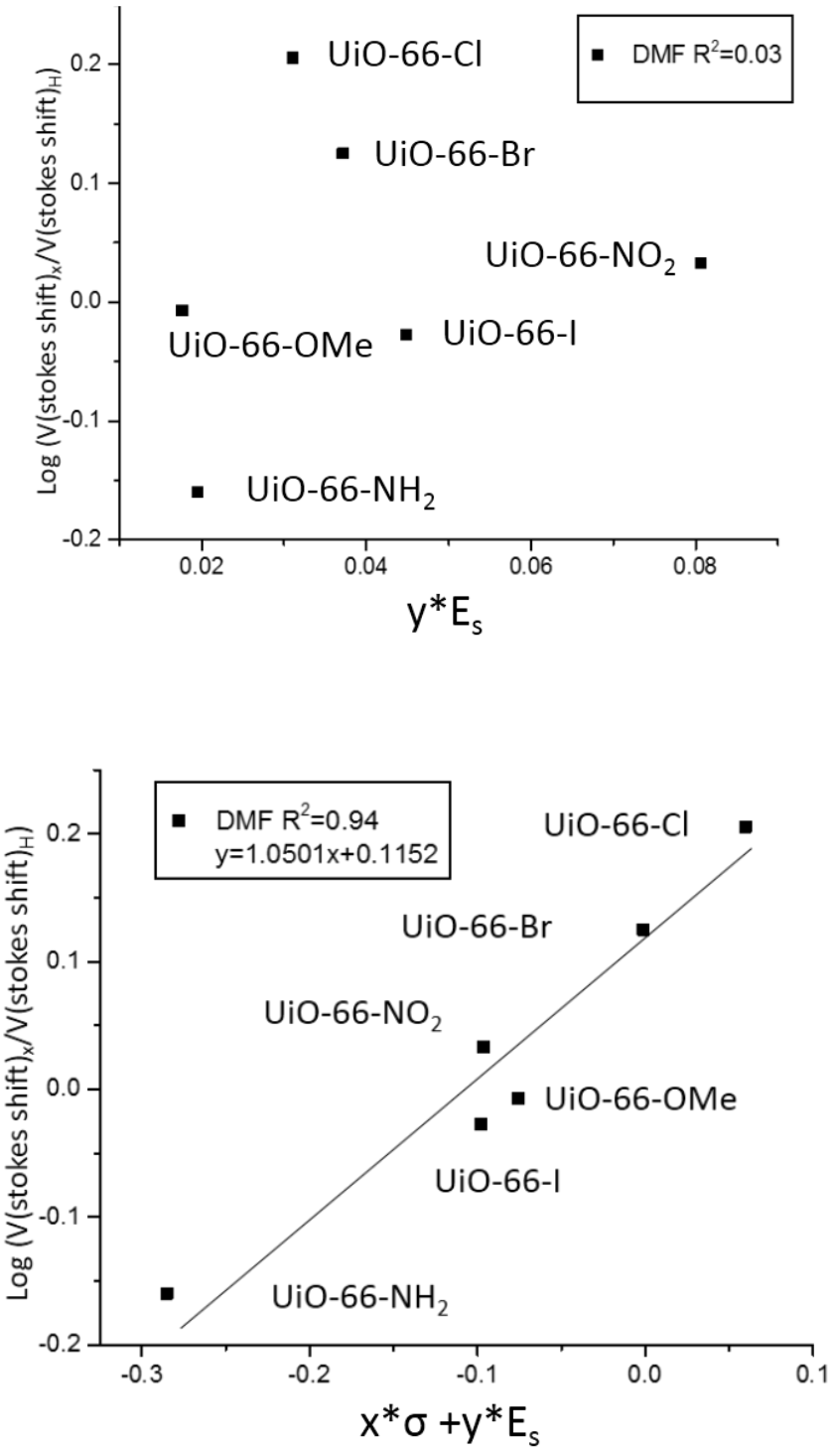

Figure 5-7. Linear free energy relationship between stokes shift and (a) only σ (b) only Es (c) σ and Es in solvent DMF.

The results suggest that a combination of electronic and steric effects are responsible for the bathochromic shift in emission spectra as well as the amplified solvatochromism behavior of the dye. The purpose of acquiring x and y values is to assess how the steric and electronic factors of the substitutes effect the local environment of the MOF cavity rather than predicting Stokes shift. Direct comparison of the relative importance of substituent sterics and electronics is impossible due to the fact that σ and E_s are not normalized to one another. However, evaluating the coefficients (x, y) by comparing one solvent to another can be made to assess how sensitive the relative importance of the substituent sterics and electronics are to the solvent. For small alcohols (MeOH, n-butanol, EtOH) and acetone, which has the same pKa as MeOH, the relative importance of the substituents electronics (x) and sterics (y) on the spectra of encapsulated R6G stay approximately the same. In comparison, large alcohols like 1-heptanol and 1-hexanol alter the relative importance of substituent electronics and sterics: Spectra taken in these solvents are sensitive to both factors more than they would be for more polar alcohols . Nonpolar solvents such as dioxane and CH_2Cl_2 exhibit poor correlation with the emission spectra of the dye molecule (R^2(dioxane): 0.64, $R^2(CH_2Cl_2)$:0.70), second and third worse to water (R^2:0.49). DMSO and DMF are aprotic polar solvents, and they have different x,y values compared to other categories. If there is little change to x and y among solvents, like in 1-hexanol and 1-heptanol, substituent effects dominate the change of photophysical property of the chromophore. If x and y change significantly from solvent to solvent, the nature of the fluorescence is connected to the identity of the solvent as well as the electronic and steric factors of the substituents on the MOF. The outer sphere

interaction in the host-guest system is so complex that any subtle change on solvents and substitutes on MOF linker could lead to a significant change in the photophysical property of the guest molecule.

Table 5-6. Summary of x and y values from linear free energy fitting in all the solvents.

Stokes shift	x	y	R^2	Notes
MeOH	1.22	0.35	0.83	Small alcohol and Acetone (which has same pKa as methanol)
nButanol	1.21	0.44	0.73	
Acetone	1.21	0.33	0.86	
EtOH	1.30	0.35	0.90	
1-Heptanol	1.59	0.59	0.78	Large greasy alcohols
1-Hexanol	1.52	0.51	0.88	
Dioxane	1.92	0.65	0.64	Nonpolar solvents with small β
CH_2Cl_2	1.94	0.58	0.70	
Water	0.65	0.17	0.49	Unique with worst correlation
DMSO	1.02	0.32	0.85	Aprotic polar solvents,large β
DMF	1.05	0.32	0.94	

5.7 Conclusion

Rhodamine 6G was encapsulated into UiO-66, UiO-67, and a series of functionalized UiO-66-X through aperture-opening encapsulation. R6G demonstrated strong solvatochromic behavior only when encapsulated in functionalized UiO-66 derivatives, with emission features tunable through modulation of the functional group on the MOF linker and the identity of the solvent. The comparison between R6G confined in UiO-66 and UiO-67 further demonstrated that spatial confinement was necessary to

maximize host-guest interaction. In addition, the effect of solvent polarity on the absorption and emission features of the free and encapsulated R6G was interpreted by a linear free energy relationship in the form of Kamlet-Abboud-Taft equation. The results revealed that hydrogen bond donating/accepting capability and the polarizability of the solvent influence the photophysical property of the dye significantly. Also, the spectra showed that host-guest interactions respond differently to there factors depending on whether the spectrum was acquired in polar or nonpolar solvent. Moreover, the influence from the electronic and steric features of the linker functional group was investigated using similar linear free energy relationships in the form of the Taft equation. The results from fitting to the Taft equation suggested both electronic and steric properties of the linker substitutes affect the local environment in the MOF cavity. The comparision between UiO-66-encapsualted R6G and UiO-67-encapsualted R6G suggests that distance-dependent non-covalent interactions between the dye and the encapsulated solvent molecules are reinforced by the electronically and sterically altered cage environment. Those interactions are responsible for the changes in the photophysical properties of Rhodamine 6G.

This study has shown that encapsulation of guest molecules into MOFs is an elegant method to create tunable, multifunctional, and moderate solvatochromic materials. The local environment in the cavity of the MOF can be altered by changing the identity of the MOF and solvent that cannot be achieved by changing the solvent alone. We provide an effective exploration of host-guest interactions that otherwise might be less amenable to measurement in other systems. Reminiscent of enzymatic structures, the host-guest system is a simpler, efficient, and economical alternative for investigating outer sphere interactions. The combination of experimental evidence and statistical analysis provides a more diverse

perspective for the subsequent development of host-guest systems to better understand outer sphere interactions in biological analogues, especially catalysis in the future. For instance, catalysis that are highly dependent on solvents can be tuned by encapsulating the active species in a different MOF with functional substitutes. Simply changing the substitutes on MOF linker may have similar effect to the catalytic behavior of the encapsulated catalyst than changing the solvent.

5.8 Experimental section

General considerations Unless otherwise stated, all manipulations were carried out in open air with no precautions taken to protect chemicals/reactions from air or water. $ZrCl_4$ (Sigma Aldrich), terephthalic acid (Sigma Aldrich), [1,1'-biphenyl]-4,4'-dicarboxylic acid (Sigma Aldrich), R6G (Sigma Aldrich) were purchased from the indicated sources and used without further purification. The Powder x-ray diffraction spectra (PXRD) were collected on a Bruker AXS diffractometer with Cu Kα radiation (λ= 1.5418 Å). HPLC graded solvents were used directly without further purification.

Synthesis of UiO-66 The synthesis of UiO-66 is based on a previously published procedure.[6] To a 50 mL pressure vessel reactor, a 80 mM stock solution of $ZrCl_4$ in DMF (1 ml, 0.08 mmol), a 80 mM stock solution of terephthalic acid in DMF (1 ml, 0.08 mmol) were added followed by acetic acid (1.4 ml, 24 mmol). The mixture was then filled up to the total volume of 10 ml. The reaction was carried out at 120 ºC temperature for 24 hours without stirring. The product was collected by centrifugation at 5000 rpm for 10 minutes. The solid precipitate was triturated by decanting the DMF supernatant then re-suspended with fresh DMF (15 mL). The centrifuging and trituration steps were repeated at least 3 times until supernatant was completely transparent. The residual solvent was removed from

the isolated solids in a vacuum oven at 100 °C overnight. The product mass recovery is 16 mg with yield 50%. The material is characterized by PXRD (See below) and the crystalline pattern matches with literature.

Synthesis of functionalized UiO-66-X (X: Cl, Br, NO_2, NH_2, Me)[6] The general synthesis method is the same as the synthesis of UiO-66. Instead of using terephthalic acid (BDC) (0.08 mmol), BDC-Cl (0.08 mmol), BDC-Br (0.08 mmol), BDC-NO_2 (0.08 mmol), BDC-NH_2 (0.08 mmol), BDC-Me (0.08 mmol) was used in the synthesis.

Synthesis of UiO-66-OMe[15] This synthesis was adapted from the literature N,N'-dimethylacetamide (DMA) (9 mL) was added to a 45 mL Teflon-lined steel autoclave. Zirconium oxychloride octahydrate (314 mg, 0.974 mmol) and 2-methoxyl terephthalic acid (191 mg, 0.974 mmol) and concentrated formic acid (3.87 ml, 97.4 mmol) was added to the autoclave, which was then sealed and heated at 150 ºC for 20 hours. The reaction mixture was then allowed to cool to room temperature and agitated to suspend the solid. This solid was isolated by centrifugation, then washed with DMF (15 mL) and left to soak in this solvent overnight. This solid was isolated again by centrifugation and washed twice with methanol (15 mL), then left to soak overnight in methanol. The solid was isolated by centrifugation and dried in a vacuum chamber overnight, then dried overnight in an oven at 70 ºC with a yield of 60 %. The material is characterized by PXRD (Figure 5-6) and the crystalline pattern matches with literature.

Synthesis of UiO-66-I To a 20 ml high-pressure reaction glass vessel was added 100 mg of UiO-66 (BDC: 0.35 mmol), iodine terephthalic acid (200 mg, 0.68 mmol) and 3 mL H_2O. The vessel was then sealed at heated at 80 °C for 8 days using a steady shaker. The solid was isolated by centrifugation and then washed with MeOH until no iodine

terephthalic acid was detected by ^{1}H NMR in the washing solvent. The solid was then collected by centrifugation and dried in heating oven overnight at 70 ºC.

Digestion of UiO-66-I for ^{1}H NMR analysis Solid MOF material UiO-66-I (5.00 mg) was weight out into a 1.5 mL Teflon vial. DMSO-d^{6} (700 µl) and 1 drop of 15 wt.% aqueous hydrofluoric acid solution were added in sequence. The mixture was sonicated for 1 minute and left to digest for 1 hour. An excess of $NaHCO_3$ was then added to the clear solution which effervesced until all of the hydrofluoric acid was neutralized. Neutralized supernatant was loaded into an NMR tube for ^{1}H NMR analysis. Analysis of the NMR spectrum revealed that 92% of original terephthalic acid was exchanged to iodine terephthalic acid.

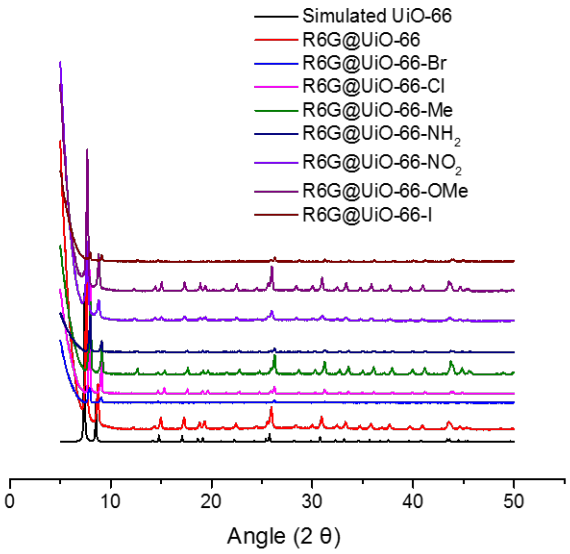

Figure 5-6. PXRD of R6G@UiO-66-X (X=-H, Br, Cl, Me, NH_2, NO_2, OMe, I)

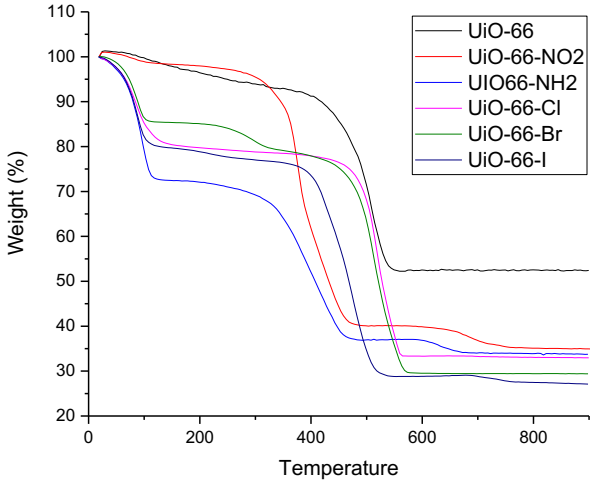

Figure 5-7. TGA of R6G@UiO-66-X (X=-H, Br, Cl, Me, NH_2, NO_2, OMe, I)

Synthesis of UiO-67 The synthesis of UiO-67 is based on a previously published procedure.[6] To a 20 mL vial, a 58 mM solution of $ZrCl_4$ in DMF (5 ml, 0.3 mmol), 0.5 mL con. HCl were added. The mixture was applied with ultrasonication for 20 minutes giving a clear solution. To another 20 ml vial, a 76 mM solution of [1,1'-biphenyl]- 4,4'-dicarboxylic acid (**1**)in DMF (5 ml, 0.38 mmol) was added. The mixture was applied with ultrasonication for 20 minutes giving a translucent suspension. Afterward, the $ZrCl_4$ in DMF solution (5 ml, 0.3 mmol), the **1** in DMF suspension (5 ml, 0.38 mmol), and additional 5 mL DMF were added to a 50 mL pressure vessel reactor in sequence. The mixture was ultrasonicated for additional 5 minutes. The reaction was carried out at 80 °C for 24 hours without stirring. The product was collected by centrifugation at 5000 rpm for 10 minutes. The solid precipitate was triturated by decanting the DMF supernatant then re-suspended with fresh ethanol (15 mL). The centrifuging and trituration steps were repeated at least 3 times and until the supernatant was completely transparent. The residual solvent was

removed from the isolated solids in a vacuum oven at 100 °C overnight. The yield of the reaction is 60%. Product was characterized by PXRD (Figure 5-8), and the crystal structure matches the literature.

Encapsulation of R6G in functionalized UiO-66 through aperture opening encapsulation 10 mL of saturated solution of R6G in H_2O was placed in a 20 mL microwave pressure vessel. To each of the vial, 20 mg of either UiO-66 or functionalized UiO-66 was added. The vial was sealed and the solid was suspended by sonication for 10 minutes. The vial was stirred and heated for three days. The R6G functionalized UiO-66 was collected by centrifugation at 5000 rpm for 10 minutes. The solid precipitate was triturated by decanting the supernatant and dispersed into fresh methanol (10 ml). The centrifugation and trituration steps were repeated at least 5 times until the solvent isolated from the washing solvent was transparent. The residual solvent was removed from the isolated solid in a vacuum overnight and the mass recovery is 90%.

2-Nitrobiphenyl-4, 4'-dicarboxylic acid dimethyl ester [19] To a solution of 2.0 g (7.4 mmol) of biphenyl-4, 4'-dicarboxylic acid dimethyl ester in 20 mL of concentrated sulfuric acid was added 1.2 ml (7.4 mmol) of 56% HNO_3 in 1.5 ml of concentrated H_2SO_4 dropwisely at 15 °C under intense stirring. The reaction mixture was maintained at 15-20 °C for additional 1 h and then was poured on a crushed ice. The precipitated solids were separated by filtration, washed with water, and purified by column chromatography with 20% THF/hexane. Yield 2.0 g (85%) of the colorless crystals. ^{1}H NMR (DMSO-d6), δ: 3.88 (s, 3H, –CH3), 3.93 (s, 3H, –CH3), 7.53 (d, 2H, J^3 ortho = 8.6 Hz, 3',5'/2',6'-Ar), 7.73 (d, 1H, J^3 ortho = 7.9 Hz, 6-Ar(NO 2)), 8.04 (d, 2H, J^3 ortho = 8.6 Hz, 3',5'/2',6'-Ar), 8.28 (dd, 1H, J^3 ortho = 8.0 Hz, J^3 meta = 1.7 Hz, 5-Ar(NO 2)), 8.48 (d, 1H,

J^3 meta = 1.5 Hz, 3-Ar(NO 2)); IR (KBr, ν cm -1): 3107, 3093, 3027, 2980, 2900, 2863, 1733, 1620, 1543, 1443, 1373, 1323, 1293, 1253, 1217, 1200, 1173, 1147, 1133, 1123, 1040, 1023, 993, 980, 973, 940, 907, 890, 873, 837, 793, 787, 770, 720.

Synthesis of 2-Aminobiphenyl-4,4'-dicarboxylic acid dimethyl ester[19] To a solution of 1.46 g (4.6 mmol) of 2-nitrobiphenyl-4,4'-dicarboxylic acid dimethyl ester in 50 ml of dry THF, 1 g of 10% Pd/C was added and the reaction mixture was stirred under hydrogen atmosphere at RT for 1 day. When the consumption of hydrogen ceased, the catalyst was filtered and solvents removed under reduced pressure. The resulting yellow paste was recrystallized from ethanol, and the crude reaction mixture was purified by column chromatography with 20% THF/hexane and dried under reduced pressure. Yield 1.0 g (75%) of light yellow to white solid. ^{1}H NMR (DMSO-d^6 , 500 MHz), δ: 3.84 (s, 3H, $–CH_3$), 3.88 (s, 3H, $–CH_3$), 5.16 (s, 2H, $–NH_2$), 7.16 (s, 1H, 3-Ar(NH_2)), 7.20 (d, 1H, J^3 meta = 1.3 Hz, 6-Ar(NH_2)), 7.45 (d, 1H, J^3 meta = 1.0 Hz, 5-Ar(NH_2)), 7.59 (d, 2H, J^3 ortho = 8.5 Hz, 3',5'/2',6'-Ar), 8.03 (d, 2H, J^3 ortho = 8.5 Hz, 3',5'/2',6'-Ar); IR (KBr, ν cm -1): 3475, 3380, 3225, 3100, 3070, 3047, 3015, 2960, 2900, 2845, 1943, 1913, 1807, 1780, 1720, 1630, 1610, 1570, 1560, 1530, 1490, 1440, 1403, 1367, 1340, 1313, 1303, 1283, 1267, 1250, 1190, 1157, 1123, 1113, 1073, 1020, 1003, 970, 953, 910, 867, 840, 827, 793, 773, 760, 727, 700.

Synthesis of 2-bromobiphenyl-4,4'-dicarboxylic acid dimethyl ester Dimethyl 2-aminobiphenyl-4,4'-dicarboxylate 50 mg (0.175 mmol) was suspended in 5 mL of MeCN, the solution was cooled at 0 °C and a solution of TsOH.H_2O in MeCN (99 mg, 0.53 mmol) was added dropwise. The mixture was stirred at r.t. for 1 hour, then 24 mg (0.35 mmol) CuBr in MeCN was added and the resulting solution was heated and reflux to

60 °C for 2 hrs. The reaction mixture was poured into 50 mL of saturated $Na_2S_2O_3$ aqueous solution and the majority of MeCN was removed under reduced pressure. The residue was extracted with 50 mL ethyl acetate. After the solvent was removed, the crude reaction mixture was purified by column chromatography with 20% THF/hexane on silica gel to give the final product as a pale yellow solid, yield 60%. ^{1}H NMR (400 MHz, $CDCl_3$) δ 8.35 (d, *J* = 1.6 Hz, 1H), 8.11 (d, *J* = 8.3 Hz, 2H), 8.02 (dd, *J* = 8.0, 1.7 Hz, 1H), 7.48 (d, *J* = 8.4 Hz, 1H), 7.39 (d, *J* = 7.9 Hz, 1H), 3.95 (d, *J* = 1.5 Hz, 6H). ^{13}C NMR (400 MHz, Chloroform-*d*) δ 166.81 (s, CO_2-C_6H_3Br), δ 165.60 (s, CO_2-C_6H_4), δ 146.00 (s, C1- C_6H_4), δ 144.69 (s, C1- C_6H_3Br), δ 134.50 (s, C3-C_6H_3Br), δ 131.20 (s, C4-C_6H_3Br), δ 131.09 (s, C5-C_6H_3Br), δ 130.31 (s, C2-C_6H_4), δ 129.95 (s, C6-C_6H_4), δ 129.53 (s, C3-C_6H_4), δ 139.37 (s, C5-C_6H_4), δ 128.61 (s, C4-C_6H_4), δ 127.34 (s, C5-C_6H_3Br), δ 122.37 (s, C2-C_6H_3Br), δ 52.61 (s, CH_3), δ 52.36 (s, CH_3). IR (, ν cm^{-1}): 3073.5, 2962, 2888, 1716, 1600, 1434, 1280, 1235, 1192, 1113, 1062, 963, 845, 826, 754, 697, 549, 490. MS HRMS(DART) calibrated for $C_{16}H_{13}O_4Br$ (M-H)+ 349.00700 found 349.00755.

Synthesis of 2-bromobiphenyl-4,4'-dicarboxylic acid 2-bromobiphenyl-4,4'-dicarboxylic acid dimethyl ester 50 mg (0.14 mmol) was combined with 4 ml THF in a 20 ml vial. An aqueous solution of KOH (48 mg) was added into the vial dropwise at room temperature with steady stirring. The solution was heated to reflux at 60 °C for 20 hours. The reaction was concentrated under reduced pressure and 2 mL of 6M HCl was added dropwise. The final yellow paste was purified by column chromatography with 20% THF/Hexane, resulting in yellow solid, yield: 62%; ^{1}H NMR (DMSO-d^6 , 500 MHz), δ: 7.56 (d, 2H), 7.58 (d, 2H), 7.90 (d, 1H), 8.03 (d, 2H), 8.17 (s, 2H).

Synthesis of UiO-67-Br/UiO-67-NO_2/UiO-67-NH_2 The synthesis protocol of

UiO-67-Br/UiO-67-NO_2/UiO-67-NH_2 is similar to the synthesis of UiO-67.[6] To a 20 mL dram vial, a 58 mM solution of $ZrCl_4$ in DMF (5 ml, 0.3 mmol), 0.5 ml concentrated HCl were added. The mixture was subjected to ultrasonication for 20 minutes giving a clear solution. To another 20 ml dram vial, a 76 mM solution of [1,1'-biphenyl]- 4,4'-dicarboxylic acid variant (BPDC-Br/BPDC-NO_2/BPDC-NH_2) in DMF (5 mL, 0.4 mmol) was added. The mixture was subjected to ultrasonication for 20 minutes giving a translucent suspension. Afterwards, the $ZrCl_4$ in DMF solution (5 ml, 0.29 mmol), the BPDC variant in DMF suspension (5 ml, 0.38 mmol), and additional 5 ml DMF were added to a 50 ml pressure vessel reactor in succession. The mixture was ultrasonicated for additional 5 minutes. The reaction was carried out at 80 °C for 24 hours without stirring. The product was collected by centrifugation at 5000 rpm for 10 minutes. The solid precipitate was triturated by decanting the DMF supernatant then suspended with ethanol (15 ml). The centrifuging and trituration steps were repeated at least 3 times until the supernatant was completely transparent. The residual solvent was removed from the isolated solids in a vacuum oven at 100 °C overnight. The yield for those reactions are about 50%. Products are characterized by PXRD (Figure 5-8) and SEM (Figure 5-9).

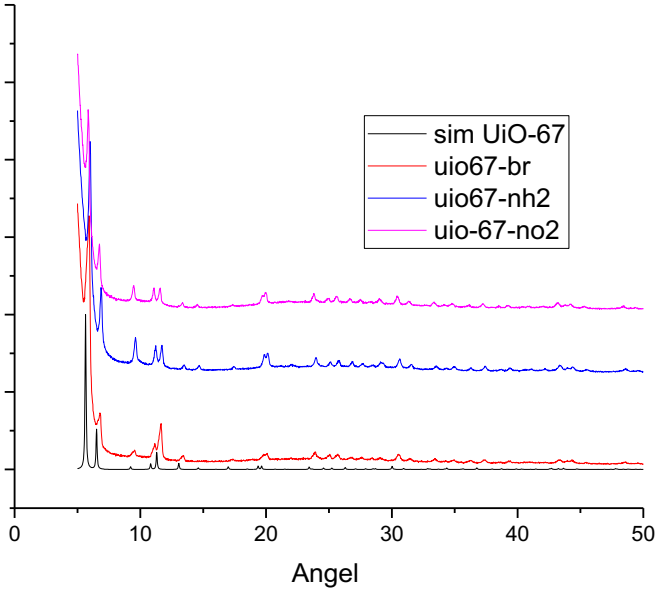

Figure 5-8. PXRD pattern of UiO-67-X (X: Br, NH_2, NO_2)

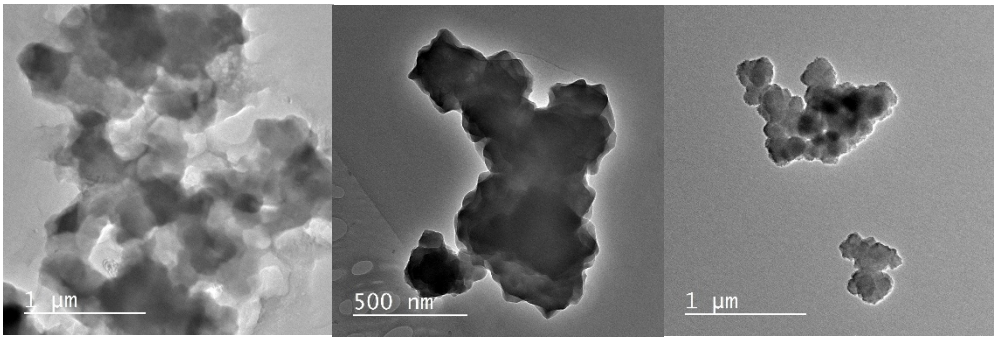

Figure 5-9. TEM images of UiO-67-Br, UiO-67-NO_2, UiO-67-NH_2

Encapsulation of R6G in UiO-67-Br/UiO-67-NO_2/UiO-67-NH_2 through aperture-opening encapsulation 10 mL of saturated solution of R6G in H_20 was placed in a 20 ml microwave pressure vessel. To each of the vial, 20 mg of either UiO-67 or

functionalized UiO-67 was added. The vial was sealed and the solid was suspended by sonication for 10 minutes then heated for three days. The R6G loaded functionalized UiO-67 was collected by centrifugation at 5000 rpm for 10 minutes. The solid precipitate was triturated by decanting the supernatant then re-suspended into methanol (10 mL). The centrifugation and trituration steps were repeated at least 5 times until the last washing solvent was transparent. The residual solvent was removed from the isolated solid in a vacuum overnight with 90% mass recovery.

Reference

(1) Avnir, D.; Levy, D.; Reisfeld, R. *"The nature of the silica cage as reflected by spectral changes and enhanced photostability of trapped Rhodamine 6G"* The Journal of Physical Chemistry **1984**, *88*,5956-5959.

(2) Huang, Y.; Quan, P.; Wang, Y.; Zhang, D.; Zhang, M.; Li, R.; Jiang, N. *"Host-guest interaction of β-cyclodextrin with isomeric ursolic acid and oleanolic acid: physicochemical characterization and molecular modeling study"* Journal of Biomedical Research **2017**, *31*,395-400.

(3) Davis, A. V.; Fiedler, D.; Seeber, G.; Zahl, A.; van Eldik, R.; Raymond, K. N. *"Guest Exchange Dynamics in an M4L6 Tetrahedral Host"* Journal of the American Chemical Society **2006**, *128*,1324-1328.

(4) (a)Yan, D.; Tang, Y.; Lin, H.; Wang, D. *"Tunable Two-color Luminescence and Host–guest Energy Transfer of Fluorescent Chromophores Encapsulated in Metal-Organic Frameworks"* Scientific Reports **2014**, *4*,4337-4340; (b)Ronny, G.; Volodymyr, B.; Andreas, H.; Nicole, K.; Philipp, M.; Ulrich, S.; A., B. I.; Uwe, M.; Irena, S.; Stefan, K. *"Dye Encapsulation Inside a New Mesoporous Metal–Organic Framework for Multifunctional Solvatochromic-Response Function" Chemistry – A European Journal* **2012**, *18*,13299-13304.

(5) (a)Yang, G.-S.; Li, M.-N.; Li, S.-L.; Lan, Y.-Q.; He, W.-W.; Wang, X.-L.; Qin, J.-S.; Su, Z.-M. *"Controllable synthesis of microporous, nanotubular and mesocage-like metal–organic frameworks by adjusting the reactant ratio and modulated luminescence properties of Alq3@MOF composites"* Journal of Materials Chemistry **2012**, *22*,17947-17951; (b)Dolgopolova, E. A.; Moore, T. M.; Ejegbavwo, O. A.; Pellechia, P. J.; Smith, M. D.; Shustova, N. B. *"A metal–organic framework as a flask: photophysics of confined chromophores with a benzylidene imidazolinone core"* Chemical Communications **2017**, *53*,7361-7365.

(6) Katz, M.; Brown, Z. J.; Colon, Y. J.; Siu, P. W.; Scheidt, K. A.; Snurr, R. Q.; Hupp, J. T. *"A facile synthesis of UiO-66, UiO-67 and their derivatives"* Chemical communications **2013**, *49*,9449-9452.

(7) Karagiaridi, O.; Bury, W.; Mondloch, J. E.; Hupp, J. T.; Farha, O. K. *"Solvent-Assisted Linker Exchange: An Alternative to the De Novo Synthesis of Unattainable Metal–Organic Frameworks"* Angewandte Chemie International Edition **2014**, *53*,4530-4535.

(8) (a)Morabito, J. V.; Chou, L.-Y.; Li, Z.; Manna, C. M.; Petroff, C. A.; Kyada, R. J.; Palomba, J. M.; Byers, J. A.; Tsung, C.-K. *"Molecular Encapsulation beyond the Aperture Size Limit through Dissociative Linker Exchange in Metal–Organic Framework Crystals"* J. Am. Chem. Soc. **2014**, *136*,12540-12543; (b)Li, Z.; Rayder, T. M.; Luo, L.; Byers, J. A.; Tsung, C.-K. *"Aperture-Opening Encapsulation of a Transition Metal Catalyst in a Metal–Organic Framework for CO2 Hydrogenation"* Journal of the American Chemical Society **2018**, *140*,8082-8085.

(9) Zehentbauer, F. M.; Moretto, C.; Stephen, R.; Thevar, T.; Gilchrist, J. R.; Pokrajac, D.; Richard, K. L.; Kiefer, J. *"Fluorescence spectroscopy of Rhodamine 6G: Concentration and solvent effects"* Spectrochimica Acta Part A: Molecular and Biomolecular Spectroscopy **2014**, *121*,147-151.

(10) Zakerhamidi, M. S.; Moghadam, M.; Karimi, A. *"Aggregative properties of Rhodamine dyes in polyacrylamide hydrophilic gel media"* Journal of Molecular Structure **2013**, *1033*,289-292.

(11) Penzkofer, A.; Leupacher, W. *"Fluorescence behaviour of highly concentrated rhodamine 6G solutions"* Journal of Luminescence **1987**, *37*,61-65.

(12) Noh, J.; Kim, Y.; Park, H.; Lee, J.; Yoon, M.; Park, M. H.; Kim, Y.; Kim, M. *"Functional group effects on a metal-organic framework catalyst for CO2 cycloaddition"* Journal of Industrial and Engineering Chemistry **2018**, *64*,478-481.

(13) Zakerhamidi, M. S.; Moghadam, M.; Ghanadzadeh, A.; Hosseini, S. *"Anisotropic and isotropic solvent effects on the dipole moment and photophysical properties of rhodamine dyes"* Journal of Luminescence **2012**, *132*,931-935.

(14) Reichardt, C. *"Solvatochromic Dyes as Solvent Polarity Indicators"* Chemical Review **1994**, *94*, 2319-2322.

(15) Shyam, B.; Pascal, V. D. V. *"A General Strategy for the Synthesis of Functionalised UiO-66 Frameworks: Characterisation, Stability and CO2 Adsorption Properties"* European Journal of Inorganic Chemistry **2013**, *2013*,2154-2156.